High-Precision Optical and Microwave Signal Synthesis and Distribution

by

Jungwon Kim

B.S., Electrical Engineering, Seoul National University, 1999
S.M., Electrical Engineering and Computer Science, Massachusetts Institute of Technology, 2004

Submitted to the Department of Electrical Engineering and Computer Science
in partial fulfillment of the requirements for the degree of

Doctor of Philosophy in Electrical Engineering and Computer Science

at the

MASSACHUSETTS INSTITUTE OF TECHNOLOGY

September 2007

Author .....
Department of Electrical Engineering and Computer Science
gust 28, 2007

Certified by.....
.....
Franz X. Kärtner

Accepted by .....
Chairman, Department Committee on Graduate Students

High-Precision Optical and Microwave Signal Synthesis and Distribution

by

Jungwon Kim

Submitted to the Department of Electrical Engineering and Computer Science
on August 28, 2007, in partial fulfillment of the
requirements for the degree of
Doctor of Philosophy in Electrical Engineering and Computer Science

Abstract

In this thesis, techniques for high-precision synthesis of optical and microwave signals and their distribution to remote locations are presented.

The first topic is ultrafast optical pulse synthesis by coherent superposition of mode-locked lasers. Timing and phase synchronization of ultrabroadband Ti:sapphire and Cr:forsterite mode-locked lasers is studied. Subfemtosecond (<0.4 fs) timing synchronization over 12 h is demonstrated. In addition to the timing lock, phase synchronization to a local oscillator with subfemtosecond accuracy (<0.5 fs) over 1000 s is achieved. Drift-free subfemtosecond timing and phase synchronization enables a phase-coherent spectrum over 1.5 octaves that has a potential to generate single-cycle optical pulses at 1 μm.

The second topic is long-term stable microwave signal synthesis from mode-locked lasers. Although mode-locked lasers can produce ultralow-noise microwave signals as a form of optical pulse trains, the transfer of stability from optical to electronic domain is a highly non-trivial task. To overcome the limitations of conventional photodetection, an optoelectronic phase-locked loop based on electro-optic sampling with a differentially-biased Sagnac-loop is proposed. Long-term (>1 h) 3-mrad level phase stability of a 10.225 GHz microwave signal extracted from a mode-locked laser is demonstrated.

The third topic is timing stabilized fiber links for large-scale timing distribution. Precise optical timing distribution to remote locations can result in synchronization over long distances. In doing so, acoustic noise and thermal drifts introduced to the fiber links must be cancelled by a length-correction feedback loop. A single type-II phase-matched PPKTP crystal is used to construct a compact and self-aligned balanced optical cross-correlator for precise timing detection. Using this correlator, a 310 m long fiber link is stabilized with long-term sub-10 fs accuracy.

The final topic is photonic analog-to-digital conversion of high-frequency microwave signals. Sampling of high-frequency (>10 GHz) microwave signals is challenging due to the required aperture jitter below 100 fs. An optical subsampling down-

converter for analog-to-digital conversion of narrowband high-frequency microwave signals is studied. The measured signal to noise-and-distortion ratio of 1-Mbps signals at 9.5 GHz carrier frequency is 22 dB over 2 MHz bandwidth.

By integrating the demonstrated techniques, large-scale femtosecond-precision timing distribution and synchronization systems can be implemented.

Thesis Supervisor: Franz X. Kärtner
Title: Professor of Electrical Engineering

Acknowledgments

First of all, I thank my advisor Prof. Franz Kärtner for his guidance and encouragement. He showed the ideal model of a great mentor – while he gave me the freedom in research, at the same time, he was always happy to share his deep physical insight through numerous discussions. It was pleasure to work with Prof. Mike Perrott on interesting problems at the interface of optics and electronics. Prof. Erich Ippen and Prof. Jeff Shapiro served as the committee members and gave valuable comments.

Working at MIT was simply a great fun. I thank Dr. Thomas Schibli for his advice over years. I enjoyed many scientific and non-scientific discussions with Dr. Oliver Mücke, Dr. Christian Jirauschek and Dr. Lia Matos. Collaboration with Dr. Frank Ludwig and Florian Loehl at DESY was truly fruitful. Jeff Chen's lasers saved many of my projects. Dr. Franco Wong's PPKTP enabled interesting experiments. The ADC project with Matt Park was a fun – well, I admit the by-product (travel to the Switzerland) was the greatest fun. I feel lucky to transfer my projects to the bright new student, Jonathan Cox. All OQE group members were friendly and helpful to each other, and I thank all of them for the comfortable, yet productive, environment.

Research cannot be done without financial support. I thank fellowship from the Samsung Scholarship Foundation. It brought more flexibility in my research topics and scopes. The projects were supported by AFOSR, ONR, DARPA and EuroFEL.

Although I was 6,800 miles away from my hometown, fortunately I didn't have a chance to feel homesick thanks to many good Korean friends in Boston. Some of them are old friends since high school years. I especially thank Korean graduate students in EECS and Korean language class teachers for sharing many joyful moments and valuable experiences. I also wish to express my personal gratitude for the encouragement at the last stage of thesis to Hayun Chung at Harvard University.

Finally, my greatest thanks go to my family – my parents, Kwan and Hyejin, and younger brother Jungho. Without their love and care, I could not finish this thesis. Looking back, my parents have always trusted me and encouraged me to pursue what I like to do – that's why I can stand here now. This thesis is dedicated to them.

Curriculum Vitae

Education

MIT, PhD in Electrical Engineering and Computer Science, September 2007.
MIT, SM in Electrical Engineering and Computer Science, February 2004.
Seoul National University, BS in Electrical Engineering, February 1999.

Research Interest

Ultrafast optics and electronics; instrumentation, measurement and metrology; electronic-photonic integrated circuits; noise in lasers; microwave photonics; fiber optics and optical communications; ultrafast spectroscopy

Employment

MIT, Postdoctoral Associate, Sep 2007–
MIT, Teaching Assistant, Feb 2005 – May 2005
MIT, Graduate Research Assistant, Sep 2002 – Aug 2007
FiberPro, Development Engineer, Mar 1999 – Jul 2002

Awards

IEEE LEOS 2006 Graduate Student Fellowship Award, Oct 2006
Morris Joseph Levin Award from MIT EECS, May 2004
Samsung Scholarship Foundation Graduate Fellowship, Jan 2003 – Jun 2007
Best Paper Award in Photonics Conference 2001, Nov 2001
President's Award from Seoul National University, Feb 1999
Silver medalist in the 26th International Chemistry Olympiad (IChO), Jul 1994

Patents and Patent Applications Pending

1. "Compact background-free balanced cross-correlators" with F. N. C. Wong and F. X. Kärtner, MIT Case No. 12,402 (filed on Oct. 3, 2006)
2. "A balanced optical-radiofrequency phase detector" with F. X. Kärtner, US Provisional Application 60/748,859 (filed on Dec 9, 2005)
3. "Multi-layer thin-film broadband beam splitter with matched group delay dispersion" with F. X. Kärtner, US Patent Application 20050280895 (filed on Dec 22, 2005)
4. "Synchronization of lasers and RF-sources using timing information transfer in the optical domain" with M. H. Perrott and F. X. Kärtner, US Patent Application 20050265406 (filed on Dec 1, 2005)
5. "Apparatus and method for measuring polarization dependent loss using repeated high speed polarization scrambling" with Y. W. Koh and B. W. Lee, US Patent 6,657,709 (issued on Dec 2, 2003)

Publications in Refereed Journals

1. J. Kim, F. Ludwig, M. Felber and F. X. Kärtner, "Long-term stable microwave signal extraction from mode-locked lasers," Opt. Express **15**, 8951 (2007).

2. J. Kim, J. Chen, Z. Zhang, F. N. C. Wong, F. X. Kärtner, F. Loehl, H. Schlarb, "Long-term femtosecond timing link stabilization using a single-crystal balanced cross-correlator," Opt. Lett. **32**, 1044 (2007).
3. J. Kim, F. X. Kärtner, F. Ludwig, "Balanced optical-microwave phase detectors for optoelectronic phase-locked loops," Opt. Lett. **31**, 3659 (2006).
4. O. D. Mücke, R. Ell, A. Winter, J. Kim, J. R. Birge, L. Matos, and F. X. Kärtner, "Self-Referenced 200 MHz Octave-Spanning Ti:Sapphire Laser with 50 Attosecond Carrier-Envelope Phase Jitter," Opt. Express **13**, 5163 (2005).
5. J. Kim, J. R. Birge, V. Sharma, J. G. Fujimoto, F. X. Kärtner, V. Scheuer, G. Angelow, "Ultrabroadband beam splitter with matched group delay dispersion," Opt. Lett. **30**, 1569 (2005).
6. J. Kim, F. X. Kärtner and M. H. Perrott, "Femtosecond synchronization of radio frequency signals with optical pulse trains," Opt. Lett. **29**, 2076 (2004).
7. L. Matos, D. Kleppner, O. Kuzucu, T. R. Schibli, J. Kim, E. P. Ippen, and F. X. Kärtner, "Direct frequency comb generation from an octave-spanning, prismless Ti:sapphire laser," Opt. Lett. **29**, 1683 (2004).
8. T. R. Schibli, O. Kuzucu, J. Kim, E. P. Ippen, J. G. Fujimoto, F. X. Kärtner, V. Scheuer, G. Angelow, "Toward Single-Cycle Laser Systems," (Invited) IEEE J. Sel. Top. Quantum Electron. **9**, 990 (2003).
9. T. R. Schibli, J. Kim, O. Kuzucu, J. Gopinath, S. N. Tandon, G. S. Petrich, L. A. Kolodziejski, J. G. Fujimoto, E. P. Ippen, and F. X. Kärtner, "Attosecond active synchronization of passively mode-locked lasers using balanced cross correlation," Opt. Lett. **28**, 947 (2003).

Proceedings of Refereed Conferences

1. F. X. Kärtner, J. Kim, J. Chen, J. Cox, F. O. Ilday, F. Wong, F. Ludwig, A. Winter, F. Loehl, H. Schlarb, L. Banchi, F. Rossi, M. Ferianis, "Large Scale, Femtosecond Timing Distribution," (Invited) to be presented at *IEEE/LEOS Annual Meeting 2007*, Orlando, FL, Oct 2007.
2. J. Kim, "Large-Scale, Long-Term Stable Femtosecond Timing Distribution and Synchronization," (Invited) Paper FTuL1, to be presented at *OSA Annual Meeting 2007*, San Jose, CA, Sep 2007.
3. F. X. Kärtner, A. Benedick, J. Kim, J. Birge, P. Fendel, M. Sander, "From Octave-Spanning Lasers Toward Single-Cycle Pulse Synthesis," (Invited) to be presented at *Ultrafast Optics (UFO/HFSW) 2007*, Santa Fe, NM, Sep 2007.
4. J. Kim, F. Ludwig, J. Chen, F. Loehl, F. Wong, H. Schlarb, and F. X. Kärtner, "Large-Scale, Long-Term Stable Femtosecond Timing Distribution and Synchronization Systems," Paper TuC3.2, *IEEE/LEOS Summer Topical Meeting on Optical Frequency and Time Measurement and Generation 2007*, Portland, OR, Jul 2007.
5. J. Bisognano, R. A. Bosch, M. Green, H. Hoechst, K. Jacobs, K. J. Kleman, R. Legg, R. Reininger, R. Wehlitz, J. Chen, W. Graves, F. X. Kärtner, J. Kim, D. Moncton, "The Wisconsin VUV/Soft X-ray Free Electron Laser Project," Paper TUPMS041, *Particle Accelerator Conference (PAC) 2007*, Albuquerque, NM, Jun 2007.

6. J. Bisognano, R. A. Bosch, M. Green, K. Jacobs, K. J. Kleman, R. Legg, J. Chen, W. Graves, F. X. Kärtner, J. Kim, "A Superconducting Linac Driver for the Wisconsin Free Electron Laser," Paper TUPMS042, *Particle Accelerator Conference (PAC) 2007*, Albuquerque, NM, Jun 2007.
7. F. Loehl, H. Schlarb, J. Chen, F. X. Kärtner, J. Kim, "First Prototype of a Fiber Link Stabilization for the FLASH Synchronization System Based on Optical Cross-Correlation," Paper WEPB16, *Beam Diagnostics and Instrumentation for Particle Accelerators (DIPAC) 2007*, Venice, Italy, May 2007.
8. J. Kim, F. Ludwig, M. Felber, H. Schlarb, and F. X. Kärtner, "Long-Term Stable Microwave Signal Extraction from Mode-Locked Lasers," Paper CMKK5, *Conference on Lasers and Electro Optics (CLEO) 2007*, Baltimore, MD, May 2007.
9. J. Kim, F. Loehl, J. Chen, Z. Zhang, H. Schlarb, F. N. C. Wong, and F. X. Kärtner, "Long-Term Femtosecond Timing Link Stabilization Using a Single-Crystal Balanced Cross-Correlator," Paper CMKK2, *Conference on Lasers and Electro Optics (CLEO) 2007*, Baltimore, MD, May 2007.
10. M. Park, J. Kim, F. X. Kärtner, and M. H. Perrott, "An Optical-Electrical Sub-Sampling Receiver Employing Continuous-Time Delta-Sigma Modulation," Paper A6L-E4, *European Solid-State Circuits Conference (ESSCIRC) 2006*, Montreux, Switzerland, Sep 2006.
11. J. Kim, J. Chen, Z. Zhang, F. Ludwig, and F. X. Kärtner, "Femtosecond Synchronization and Stabilization Techniques," (Invited) Paper TUBAU02, *Free Electron Laser (FEL) 2006*, Berlin, Germany, Aug 2006.
12. J. Kim, J. Burnham, J. Chen, F. X. Kärtner, F. Ö. Ilday, F. Ludwig, H. Schlarb, A. Winter, M. Ferianis, D. Cheever, "An Integrated Femtosecond Timing Distribution System for XFELs," Paper THOPA03, *European Particle Accelerator Conference (EPAC) 2006*, Edinburgh, UK, Jun 2006.
13. J. Kim, F. Ludwig, D. Cheever, F. Ö. Ilday, J. Burnham, and F. X. Kärtner, "A Balanced Optical-RF Phase Detector," Paper CTuP5, *Conference on Lasers and Electro Optics (CLEO) 2006*, Long Beach, CA, May 2006.
14. F. Ö. Ilday, A. Winter, J. Chen, J. Kim, and F.X. Kärtner, "Long-Distance Optical Synchronization for X-Ray Free Electron Lasers," Paper CTuP4, *Conference on Lasers and Electro Optics (CLEO) 2006*, Long Beach, CA, May 2006.
15. J. Kim, T. R. Schibli, L. Matos, H. Byun, and F. X. Kärtner, "Phase-coherent spectrum from ultrabroadband Ti:sapphire and Cr:forsterite lasers covering the visible to the infrared," (Invited) Paper M3-5, *Ultrafast Optics (UFO/HFSW) 2005*, Nara, Japan, Sep 2005.
16. M. Ferianis, J. M. Byrd, J. Staples, R. Wilcox, J. Chen, F. O. Ilday, F. X. Kärtner, J. Kim, A. Winter, "Generation and Distribution of Stable Timing Signals to Synchronize RF and Lasers at the FERMI FEL Facility," Paper MOPP041, *Free Electron Laser (FEL) 2005*, Stanford, CA, Aug 2005.
17. A. Winter, H. Schlarb, J. Chen, F. Ö. Ilday, F. X. Kärtner, J. Kim, P. Schmüsser, "Synchronization of Femtosecond Pulses," (Invited) Paper FROA002, *Free Electron Laser (FEL) 2005*, Stanford, CA, Aug 2005.

18. J. Kim, F. Ö. Ilday, A. Winter, and F. X. Kärtner, "Timing Distribution and RF-Synchronization with Mode-Locked Lasers," Paper WB3.4, *IEEE/LEOS Summer Topical Meeting on Optical Frequency and Time Measurement and Generation 2005*, San Diego, CA, Jul 2005.
19. F. X. Kärtner, O. D. Mücke, P. Wagenblast, R. Ell, A. Winter, J. Kim, A. Siddiqui, L. Matos, "Solid-State Lasers for Frequency Metrology," (Invited) Paper TuB1.1, *IEEE/LEOS Summer Topical Meeting on Optical Frequency and Time Measurement and Generation 2005*, San Diego, CA, Jul 2005.
20. O. D. Mücke, R. Ell, A. Winter, J. Kim, L. Matos, and F. X. Kärtner, "Self-Referenced 200 MHz Octave-Spanning Ti:Sapphire Laser with 0.10 Radian Carrier-Envelope Phase Error," *ESA International Workshop on Optical Clocks*, Noordwijk, the Netherlands, Jun 2005.
21. F. X. Kärtner, F. Ö. Ilday, J. Kim, A. Winter, "Progress in large scale femtosecond timing distribution and rf-synchronization," (Invited) Paper TOPB003, *Particle Accelerator Conference (PAC) 2005*, Knoxville, TN, May 2005.
22. A. Winter, P. Schmüsser, H. Schlarb, F. Ö. Ilday, J. Kim, J. Chen, and F. X. Kärtner, "Phase Noise Characteristics of Fiber Lasers as Potential Ultra-Stable Master Oscillators," Paper RTTP038, *Particle Accelerator Conference (PAC) 2005*, Knoxville, TN, May 2005.
23. A. Winter, H. Schlarb, B. Schmidt, F. Ö. Ilday, J. Kim, J. Chen, F. J. Grawert, and F. X. Kärtner, "Stabilized Optical Fiber Links for the XFEL," Paper RTTP039, *Particle Accelerator Conference (PAC) 2005*, Knoxville, TN, May 2005.
24. O. D. Mücke, R. Ell, A. Winter, J. Kim, L. Matos, and F. X. Kärtner, "Carrier-envelope phase stabilized 200 MHz octave-spanning Ti:sapphire laser," (Post-deadline paper) Paper PD3, *Advanced Solid State Photonics (ASSP) 2005*, Vienna, Austria, Feb 2005.
25. J. Kim, F. Ö. Ilday, F. X. Kärtner, O. D. Mücke, M. H. Perrott, W. S. Graves, D. E. Moncton, T. Zwart, "Large-Scale Timing Distribution and RF-Synchronization for FEL Facilities," Paper TUAOS3, *Free Electron Laser (FEL) 2004*, Trieste, Italy, Aug 2004.
26. J. Kim, M. H. Perrott, and F. X. Kärtner, "Femtosecond synchronization of RF-signals with optical pulse trains," Paper ThD2, *Ultrafast Phenomena (UP) 2004*, Niigata, Japan, Jul 2004.
27. J. Kim, F. X. Kärtner, V. Scheuer, G. Angleow, "Ultrabroadband beam splitter with matched group delay dispersion," Paper ThA5, *Optical Interference Coating (OIC) 2004*, Tucson, AZ, Jun 2004.
28. L. Matos, O. Kuzucu, T. R. Schibli, J. Kim, E. P. Ippen, D. Kleppner, and F. X. Kärtner, "Direct frequency comb generation from an octave spanning, prism-less Ti:sapphire laser," Paper CMO1, *Conference on Lasers and Electro Optics (CLEO) 2004*, San Francisco, CA, May 2004.
29. F. X. Kärtner, T. R. Schibli, J. Kim, O. Kuzucu, L. Matos, J. G. Fujimoto, and E. P. Ippen, "Towards single-cycle optical pulses," (Invited) Paper MJ2, *OSA Annual Meeting 2003*, Tuscon, AZ, Oct 2003.

30. F. X. Kärtner, L. Matos, J. Kim, O. Kuzucu, T. R. Schibli, J. G. Fujimoto and E. P. Ippen, "An Octave Spanning Prismless Ti:sapphire Laser as Direct Frequency Comb Generator," Paper TuZ3, *IEEE/LEOS Annual Meeting 2003*, Tucson, AZ, Oct 2003.
31. T. R. Schibli, J. Kim, L. Matos, A. W. Killi, J. Gopinath, S. Tandon, G. Petrich, J. G. Fujimoto, E. P. Ippen, F. X. Kärtner, L. A. Kolodziejski, "300 attosecond active synchronization of passively mode-locked lasers using balanced cross-correlator," Paper JTuC4, *Conference on Lasers and Electro Optics (CLEO) 2003*, Baltimore, MD, Jun 2003.
32. T. R. Schibli, J. Kim, O. Kuzucu, J. T. Gopinath, S. N. Tandon, G. S. Petrich, L. A. Kolodziejski, J. G. Fujimoto, E. P. Ippen, and F. X. Kärtner, "Attosecond active synchronization of passively mode-locked lasers using balanced cross-correlation," (Post-deadline paper) *Advanced Solid State Photonics (ASSP) 2003*, San Antonio, TX, Feb 2003.
33. J. Kim, T. H. Kim, and B. W. Lee, "Measurement of Polarization Dependent Loss of Fiber Optic Components Using a Polarization Scrambler," Paper F4C3, *Photonics Conference 2001*, Mt. Seorak, Korea, Nov 2001.
34. J. Kim and B. W. Lee, "A New High Speed Measurement Method of Polarization Dependent Loss," *National Fiber Optic Engineers Conference (NFOEC) 2001*, Baltimore, MD, Jul 2001.

Other Major Publications

1. J. Kim, T. R. Schibli, L. Matos, H. Byun, and F. X. Kärtner, "Phase-Coherent Spectrum from Ultrabroadband Ti:sapphire and Cr:forsterite Lasers Covering the Visible to the Infrared," in *Ultrafast Optics V*, S. Watanabe and K. Midorikawa, eds. (Springer, 2007), pp. 87-94.

Invited Talks

1. "Large-Scale, Long-Term Stable Femtosecond Timing Distribution and Synchronization," to be presented at *OSA Annual Meeting 2007*, San Jose, CA, Sep 2007.
2. "Femtosecond Synchronization and Stabilization Techniques," at *Free Electron Laser 2006*, Berlin, Germany, Aug 2006.
3. "Sub-fs laser-laser and laser-RF synchronization," Optical Metrology Division, Korea Research Institute of Standards and Science (KRISS), Daejeon, Korea, Feb 2006.
4. "Progress Toward Single-Cycle Optical Pulse Synthesis," Coherent X-Ray Research Center and Department of Physics, Korea Advanced Institute of Science and Technology (KAIST), Daejeon, Korea, Jan 2006.
5. "Optical-Electrical Hybrid Phase-Locked Loops," Department of Electrical Engineering, Korea Advanced Institute of Science and Technology (KAIST), Daejeon, Korea, Jan 2006.
6. "Phase-coherent spectrum from ultrabroadband Ti:sapphire and Cr:forsterite lasers covering the visible to the infrared," at *Ultrafast Optics 2005*, Nara, Japan, Sep 2005.

7. "Laser-RF Synchronization," Applied Photonic Systems Laboratory and School of Electrical Engineering, Seoul National University, Seoul, Korea, Dec 2004.
8. "Progress in Large-Scale Timing Distribution and RF-Synchronization for FEL Facilities," Pohang Accelerator Laboratory (PAL), Pohang, Korea, Dec 2004.
9. "Laser and RF Synchronization," at *ICFA Workshop on the Physics of Seeded Free Electron Lasers*, Cambridge, MA, Jun 2004.

Contents

List of Figures

Chapter 1

Introduction

Ultrashort optical pulse generation has a rich history of more than 40 years. Recent progress in ultrashort optical pulse technology has enabled the generation of sub-two-cycle optical pulses with 5 femtoseconds (fs, 10^{-15} s) duration and octave-spanning spectra directly from a mode-locked laser [1]. Traditionally, ultrashort optical pulses from mode-locked lasers have mostly been used for time-resolved studies of ultrafast phenomena on picosecond (ps, 10^{-12} s) and femtosecond time scales [2].

Recently, new insight into the frequency and noise characteristics of mode-locked lasers has initiated intense research activities in new directions. In the frequency domain, the pulse train from the mode-locked laser corresponds to millions of regularly spaced frequency lines, which is called an optical frequency "comb." Figure 1-1 shows the time-frequency correspondence between the pulse train and the frequency comb.

By stabilizing the spacing (repetition rate, f_{rep}) and the offset (carrier-envelope offset frequency, f_{ceo}) of the frequency comb, one can measure an arbitrary optical frequency with unprecedented accuracy [3, 4]. This frequency property of mode-locked lasers has enabled precision frequency spectroscopy and provided a platform for an optical atomic clock [5]. The importance of this technique was also recognized by the 2005 Nobel Prize in Physics shared by John Hall and Theodor Hänsch for their contribution to the frequency comb technology [6].

As these frequency-domain techniques were developed and improved, they also had an impact on the time-domain control of ultrashort pulses. In particular, the coupling

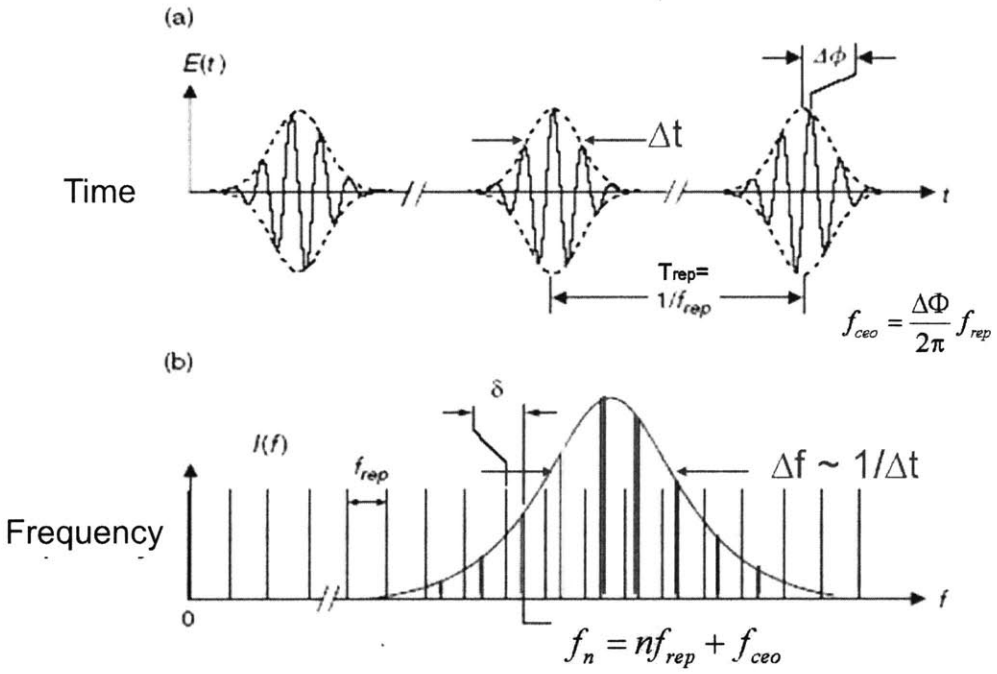

Figure 1-1: Time-frequency correspondence between the optical pulse train in the time domain and the frequency domain. The pulse train has a period of T_{rep}, same as the round-trip time ($2L/c$ where L is the laser cavity length and c is the velocity of light) in the laser cavity. In the frequency domain, this pulse train corresponds to regularly spaced frequency lines whose bandwidth is inversely proportional to the pulse width ($\Delta f \sim 1/\Delta t$). The spacing corresponds to the repetition rate $f_{rep} = 1/T_{rep}$, and the entire frequency comb lines are shifted by an offset frequency named carrier-envelope offset frequency, f_{ceo}. Each comb line can be expressed as $f_m = mf_{rep} + f_{ceo}$ (m=integer). Figure is modified from Ref. [7].

of time-domain and frequency-domain techniques became important for few-cycle optical pulses. For few-cycle optical pulses, the pulse shape in the time domain critically depends on the carrier-envelope phase stabilization, a concept mainly developed in the frequency domain. In the last few years, phase-stabilized few-cycle optical pulses have opened up new possibilities for various extreme light-matter interactions that directly depend on the light electric-field oscillations, for example, high-harmonic generation (HHG) for extreme ultraviolet (EUV) and soft x-ray pulse generation [8, 9].

Another interesting and important aspect of pulse trains from mode-locked lasers is their excellent noise performance. The repetition rate of the pulse train shows very low phase noise and timing jitter [10]. Due to its excellent noise performance, a mode-locked laser has the potential to serve as a master clock for systems that require stringent timing accuracy, such as (i) high-precision microwave signal synthesizer, (ii) high speed (>GHz), high resolution optical sampling and analog-to-digital converters (ADCs), (iii) phased array antenna systems, and (iv) large-scale optical clock signal distribution and synchronization systems.

1.1 Today's Ultrashort Pulse Mode-Locked Lasers

Today state-of-the-art ultrashort pulse mode-locked lasers are developed with dramatic improvements pushing their limits in achieving shorter pulses, broader spectra, higher pulse energy and peak power, higher repetition rate, and lower timing and phase jitters: for example, shorter than 5 fs pulse duration [1], broader than octave (600 nm to 1200 nm) optical spectrum [1, 11, 12], higher than 70 GHz repetition rate [13], lower than 10 fs timing jitter [10 kHz, 10 MHz] in the free-running repetition rate [14], and lower than 50 attoseconds (as, 10^{-18} s) residual carrier-envelope offset phase jitter [15] have been recently demonstrated. In conjunction with the advance in optical amplifiers, mJ-level pulses with less than 10 fs pulse duration, reaching TW-level peak power, can be generated [16].

Among numerous types of mode-locked lasers, the Kerr-lens mode-locked Ti:sappphire laser is arguably the most important laser source in today's ultrafast science and

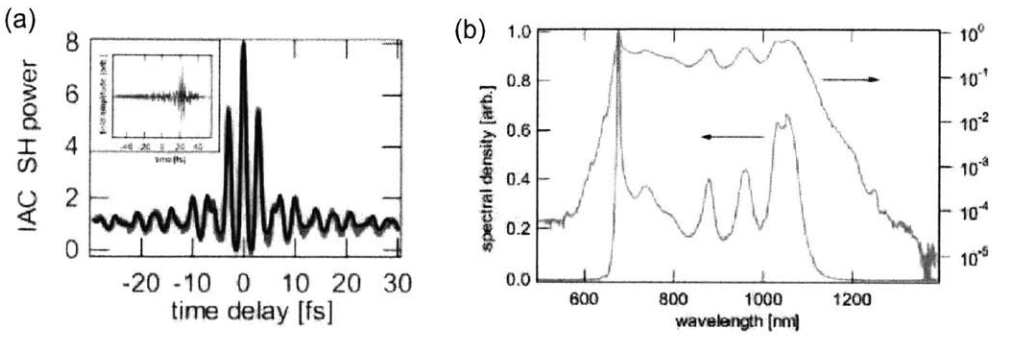

Figure 1-2: Pulse characterization and optical spectrum of the Ti:sapphire laser. (a) Interferometric autocorrelation trace of 5-fs pulses. (b) Optical spectrum spans from 550 nm to over 1400 nm range. Figure reproduced from Ref. [1].

technology. Its broad gain spectrum and excellent mechanical and optical stability enabled generation of less than 10 fs pulses in a 'routine' way from almost every laboratory studying ultrafast phoenomena around the world. As shown in Fig. 1-2, optical pulses with less than two cycles of oscillation with octave spanning optical spectrum can be generated directly from the Ti:sapphire mode-locked lasers with careful dispersion-control engineering by double-chirped mirror pairs [17]. Although the 5 fs pulse is extremely short on its own, it further enables generation of even shorter pulses by the HHG processes - most recently, an isolated 130 as EUV pulse was generated from Argon gas driven by the electric field of 5 fs pulses at 800 nm originated from a Ti:sapphire laser system [18].

A mode-locked laser is useful not only for producing extremely short optical pulses but also for producing extremely low-noise pulses. Gain media such as Erbium (Er)- and Erbium/Ytterbium (Er/Yb)-doped glasses and fibers are advantageous in achieving low-noise pulses owing to their long upper-state lifetime. In addition, at their operating wavelength centered at 1550 nm, various telecommunication-grade components are commercially available. Recent efforts toward using mode-locked lasers as master oscillators for high-precision timing systems push toward building higher repetition rate and lower noise Er- or Er/Yb-mode-locked lasers. Previously, a 750 MHz repetition rate Er/Yb-glass mode-locked laser locked to an external clock signal resulted in 14 fs timing jitter integrated from 10 Hz to 375 MHz [19]. More recently, a

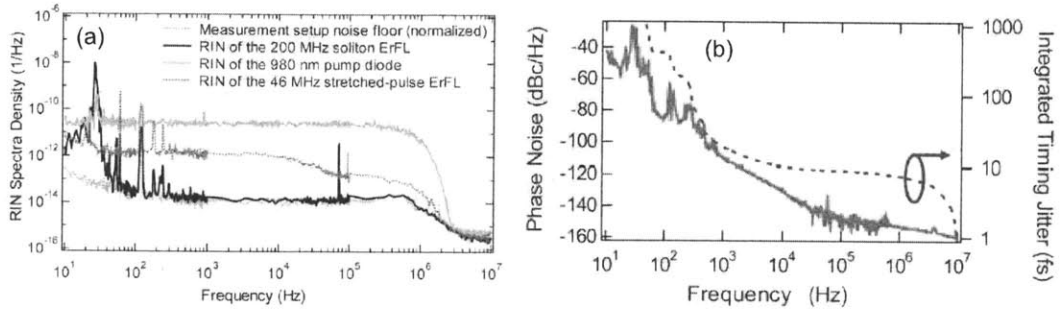

Figure 1-3: (a) Relative intensity noise and (b) phase noise density (at 1 GHz) and integrated timing jitter for 200-MHz soliton mode-locked Er-fiber laser. Figure reproduced from Ref. [14].

200 MHz repetition rate soliton mode-locked Er-fiber laser is demonstrated with 0.003 % integrated intensity noise and less than 10 fs timing jitter integrated from 10 kHz to 10 MHz [14] as shown in Fig. 1-3. These high repetition rate and low noise sources have a promise for master oscillators in timing systems, photonic analog-to-digital converters, and arbitrary optical waveform generators.

1.2 High-Precision Optical and Microwave Signal Synthesis and Distribution

Although there has been remarkable progress in ultrafast laser technology, as overviewed in Section 1.1, the real potential of this technology is not yet fully exploited. In particular, precise synchronization between multiple mode-locked lasers and/or microwave sources with femtosecond and subfemtosecond accuracy may open up a new regime of high-precision control and synthesis of optical and microwave signals. This thesis work is directed toward answering important questions regarding high-precision control, distribution, and measurement of ultrashort optical pulses and microwave signals, such as:

- Can we synthesize optical pulses that a single mode-locked laser cannot generate, such as optical pulses with a duration of single optical cycle?
- Can we synthesize microwave signals with ultralow timing jitter and excellent

phase stability over extended periods of time (e.g., days) from mode-locked lasers?

- Can we distribute high-precision optical and microwave signals to remote locations without excess noise over long distances?
- Can we use optical pulse trains for sampling microwave signals to overcome the bottleneck set by electronic jitters?

The next section shows a representative example how high-precision optical and microwave signal synthesis and distribution can be applied in an integrated way in *real* large-scale facilities requiring femtosecond precision.

1.2.1 Example: Large-Scale Timing Distribution and Synchronization for Next Generation Light Sources

Seeding of free electron lasers operating in the EUV and soft/hard x-ray regime with radiation generated from ultrafast laser sources, either directly, via nonlinear crystals, or via high harmonics from noble gases, may result in a fully coherent x-ray laser. For seeding of such large-scale facilities spanning over several hundreds meters to a few kilometers, it is critical to synchronize low-level RF-systems, photo-injector lasers, seed radiation and potential probe lasers with low timing jitter, preferably in sub-10 fs range, in a long-term stable arrangement [20].

For such large-scale timing distribution and synchronization systems, it is essential to have (i) an ultra-low noise master oscillator, (ii) a means for dissemination of timing signals to remote locations with minimal excess noise and drift, and (iii) tight and drift-free synchronization of RF- or optical subsystems to the delivered timing signal at each remote location. Conventional timing distribution based on coaxial RF-cables can never achieve sub-10 fs accuracy, and a completely different approach is required. As presented in Section 1.1, mode-locked lasers have the potential for generating ultra low-jitter optical pulse trains [10, 21, 22], and serving as an optical master oscillator for this application. The microwave signal is encoded in the pulse repetition rate and its harmonics, and any harmonic component up to the detector bandwidth can be recovered from the optical pulse train upon photodetection. The

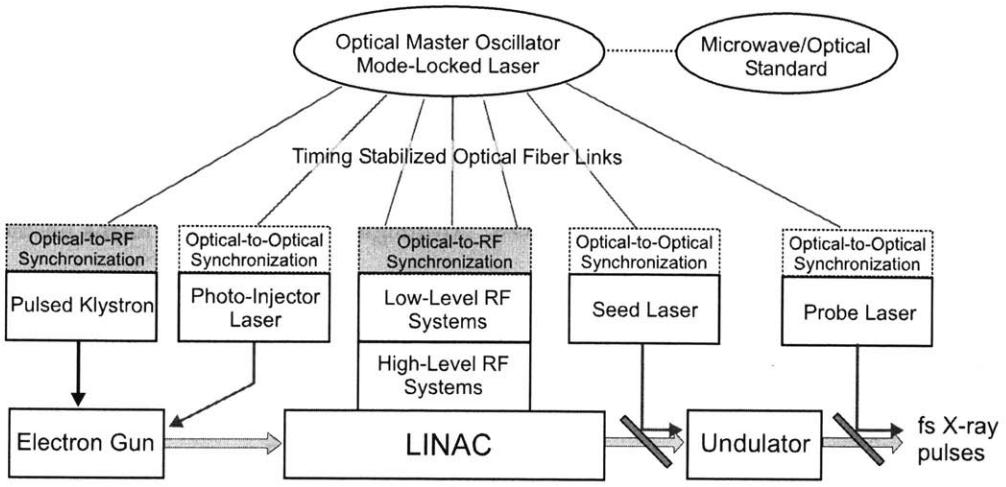

Figure 1-4: Schematic outline of a seeded X-ray free electron laser (XFEL). Tight remote synchronization between various lasers and RF-systems inside the linear accelerator is necessary for operating this facility.

use of optical signals as a means for timing delivery has an additional advantage that it is more robust against electromagnetic interference (EMI) and temperature drift in the accelerator facilities in comparison with RF-coaxial cables. Together with timing-stabilized fiber links and multiple optoelectronic conversion units at remote locations, a flexible timing distribution and synchronization system can be built with a mode-locked laser as an optical master oscillator.

Figure 1-4 shows the schematic of the envisioned timing distribution and synchronization system for the future next generation light sources, seeded x-ray free electron lasers (XFELs). The pulse repetition rate of an optical master oscillator implemented as a mode-locked laser is stabilized to an optical and/or microwave frequency standard. The pulse train is distributed to all critical sub-systems, i.e., the pulsed klystron, the photo-injector laser, the low-level RF systems for the linear accelerator, the seed laser as well as probe lasers, by use of timing stabilized fiber links. Finally, low-jitter, drift-free optical-to-RF and optical-to-optical synchronization between the distributed pulse trains and the remote RF- or optical subsystems will result in a tightly synchronized timing system over the full scale of the accelerator facility.

1.2.2 Scope of the Thesis

The focus of this thesis is how to synthesize ultrafast optical signals and low-noise microwave signals by high-precision optoelectronic synchronization and distribute this timing information over long distances. Although each technique forms an independent topic and has different motivations and applications, by integrating all these techniques, one can build a flexible and modular timing distribution and synchronization system visualized in Fig. 1-5.

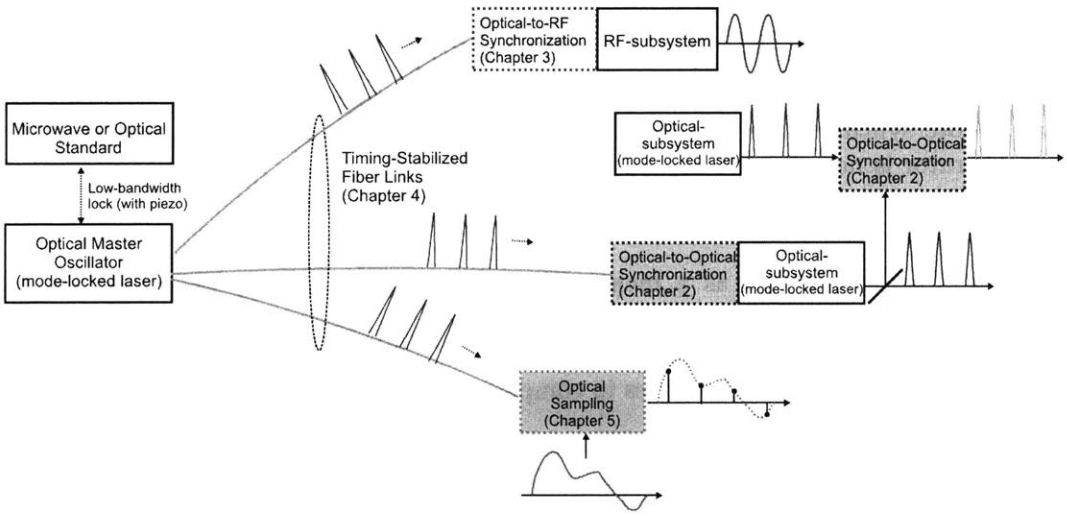

Figure 1-5: Schematic outline of timing distribution and synchronization system. Optical-to-optical synchronization for timing lock and pulse synthesis is presented in Chapter 2. Optical-to-RF synchronization for low-jitter microwave signal synthesis is presented in Chapter 3. Timing stabilized fiber links for timing distribution is presented in Chapter 4. Optical sampling of narrowband high-frequency microwave signals is presented in Chapter 5.

Ultrafast optical signal synthesis by coherent superposition of mode-locked lasers

It has long been recognized that timing and phase synchronization of multiple mode-locked lasers with overlapping spectra may synthesize shorter pulses by extended effective spectra [23]. In particular, this technique has been expected as a promising way to generate a single-cycle optical pulse, comprised of only one cycle of light

oscillation, beyond the bandwidth limitations of a single mode-locked laser.

In this thesis research, timing and phase synchronization of ultrabroadband Ti:sapphire and Cr:forsterite mode-locked lasers covering 1.5 octaves (600-1500 nm) is studied. Subfemtosecond (<0.4 fs) timing (repetition rate) synchronization over 12 hours is demonstrated. In addition to the timing synchronization, phase (carrier-envelope offset frequency) synchronization to a local oscillator with subfemtosecond accuracy (<0.5 fs) over 1000 seconds is demonstrated. Drift-free subfemtosecond timing and phase synchronization enables a phase-coherent spectrum over 1.5 octaves that has a potential to generate single-cycle optical pulses at 1 μm.

Long-term stable microwave signal synthesis from mode-locked lasers

Mode-locked lasers can produce very low jitter microwave signals in the form of optical pulse trains [10, 21, 22]. However, the extraction of a clean micrwoave signal from the pulse train is a highly non-trivial task. Recently, it was shown that the extraction of a microwave signal from an optical pulse train using direct photodetection, the most commonly used technique for microwave signal regeneration from optical pulses, is limited in precision by excess phase noise [24]. In addition, a high temperature sensitivity of the semiconductor photodetector (>300 fs/K is measured in Ref. [25]) limits the long-term stable operation.

In this thesis research, to circumvent the excess noise and to ensure long-term stable operation, new techniques for microwave signal synthesis are demonstrated using optoelectronic phase-locked loops. The phase error between the pulse train and microwave signal is detected by electro-optic sampling and corrected in the optical domain before photodetection is involved. A long-term (>1 hour) 3-mrad level phase stability of a 10.225 GHz microwave signal extracted from a mode-locked laser is demonstrated.

Timing stabilized fiber link for timing distribution

Precise optical timing distribution to remote locations is important for large-scale facilities requiring high-precision synchronization. Acoustic noise and thermal drifts

introduced to the distribution fiber must be canceled by a proper feedback loop. So far, electronic techniques based on high-speed photodetectors and microwave mixers are used to stabilize fiber links on a rather short-term time scale [26, 27]. The limited resolution as well as thermal drifts of microwave components make it difficult to stabilize links better than 100 fs in a long-term stable way.

In this thesis research, to overcome these limitations set by the performance of microwave components and techniques, optical cross-correlation is used for high-resolution and drift-free detection of timing errors between two optical pulses. A single type-II phase-matched PPKTP crystal is used to construct a compact and self-aligned balanced optical cross-correlator for precise timing detection. Using this correlator, a 310 m long fiber link is stabilized with long-term sub-10 fs accuracy.

Optical subsampling downconverter for photonic analog-to-digital conversion of narrowband high-frequency microwave signals

Sampling and analog-to-digital conversion of high-frequency (>10 GHz) microwave signals is challenging due to the required aperture jitter below 100 fs. For example, sampling of 40 GHz signal with 8-bit resolution needs sub-10 fs timing jitter. Due to very low timing jitters from mode-locked lasers, photonic analog-to-digital converters (ADCs) have been strongly pursued.

In this thesis research, in close collaboration with Prof. Michael Perrott's group, an optical subsampling downconverter for analog-to-digital conversion of narrowband high-frequency microwave signals is studied. The demonstrated maximum signal to noise ratio (SNR) and signal to noise-and-distortion ratio (SNDR) of a 1-Mbps GMSK signal downconverted from a 9.5 GHz carrier are 32 dB and 22 dB over 2 MHz bandwidth, respectively. With improved optical components, the SNDR performance may reach up to 54 dB.

Chapter 2

Ultrafast Optical Signal Synthesis by Coherent Superposition of Mode-Locked Lasers

2.1 Motivation

Recent advances in few-cycle optical pulse technology initiated a new field of research, extreme nonlinear optics, which is the study of light-matter interactions depending on the carrier-envelope phase of the electric-field [28]. The representative example of such extreme light-matter interactions is high-harmonic generation (HHG) for extreme ultraviolet and soft x-ray pulse generation [9]. For further investigations and applications of such phase-sensitive phenomena [29, 30, 31, 32, 33, 34, 35, 36, 37], a single-cycle optical pulse, comprised of only one cycle of the light oscillation, is currently pursued in many laboratories.

Recently, single-cycle pulse trains spanning the visible to ultraviolet range have been generated by cascaded difference frequency generation of two Q-switched lasers with a vibrational transition in D_2 [38]. Broadband optical parametric amplification in BBO has been used to generate close to single-cycle optical pulses at 1 μm [39]. External compression techniques based on spectral broadening and adaptive disper-

sion compensation also generated sub-4 fs optical pulses approaching the single-cycle regime [40, 41, 42]. However, these systems are either very-high-repetition rate system with a pulse-to-pulse separation of only 11 fs [38] or low-repetition rate system with limited beam quality [39, 42]. An isolated, truly single-cycle optical pulse with excellent temporal and spatial quality has not been achieved to date.

The combination of phase-stabilized lasers has been long recognized as a way to synthesize ultrashort optical pulses with durations down to half an optical cycle using multiple single-frequency or mode-locked lasers (see Ref. [23] and references therein). To synthesize single-cycle optical pulses, several groups [43, 44, 45, 46, 47] have worked on the synthesis of optical combs spanning the visible to the infrared range from mode-locked Ti:sapphire and Cr:forsterite lasers. However, previous work could not synthesize single-cycle pulse due to their limited bandwidth and/or large residual timing/phase jitters and drifts.

Figure 2-1 shows the concept of phase-coherent superposition of two independent mode-locked lasers in (a) the frequency domain and (b) the time domain, with an example of a 5-fs Ti:sapphire laser (centered at 830 nm) and a 20-fs Cr:forsterite laser (centered at 1250 nm). In the frequency domain, to synthesize a phase-coherent frequency mode comb over the entire spectral range, the spacing (repetition rate, f_{rep}) and offset (carrier-envelope offset frequency, f_{ceo}) of each comb should be matched, i.e., $f_{rep1} = f_{rep2}$ and $f_{ceo1} = f_{ceo2}$. In the time domain, the envelope timing and the electric-field phase of each pulse should be matched. The envelope timing matching corresponds to the repetition rate synchronization (also simply called *timing synchronization*). The electric-field phase matching corresponds to the carrier-envelope offset frequency synchronization (also simply called *phase synchronization*). The resulting pulse has a constructive interfered peak part, while the wing parts are destructively interfered. This results in an effective shortening of the synthesized pulse.

The motivation of coherent pulse synthesis is not limited specifically to the single-cycle pulse generation. More generally, it forms the key technique to synthesize 'arbitrary' optical waveforms with special shapes of optical spectra [48] that a single mode-locked laser cannot generate. In addition, in optical timing distribution and

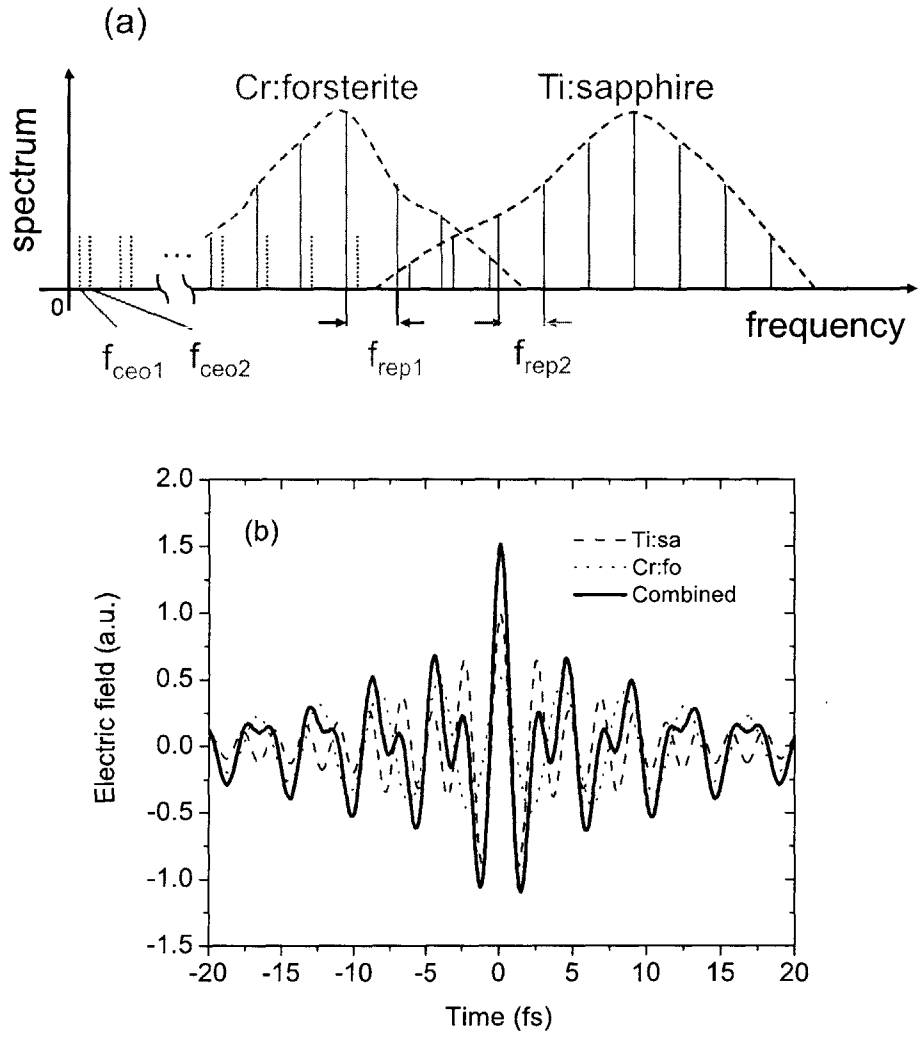

Figure 2-1: Phase-coherent superposition of two independent mode-locked lasers. (a) In frequency domain, the repetition rate f_{rep} and the carrier-envelope offset frequency f_{ceo} should be matched, i.e., $f_{rep1} = f_{rep2}$ and $f_{ceo1} = f_{ceo2}$. (b) In time domain, the pulse envelope and the electric-field phase should be aligned in such a way that the peak part is constructively interfered while the wing parts are destructively interfered.

synchronization systems shown in Section 1.2, tight optical-to-optical synchronization between different optical subsystems are required. Therefore, investigating the timing and phase locking mechanisms of the mode-locked lasers and developing new techniques for high-precision synchronization can provide very useful *toolbox* in the ultrafast science and technology.

2.2 System Overview

Figure 2-2 shows the schematic of the pulse synthesis system by coherent superposition of broadband mode-locked lasers. An ultrabroadband Ti:sapphire laser (Ti:sa in Fig. 2-2) and a broadband Cr:forsterite laser (Cr:fo in Fig. 2-2) are generating optical pulses with 600-1200 nm and 1100-1500 nm spectra, respectively. After their extra-cavity dispersion is precompensated (by $-GDD_1$ and $-GDD_2$ in Fig. 2-2), two pulses are combined at the ultrabroadband 50:50 beam splitter (Combining Beamsplitter in Fig. 2-2). Because this beamsplitter will act as an effective output coupler of the pulse synthesis system, it is very important to have well-controlled transmission (reflection) and dispersion characteristics over the whole combined spectral range (600-1500 nm). For the repetition rate (f_{rep}) synchronization, an optical technique named balanced optical cross-correlation is used to detect the timing error between two pulses with ultrahigh timing resolution and drift-free operation. Drift-free subfemtosecond synchronization is realized over 12 hours. Once a tight repetition rate synchronization is obtained, a heterodyne beat signal between the two lasers in the overlapped spectral range (at 1120 nm) is obtained. This beat signal corresponds to the difference in the carrier-envelope offset frequencies ($\Delta f_{ceo} = f_{ceo1} - f_{ceo2}$) of two lasers. When the beat signal is locked to DC by modulating the pump power of the Ti:sapphire laser with an acousto-optic modulator (AOM), it closes the pulse synthesis process. In the following sections, each of the key components and techniques will be explained.

In Section 2.3, the construction and measured performance of the ultrabroadband Ti:sapphire and Cr:forsterite lasers are presented. The intensity noise characteristics

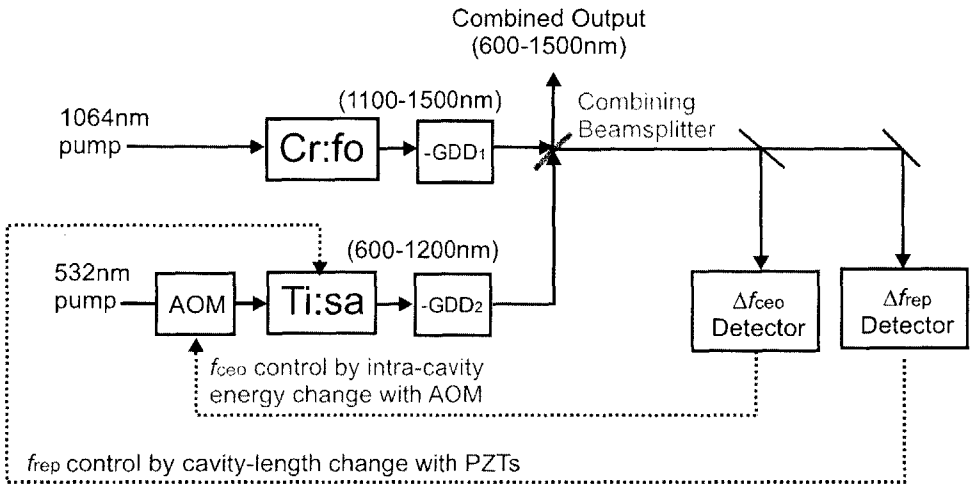

Figure 2-2: System overview of the pulse synthesis system by coherent superposition of two mode-locked lasers. Cr:fo, Cr:forsterite mode-locked laser; Ti:sa, Ti:sapphire mode-locked laser; $-GDD_1$, extra-cavity dispersion precompensation for Cr:forsterite laser; $-GDD_2$, extra-cavity dispersion precompensation for Ti:sapphire laser; Δf_{ceo}, difference in the carrier-envelope offset frequency between two lasers; Δf_{rep}, difference in the repetition rate between two lasers; AOM, acousto-optic modulator; PZT, piezoelectric transducer. Solid and dashed lines represent optical and electrical signal paths, respectively.

and its suppression with a noise eater follow in Section 2.4 In Section 2.5, the design and characterization of the ultrabroadband 50:50 beamsplitter with matched group delay dispersion are introduced. Subfemtosecond repetition rate synchronization with a balanced cross-correlator is explained in Section 2.6. Finally, carrier-envelope phase synchronization results are presented in Section 2.7.

2.3 Ultrabroadband Mode-Locked Lasers

Building stable and broadband mode-locked lasers with overlapping spectra is the first and still most important step in the pulse synthesis. To ensure long-term stable and broadband operation, both lasers were constructed as prism-less cavities. The intracavity dispersions were compensated by the combination of double-chirped mirrors (DCMs) [49] and thin wedges of glass material.

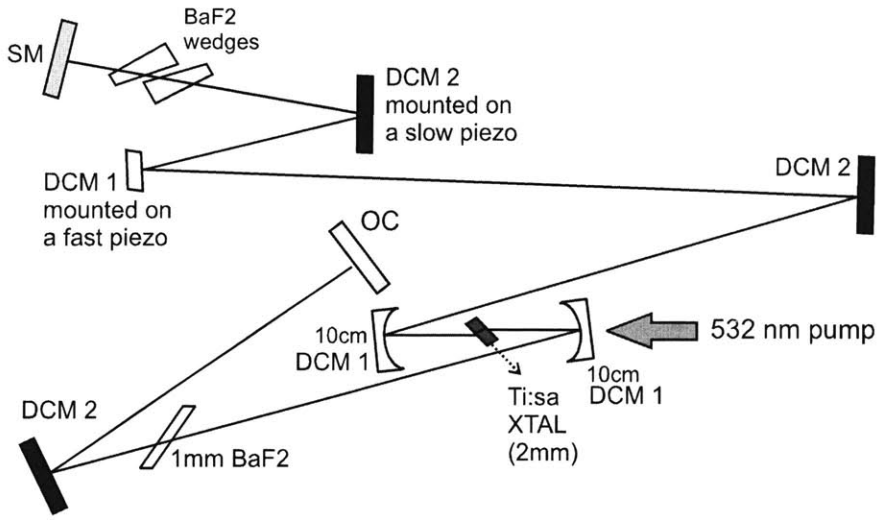

Figure 2-3: Schematic of the octave-spanning Ti:sapphire laser. DCM1, DCM7 type I; DCM2, DCM7 type II; SM, silver mirror; OC, output coupler.

2.3.1 Octave-Spanning Ti:sapphire Laser

Since its first Kerr-lens mode-locked operation in 1991 [50], the Ti:sapphire laser has revolutionized ultrafast optics. It can generate the shortest pulses (5 fs) and the broadest octave spanning spectrum (600-1200 nm) directly from the laser oscillator. It is a natural choice to use this laser for the single-cycle pulse synthesis experiment.

The Ti:sapphire laser design is similar to the previous prism-less designs in Refs. [12] and [51]. Figure 2-3 shows the schematic of the Ti:sapphire laser. The pulse generation mechanism is based on dispersion-managed mode-locking [52], and it is very important to keep the intra-cavity dispersion of the laser in a well-controlled way to generate the shortest pulses with the broadest spectrum. The negative group delay dispersion (GDD) is generated by dispersion compensating mirrors named double-chirped mirrors (DCMs) to compensate strong positive GDD of the laser crystal. Two types of DCMs (labelled as DCM1 and DCM2 in Fig. 2-3) are used in pairs to cancel the oscillation in the group delay (GD) by a phase shift of π between paired mirrors. As a result, the resulting group delay (GD) and the corresponding group delay dispersion (GDD) over an octave spectral range (600-1200 nm) have smooth profiles without oscillation as shown in Ref. [17]. The fine tuning of intra-cavity

dispersion is done by inserting and de-inserting a thin wedge of BaF_2. The use of BaF_2 is especially advantageous because 1 mm of BaF_2 has almost identical GDD as 1.85 m of air. The dispersion for the round trip of each arm with respect to the center of the Ti:sapphire crystal is balanced to achieve the broadest spectral output [52]. To lock the repetition rate of the laser, one small (3mm diameter) mirror is mounted on a fast piezoelectric transducer (PZT) and the other mirror is mounted on a slow PZT. Finally, the output coupler is fabricated with high index contrast material, ZnSe (n = 2.52)/MgF_2 (n = 1.38) Bragg stack to achieve broad spectral range.

The repetition rate of the Ti:sapphire laser is set to 81.7 MHz. It emits ~70 mW average power when pumped with 4.5 W from a 532 nm pump laser. The optical spectrum spans from 600 nm to over 1200 nm at -30 dB level from the peak (see Fig. 2-4 (a)) with a transform-limited pulsewidth of ~4 fs assuming zero phase over the entire spectrum. Figure 2-4 (b) shows the measured interference autocorrelation (IAC) trace. The pulse retrieval based on the Phase and Intensity from Correlation And Spectrum Only (PICASO) algorithm [53] shows that the retrieved pulsewidth is about 5.8 fs. It is longer than the transform limited pulsewidth, and imperfect extra-cavity dispersion compensation and residual intra-cavity nonlinear chirp might be the reason for this discrepancy.

The laser operation is very stable when the alignment is set at the right condition. Typically, the mode-locking was kept more than several hours in a routine way. This long-term stability of the laser enables more than 12 hours drift-free subfemtosecond timing synchronization, as will be shown in Section 2.6.

2.3.2 Broadband Cr:forsterite Laser

The Cr:forsterite laser, since its first lasing in 1988 [54], has attracted great interest as a broadband light source at 1.3 μm [55] for fiber optic characterization and biomedical imaging [56]. However, the starting and stabilization of Cr:forsterite mode-locked laser is known as difficult due to strong thermal loading and low gain of Cr:forsterite crystal [57, 58, 59, 60].

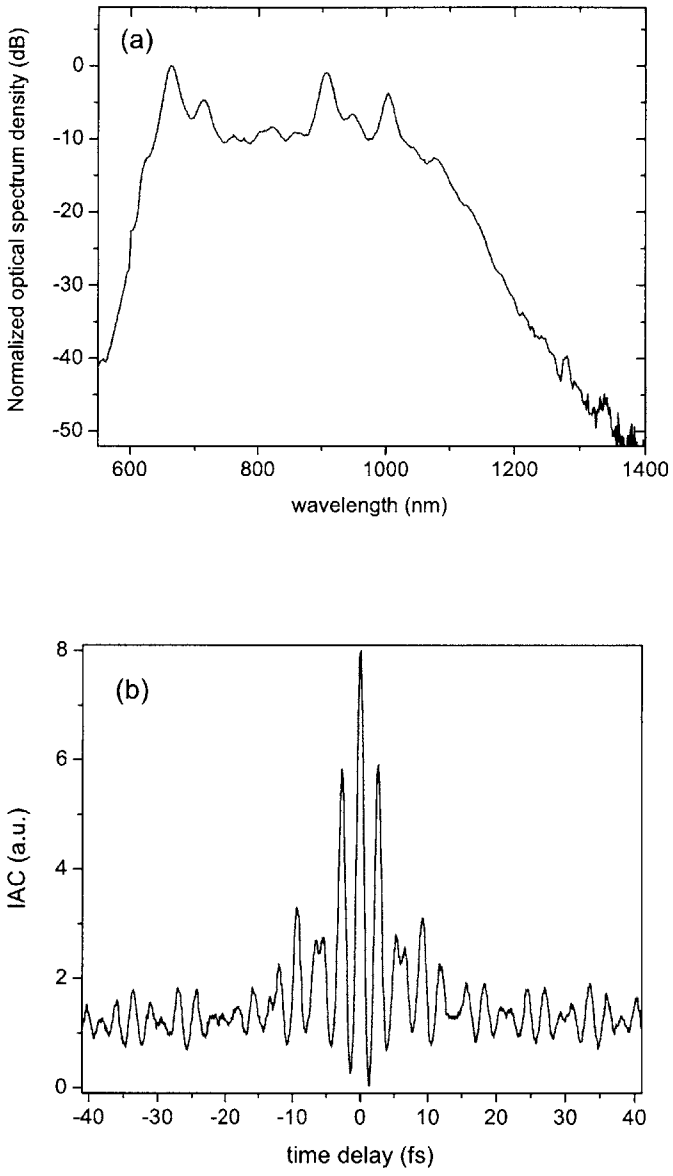

Figure 2-4: (a) Measured optical spectrum of the output from the Ti:sapphire laser. The spectrum spans octave from 600 nm to 1200 nm at the -30 dB level from the peak. The transform limited pulsewidth is ~4 fs. (b) Measured interference autocorrelation trace of the output from the Ti:sapphire laser. The retrieved pulsewidth is ~5.8 fs.

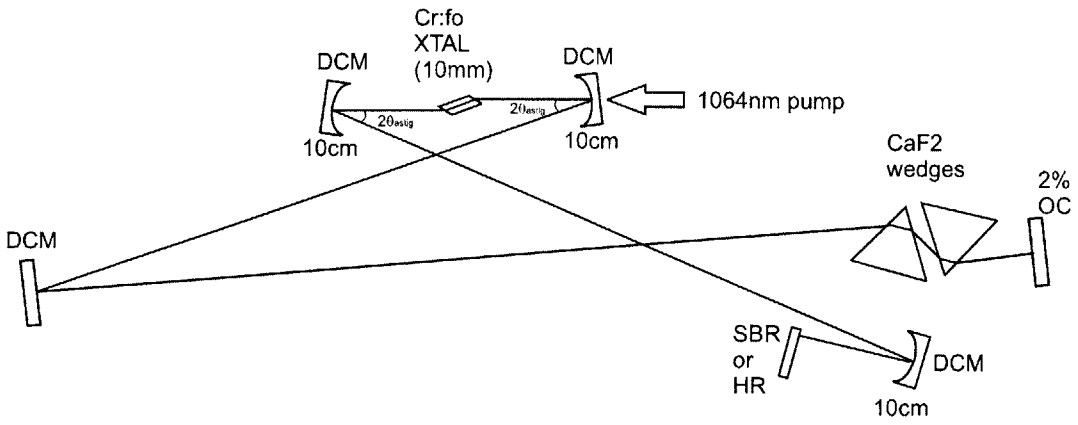

Figure 2-5: Schematic of the broadband Cr:forsterite laser. SBR, saturable Bragg reflector; HR, high reflectance mirror.

Despite of its difficulty in operation, the Cr:forsterite laser is still a very attractive choice to synchronize with the Ti:sapphire laser. Its broad spectral coverage from 1100 nm to 1500 nm enables 1.5 octaves when it is combined with the octave-spanning Ti:sapphire laser. Its spectral overlap in 1100-1200 nm range also enables an easy detection of the difference in the carrier-envelope offset frequency (Δf_{ceo}) between the two lasers.

The schematic of the broadband Cr:forsterite laser is shown in Fig. 2-5. Both the saturable absorber mode-locking by a saturable Bragg reflector (SBR) and the pure Kerr-lens mode-locking (KLM) are tested.

The use of a saturable absorber can greatly improve the stability of the mode-locked laser. An SBR made of a broadband 40 nm thick InGaAs saturable absorber on a large area, high-index contrast AlGaAs/Al_xO_y mirror [61] is used at the one end of the cavity. The focus size onto the SBR is set to $\sim$300 μm diameter.

The KLM can, in general, achieve the shortest output pulse with the broadest spectrum from the mode-locked laser. By replacing the SBR to the high reflecting mirror and changing the laser cavity condition to the inner edge of the outer stability region, a KLM based Cr:forsterite laser is built and tested.

The used Cr:forsterite crystal (from Scientific Materials Inc) has a length of 10 mm. The crystal length is five times longer than the Ti:sapphire case mainly because

of the low gain of the Cr:forsterite material. To avoid the effect of thermal loading and lensing in the crystal, it is cooled to 5 °C. The CaF_2 wedges are used to fine-tune the intra-cavity dispersion, similar to the case of BaF_2 wedges in the Ti:sapphire laser. More detailed information on designing and building Cr:forsterite lasers can be found in Ref. [62].

When it is mode-locked, the laser emits ~40 mW (SBR-ML case) and ~60 mW (KLM case) of average power when pumped with 6 W from a 1064 nm pump laser. The output power difference between SBR-ML case and KLM case originates from the insertion loss of the SBR (about 1-2 %). Figure 2-6 (a) shows the optical spectrum for SBR-ML and pure KLM cases. For both conditions, the 3-dB bandwidth is about 90 nm, corresponding to a transform-limited pulsewidth of ~21 fs. This is one of the broadest spectra achieved with SBR-ML mechanism from the Cr:forsterite laser [63]. It is believed that the SBR-ML laser is further assisted by the KLM, and this leads to as much broad spectrum as the pure KLM laser. Figure 2-6 (b) shows the measured IAC trace. The retrieved pulsewidth using the PICASO algorithm shows that the pulsewidth is about 26 fs. The nonlinear spectral chirp built in the laser cavity is responsible for this pulsewidth discrepancy. This can be fixed by a proper extra-cavity compensation. For the pulse synthesis system, the SBR-ML Cr:forsterite laser is used. It is self-starting and much more robust than the pure KLM case, with broad optical spectrum over 90 nm bandwidth. With the help of the SBR, the laser can be routinely operated over 12 hours time scale.

2.3.3 Extra-Cavity Dispersion Precompensation

For a pulse synthesis in the time domain, the extra-cavity dispersion must be compensated. In this system, the dispersion is precompensated before the pulses from each laser are combined. This enables easier dispersion compensation by use of chirped mirrors and glass plates than in the overall combined output over 1.5 octaves.

For the Ti:sapphire laser, extra-cavity dispersion between the laser output and the pulse characterization setup is caused by 2.35 mm of fused silica (from substrates of output coupler and beamsplitters) and 3.73 m of air. The extra-cavity second order

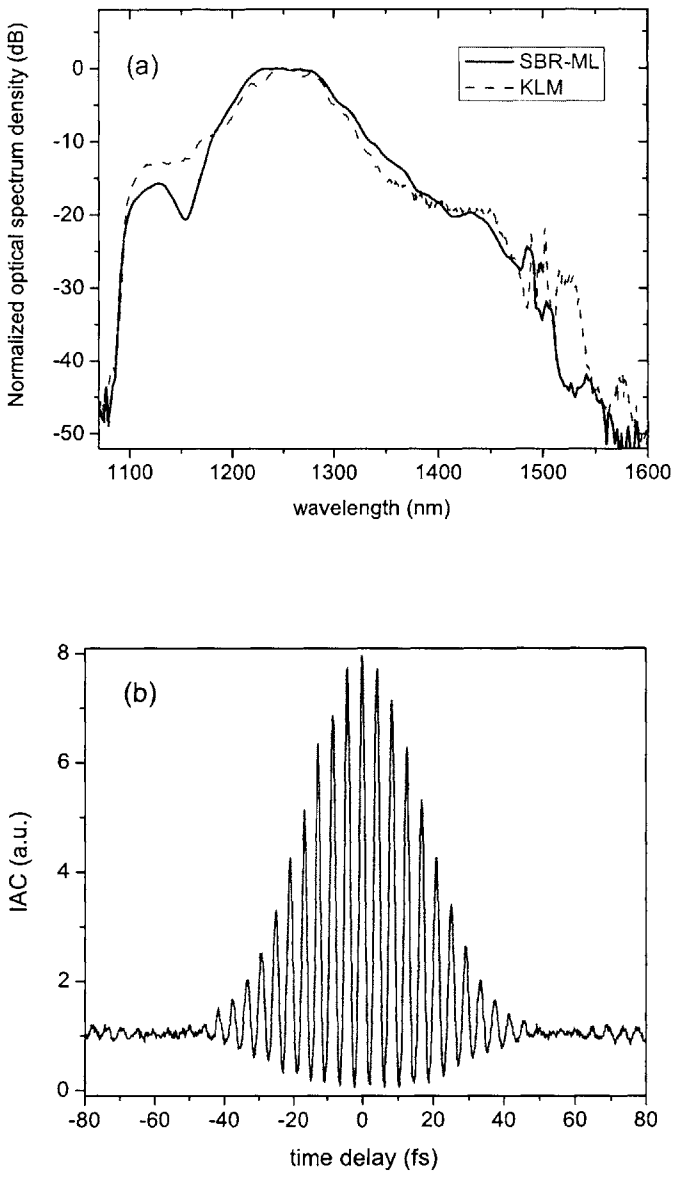

Figure 2-6: (a) Measured optical spectra of the output from the Cr:forsterite laser. The black-solid and red-dashed curves represent SBR-ML and KLM cases, respectively. For both cases, the spectra range from 1100 nm to 1500 nm at the -30 dB level from the peak. The transform limited pulsewidth is ~21 fs for the SBR-ML case. (b) Measured interference autocorrelation trace of the output from the Cr:forsterite laser when mode-locked by an SBR. The retrieved pulsewidth is ~26 fs.

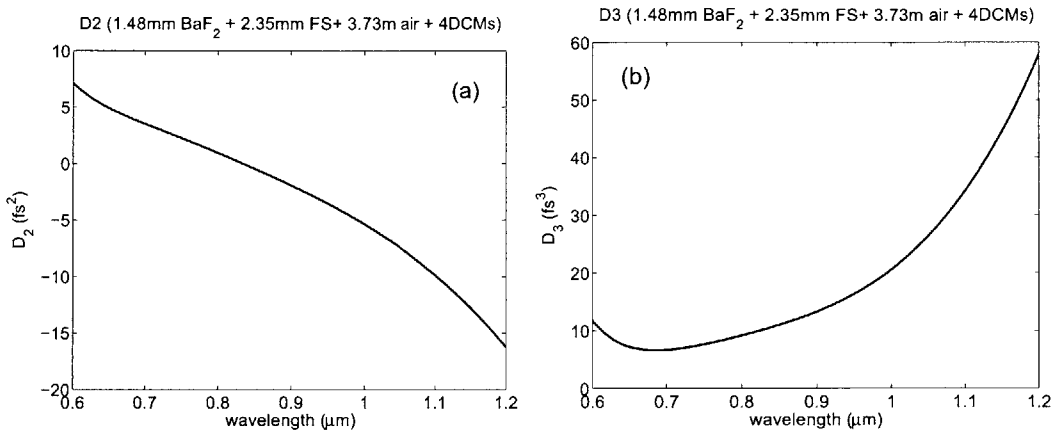

Figure 2-7: Extra-cavity precompensation calculation result for Ti:sapphire laser: (a) second order dispersion and (b) third order dispersion.

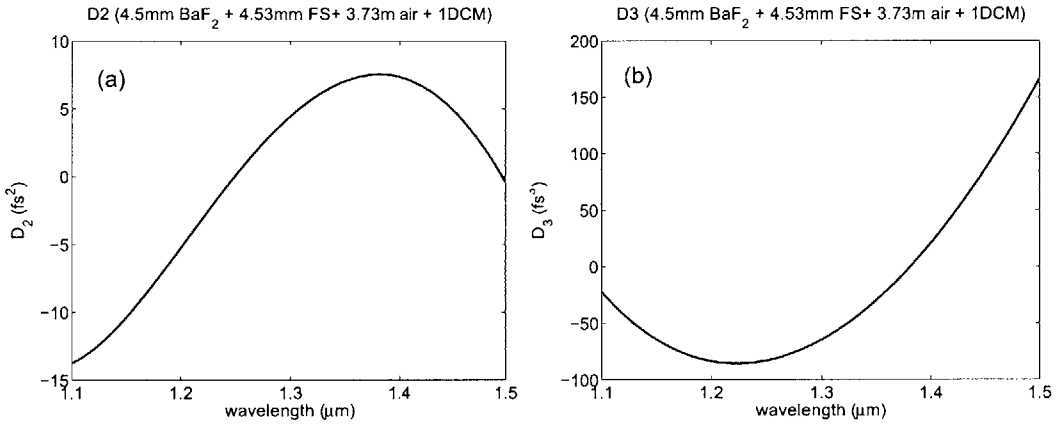

Figure 2-8: Extra-cavity precompensation calculation result for Cr:forsterite laser: (a) second order dispersion and (b) third order dispersion.

dispersion (D_2) is +190 fs^2 at 800 nm. The extra-cavity D_2 can be compensated within ± 10 fs^2 precision from 600 nm to 1100 nm using 4 bounces on DCMs (2 bounces on DCM1 and 2 bounces on DCM2) and 1.48 mm of BaF_2. Figure 2-7 shows the calculated (a) second order and (b) third order dispersion after compensation.

For the Cr:forsterite laser, 4.53 mm of fused silica and 3.73 m of air should be compensated. The corresponding D_2 is +60 fs^2 at 1250 nm. By use of 4.5 mm of BaF_2 and one bounce on the DCM for a Cr:forsterite laser, the D_2 can be compensated within ± 10 fs^2 from 1150 nm to 1500 nm. Figure 2-8 shows the calculated (a) second

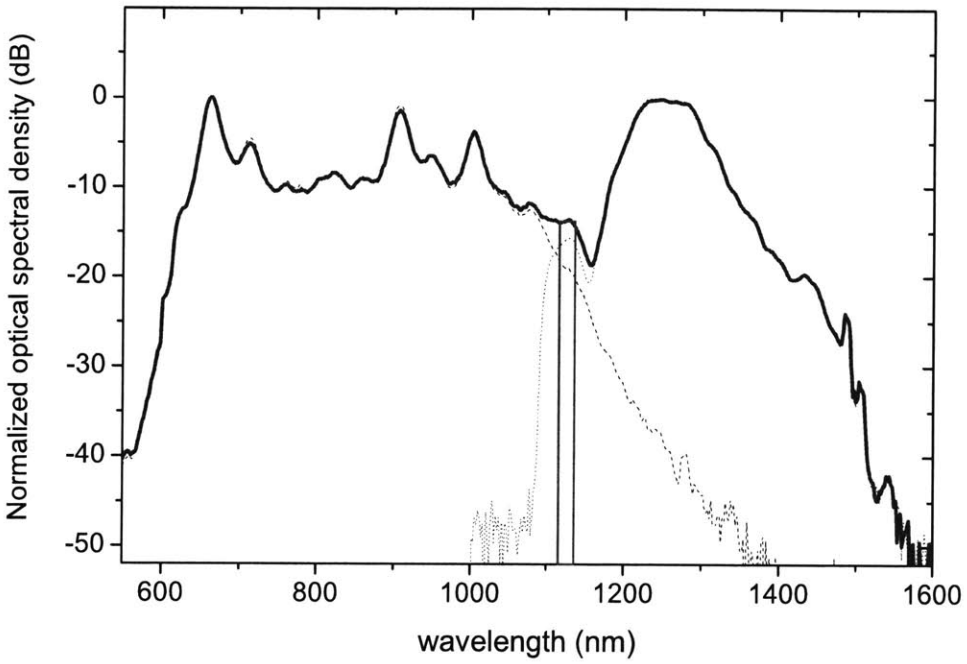

Figure 2-9: Combined optical spectra from Ti:sapphire and Cr:forsterite lasers. The red box (15nm wide, centered at 1120 nm) indicates the spectral range where the heterodyne beatnote between the two lasers is measured.

order and (b) third order dispersion after compensation.

2.3.4 Combined Optical Spectra

With a 50:50 ultrabroadband beamsplitter (presented in Seciton 2.5), the two pulsed beams from the Ti:sapphire and Cr:forsterite lasers are spatially combined. The combined spectrum spans 1.5 octaves from 600 nm to 1500 nm at -30 dB level measured from the peak. There is a strong spectral overlap in wavelength range 1100-1200nm, which enables a simple direct detection of the difference in carrier-envelope offset frequency (Δf_{ceo}) without using $1f$-$2f$ or $2f$-$3f$ interferometers [47]. The transform-limited pulse width of the combined spectra is about 3 fs. At the center wavelength 1 μm, this corresponds to less than one cycle of the light oscillation ($\sim$0.9 cycles).

2.4 Intensity Noise Characteristics and Noise Eater

For subfemtosecond timing and phase synchronization, the intrinsic noise of the free-running Ti:sapphire and Cr:forsterite laser should be minimal. In particular, the contribution from high frequency noise beyond the PZT and AOM bandwidths (~100 kHz) should be subfemtosecond range for both timing and phase jitters. The noise contribution is up to a few times of the relaxation oscillation frequency of the laser [64]. Since the relaxation oscillation frequencies are roughly 70 kHz and 140 kHz for Ti:sapphire and Cr:forsterite lasers respectively [44], the noise contribution above 1 MHz is negligible. This result is confirmed by the relative intensity noise (RIN) measurement in the next subsection.

The major contribution is from the amplitude-to-timing/phase conversion of the intensity noise of pump laser into the timing and phase jitters in the laser oscillator. These processes are formulated in Appendix A, and the impacts of intra-cavity energy change on the carrier-envelope offset frequency and repetition rate are formulated in Eqs. (A.12) and (A.14). It is important to characterize the intensity noise of the pump lasers and reduce it as much as possible to reduce residual timing/phase jitter. In Section 2.4.1, the RINs of 532nm pump laser (for Ti:sapphire laser), Ti:sapphire laser output, 1064nm pump laser (for Cr:forsterite laser) and Cr:forsterite laser output are measured. Since the noise contribution is dominant from the 1064nm pump laser, in Section 2.4.2, a "noise eater" is designed and implemented to reduce the intensity noise.

2.4.1 Relative Intensity Noise (RIN) of Lasers

The relative intensity noise (RIN) is defined as

$$RIN = \frac{< p_{rin}^2(t) >}{< P_0 >^2} \tag{2.1}$$

where the total optical power is $p_o(t) =< P_0 > + p_{rin}(t)$ with $< p_{rin}(t) >= 0$ [65].

The RINs of the 532 nm frequency-doubled Nd:YVO_4 laser (Ti:sapphire pump

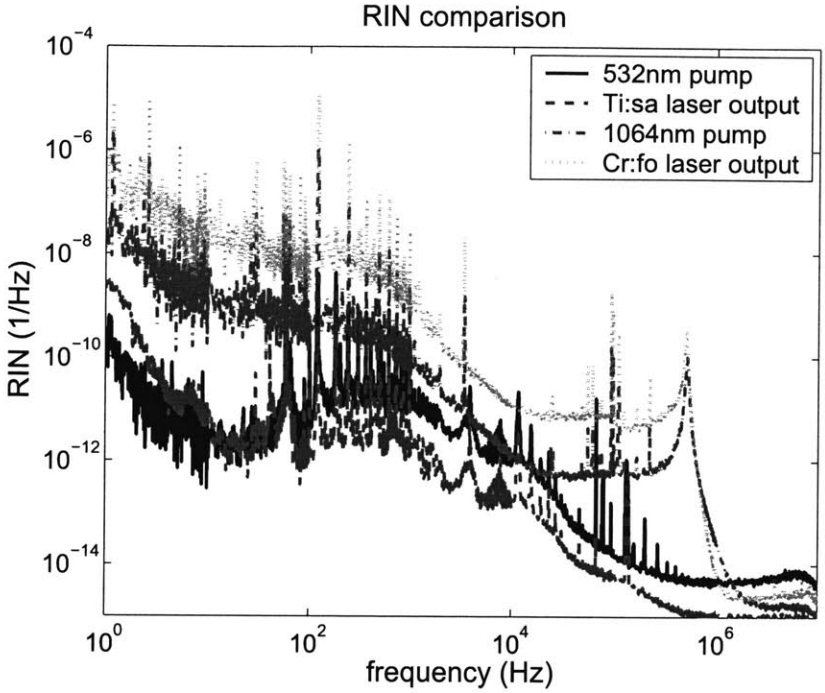

Figure 2-10: Relative intensity noise (RIN) of 532nm pump laser (for Ti:sapphire laser), Ti:sapphire laser output, 1064nm pump laser (for Cr:forsterite laser) and Cr:forsterite laser output.

laser) and the Ti:sapphire laser are measured with a 10 MHz bandwidth amplified Si-photodetector. The RINs of the 1064 nm Nd:YVO_4 laser (Cr:forsterite pump laser) and the Cr:forsterite laser are measured with a 10 MHz bandwidth amplified InGaAs-photodetector. Figure 2-10 shows the collection of measured RIN densities from 1 Hz to 10 MHz.

This measurement clearly shows that the 1064nm pump laser has much higher intensity noise than the 532nm pump laser. The integrated relative power fluctuation from 1 Hz to 1 MHz is 0.038 % and 0.3 % for the 532nm and 1064nm pump lasers, respectively. The integrated relative power fluctuations in the same bandwidth for the Ti:sapphire and Cr:forsterite lasers are 0.016 % and 0.85 %, respectively.

The perturbations in pump intensity cause fluctuations in amplitude, phase, center frequency and timing of the intra-cavity pulse. The dominating perturbation is the self-steepening of the pulse, and it was experimentally confirmed that the carrier-

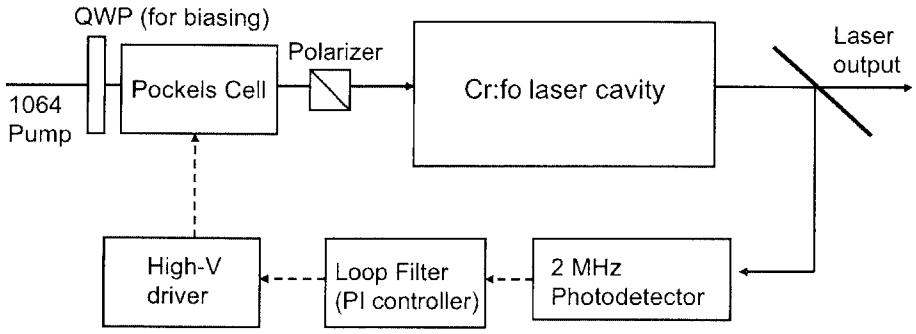

Figure 2-11: Schematic of the noise eater for the Cr:forsterite laser.

envelope offset frequency fluctuation is dominated by the amplitude-to-phase conversion of the pump intensity noise [66]. Therefore, one should keep the intensity noise from the pump laser as low as possible to achieve subfemtosecond synchronization between the two lasers. Because the intensity noise is dominated by the Cr:forsterite laser, in the next section, a noise eater is designed and implemented to suppress this intensity noise.

2.4.2 Noise Eater with a Pockels Cell

Figure 2-11 shows the schematic of the noise eater for Cr:forsterite laser. In essence it is an amplitude regulation feedback loop using an intensity modulator in the pump beam. Both electro-optic modulator (EOM) and acousto-optic modulator (AOM) can be used for intensity modulation. An EOM-type modulation is chosen to enable broadband operation because an AOM limits a feedback bandwidth less than 100 kHz caused by a phase shift from the travelling time of acoustic waves. Although the EOM provides enough bandwidth, the commercially available intensity-modulating EOMs turned out to be unsuitable due to their limited aperture sizes and severe thermal problems that prevent a stable operation of the Cr:forsterite laser. To implement the intensity modulation, a Pockels cell biased by a quarter-wave plate (QWP) is used. The use of QWP for the biasing enables the operation of the Pockels cell at the zero voltage bias condition and remove high voltage (>1 kV) biasing of the Pockels cell. This simplifies the driving of the Pockels cell.

Here, the biasing of the Pockels cell and the modulation slope are derived using Jones matrices calculation. The Jones matrix of each component is

QWP

$$Q_{\varphi_q} = \frac{1}{\sqrt{2}} \begin{bmatrix} 1 + j\cos(2\varphi_q) & j\sin(2\varphi_q) \\ j\sin(2\varphi_q) & 1 - j\cos(2\varphi_q) \end{bmatrix} \tag{2.2}$$

where φ_q is the QWP angle,

Pockels cell

$$C_{\{\Gamma,\phi\}} = \begin{bmatrix} e^{j\frac{\Gamma}{2}}\cos^2\phi + e^{-j\frac{\Gamma}{2}}\sin^2\phi & j\sin(\frac{\Gamma}{2})\sin 2\phi \\ j\sin(\frac{\Gamma}{2})\sin 2\phi & e^{j\frac{\Gamma}{2}}\sin^2\phi + e^{-j\frac{\Gamma}{2}}\cos^2\phi \end{bmatrix} \tag{2.3}$$

where Γ is the phase difference between the fast and slow axes and ϕ is the orientation angle of the Pockels cell,

Polarizer

$$P_\theta = \begin{bmatrix} \cos^2\theta & \cos\theta\sin\theta \\ \cos\theta\sin\theta & \sin^2\theta \end{bmatrix} \tag{2.4}$$

where θ is the polarizer angle.

The overall Jones matrix of the QWP-Pockels cell-polarizer (x-axis polarized) is

$$P_0CQ = \frac{1}{\sqrt{2}} \begin{bmatrix} e^{j\frac{\Gamma}{2}}\cos^2\phi + e^{-j\frac{\Gamma}{2}}\sin^2\phi & j\sin(\frac{\Gamma}{2})\sin 2\phi \\ 0 & 0 \end{bmatrix} \begin{bmatrix} 1 + j\cos(2\varphi_q) & j\sin(2\varphi_q) \\ j\sin(2\varphi_q) & 1 - j\cos(2\varphi_q) \end{bmatrix}. \tag{2.5}$$

When $\phi = \pi/4$ and $\Gamma = KV$, where V is the driving voltage of the Pockels cell,

$$P_0CQ = \frac{1}{\sqrt{2}} \begin{bmatrix} \cos(\frac{KV}{2}) & j\sin(\frac{KV}{2}) \\ 0 & 0 \end{bmatrix} \begin{bmatrix} 1 + j\cos(2\varphi_q) & j\sin(2\varphi_q) \\ j\sin(2\varphi_q) & 1 - j\cos(2\varphi_q) \end{bmatrix}. \tag{2.6}$$

For the x-axis polarized input light, the projected output electric field is

$$\frac{1}{\sqrt{2}} \begin{bmatrix} \left(\cos(\frac{KV}{2}) - \sin(\frac{KV}{2})\sin(2\varphi_q)\right) + j\cos(\frac{KV}{2})\cos(2\varphi_q) \\ 0 \end{bmatrix}. \tag{2.7}$$

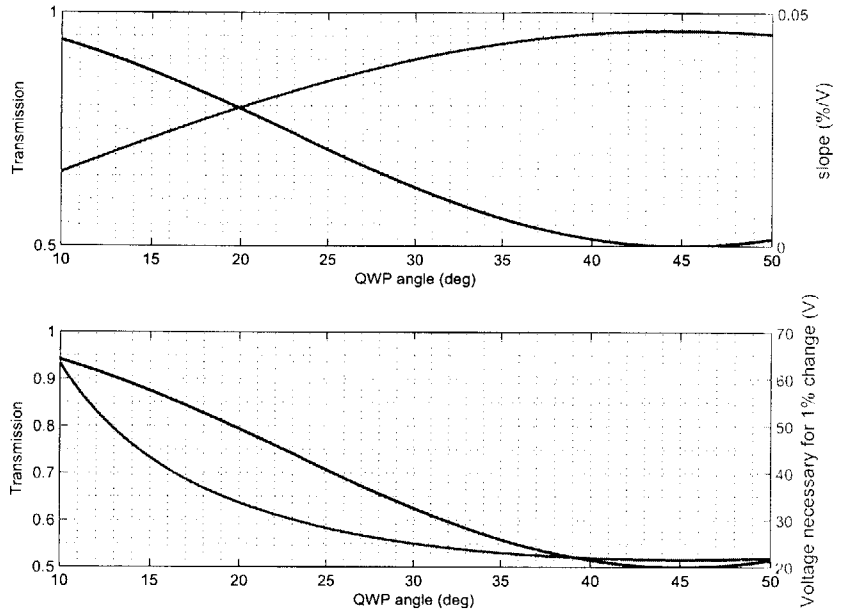

Figure 2-12: Calculated biasing condition and modulation slope as a function of QWP angle.

At V=0 (zero bias voltage), the power transmission is

$$T\Big|_{V=0} = \frac{|E_{out}|^2}{|E_{in}|^2}\Big|_{V=0} = \frac{1}{2}(1+\cos^2(2\varphi_q)), \tag{2.8}$$

and the modulation slope is

$$\frac{\partial T}{\partial V}\Big|_{V=0} = -\frac{K}{2}\sin(2\varphi_q) = -\frac{\pi}{2V_\pi}\sin(2\varphi_q). \tag{2.9}$$

Figure 2-12 shows the calculated transmission and modulation slope as a function of QWP angle (φ_q). The bottom figure shows the voltage necessary for 1 % transmission change when V_π is 3.4 kV.

Figure 2-13 shows the noise suppression result using a noise eater. In Fig. 2-13(a), the feedback bandwidth is only about 10 kHz. This is caused by the resonance at 100 kHz of the Pockels cell. The used DKDP Pockels cell has piezoelectric resonances which prevent increasing the gain beyond 100 kHz. The integrated noise from 100 kHz to 1 MHz contributes more than half of the total integrated noise from 10 Hz to

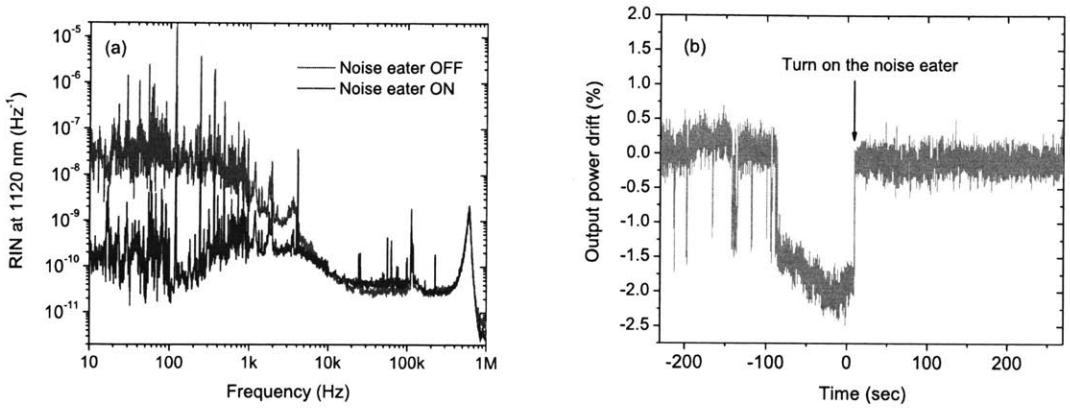

Figure 2-13: Noise suppression result by a noise eater. (a) RIN suppression of the Cr:forsterite laser output at 1120 nm. (b) Time-trace measurement of the Cr:forsterite laser output when the noise eater is on and off. Both are measured with a 10 MHz bandwidth InGaAs photodetector.

1 MHz, and it is important to extend this bandwidth up to 1 MHz to fully suppress the carrier-envelope offset frequency fluctuations originated from the intensity noise. A Pockels cell with an RTP or a BBO crystal with damped piezo resonances will be tested in the near future to avoid this bandwidth reduction by resonances. Although the high frequency part is not fully suppressed, the slow drift is well removed as shown in Fig. 2-13(b). Without noise eater, more than 2 % power change is observed in one minute. This power fluctuation can be removed by the noise eater.

2.5 Ultrabroadband Beam Splitter with Matched Group Delay Dispersion

2.5.1 Introduction

As the pulse width of femtosecond lasers becomes shorter and shorter, the spectral range increases dramatically. Currently, pulses with octave-spanning spectra in the range of 600-1200 nm can be directly generated from mode-locked lasers [1, 11, 12, 67]. The characterization of such extremely short pulses, comprised of less than

two cycles of light, using an interferometric auto-correlator (IAC) or the SPIDER-method [68] requires ultrabroadband beam splitters for combining and splitting the pulses without spectral and spatial distortions. Ultrabroadband beam splitters are also necessary for the pump-probe spectroscopy experiments with few-cycle optical pulses. Furthermore, for single-cycle optical pulse synthesis described in this Chapter, a beam splitter with well-controlled characteristics over the whole combined spectral range is necessary.

When the spectral range of interest increases beyond one octave, conventional metallic beam splitters show considerable loss and strong wavelength dependence in reflection and transmission due to the wavelength dependent penetration depth into the metal. Conventional dielectric beam splitters based on quarter-wave Bragg stacks cannot support such broad spectra. Therefore it is highly desirable to design a broadband beam splitter based on chirped multi-layer dielectric thin-film coatings deposited on a substrate.

For the pulse synthesis system shown in Fig. 2-2, the pulses from both lasers are combined at the beam splitter (labelled as "Combining Beamsplitter" in Fig. 2-2). The combination of both laser outputs by an in-loop beam splitter is of key importance for a long-term drift-free operation of the combined system. When the timing and phase locking loops are closed, this beam splitter will effectively serve as an output coupler of the pulse synthesis system. For efficient ultrabroadband pulse combining, we need not only constant reflectance and transmittance over the whole controlled spectral range but also well-controlled group delay dispersion (GDD) for any input-output combinations. These conditions are fulfilled, as will be shown later, by matching the dispersion in reflection from the coating with that of the single pass transmission through the substrate while keeping the coating reflection constant over the interested spectral range. In this section, a broadband 50:50 beam splitter (ranging 600-1500 nm) with matched group delay dispersion is designed, fabricated, and used for combining and splitting pulses in the coherent pulse synthesis setup. Furthermore, this 50:50 splitting ratio also enables the locking of the difference carrier-envelope frequency (Δf_{ceo}) via homodyne detection at the beam splitter,

which stabilizes the relative carrier-envelope phase in a long-term stable way as will be shown in Section 2.7.

2.5.2 Design Idea and Result

The design goal is a broadband beam splitter with a constant transmission (and reflection) and a well-controlled dispersion over the spectral range of interest identical for reflection or transmission through the beam splitter. This goal can be achieved when the GDD for reflection from the coating (from port 1 to port 4 in Fig. 2-14) is matched with the GDD for a single pass in the substrate. In this condition, the GDD for any combination of input and output can be matched over the whole wavelength range.

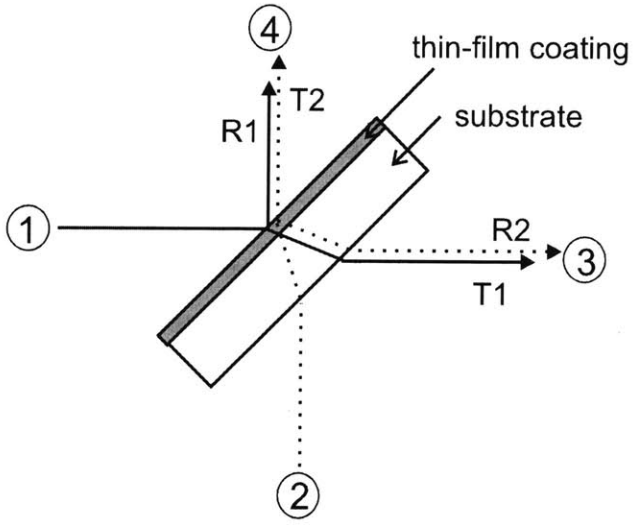

Figure 2-14: Schematic of a beam splitter.

Let us denote the GDD of the coating between the air and the substrate interfaces with reflection R1 (from port 1 to 4 in Fig. 2-14), transmission T1 (from port 1 to 3 in Fig. 2-14), reflection R2 (from port 2 to 3 in Fig. 2-14), and transmission T2 (from port 2 to 4 in Fig. 2-14) by GDD_{R1}, GDD_{T1}, GDD_{R2}, and GDD_{T2}, respectively. In the design we will match the group delay dispersion for a single-pass in the substrate, GDD_S, with that of the coating reflection, i.e., $GDD_S = GDD_{R1}$.

The GDD for each optical path through the total beam splitter, i.e., coating plus substrate, is then given by:

$$GDD(1 \rightarrow 4) = GDD_{R1} = GDD_S,$$
$$GDD(1 \rightarrow 3) = GDD_{T1} + GDD_S,$$
$$GDD(2 \rightarrow 3) = GDD_{R2} + 2GDD_S,$$
$$GDD(2 \rightarrow 4) = GDD_{T2} + GDD_S.$$

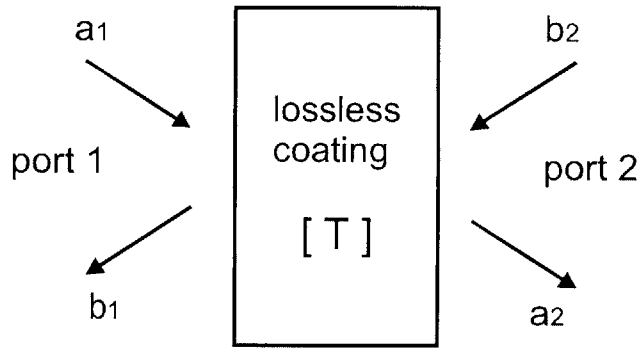

Figure 2-15: Lossless coating represented as a two-port system.

The transfer matrix for a lossless coating requires relationships between the group delay dispersion in reflection and transmission. The transfer matrix of a lossless coating described as a two-port system (see Fig. 2-15), is written as

$$\begin{bmatrix} a_1 \\ b_1 \end{bmatrix} = \begin{bmatrix} \frac{1}{t_1} & \frac{r_1^*}{t_1^*} \\ \frac{r_1}{t_1} & \frac{1}{t_1^*} \end{bmatrix} \begin{bmatrix} a_2 \\ b_2 \end{bmatrix}, \tag{2.10}$$

where r_1 and t_1 are the complex coefficients for reflection and transmission at port 1 assuming reflection free termination of port 2. Then the transmission and reflection coefficients and their phases at port 2 have a relationship with those at port 1

according to

$$t_2 = \left.\frac{b_1}{b_2}\right|_{a_1=0} = t_1, \qquad \phi_{t2} = \phi_{t1} \tag{2.11}$$

$$r_2 = \left.\frac{a_2}{b_2}\right|_{a_1=0} = -\frac{t_1 r_1^*}{t_1^*}, \qquad \phi_{r2} = 2\phi_{t1} - \phi_{r1} + \pi. \tag{2.12}$$

Since the GDD is determined by $GDD = -d^2\phi/d\omega^2$, the following relationships are generally valid for the lossless coating of the beam splitter in Fig. 2-14:

$$GDD_{T2} = GDD_{T1},$$
$$GDD_{R2} = 2GDD_{T1} - GDD_{R1}.$$

Finally, over the wavelength range of constant transmission, which is the condition we aim to achieve for broadband beam splitter, the GD for transmission through the coating, GD_{T1}, is almost constant because the transmission through a dielectric coating is subject to Kramers-Krönig relation [69]. Therefore, the corresponding GDD is negligible: $GDD_{T1} \simeq 0$.

With these additional conditions for a lossless and constant transmission coating, the GDD for each beam path becomes identical:

$$GDD(1 \rightarrow 4) = GDD_S,$$
$$GDD(1 \rightarrow 3) = GDD_{T1} + GDD_S = GDD_S,$$
$$GDD(2 \rightarrow 3) = GDD_{R2} + 2GDD_S = 2GDD_{T1} - GDD_{R1} + 2GDD_S = GDD_S,$$
$$GDD(2 \rightarrow 4) = GDD_{T2} + GDD_S = GDD_S.$$

Thus, the GDD from any input to any output is matched with the GDD from a single pass in the substrate, GDD_S. This well-controlled dispersion condition in transmission and reflection enables pre-compensation of the dispersion in the splitter for both output ports at the input port. Furthermore, one can easily show, under this design condition, that both output pulses (through port 3 and 4 in Fig. 2-14) are perfectly overlapped in time by properly choosing the delay between the two

input pulses. This characteristic makes this beam splitter attractive for coherent pulse synthesis with pulses from different femtosecond laser sources. In addition, a dielectric thin-film coating on a sufficiently thick substrate will ensure a long-term stable and spatially distortion-free operation.

For a specific device demonstration based on the design strategy described above, an ultrabroadband 50:50 beam splitter covering the spectral range of 600 nm to 1500 nm is designed. The design is carried out for p-polarized light with a 45° angle of incidence. The dielectric multi-layer thin film coating is deposited on a fused silica substrate. The fused silica substrate used in the design is about 655 μm thick, equal to a 750 μm (=655/cos(29.2°)) optical path length in the substrate for 45° angle of incidence. The design and optimizations are done with the OptiLayer thin film software [70]. The optimized coating consists of 38 layers of TiO_2 ($n \simeq 2.4$) and SiO_2 ($n \simeq 1.48$) on a fused silica substrate, and the total coating thickness is 3.54 μm. Figure 2-16 (a) and (b) show the designed reflectance/transmittance and GD in reflection and transmission from the coating, respectively. The designed reflectance and transmittance are within (50 ± 5) % from 600 to 1500 nm. The GD in coating reflection (solid line in Fig. 2-16(b)) is matched with that of the 750 μm optical path length of the fused silica substrate up to a constant (dot-dashed line in Fig. 2-16(b)), within ± 1 fs from 650 to 1500 nm. Fig. 2-16(b) demonstrates that the GDD in reflection from the coating is well matched with that of the substrate. The GD in coating transmission (dashed line in Fig. 2-16(b)) is constant centered at 20 fs (dotted line in Fig. 2-16(b)) within ± 1 fs from 650 to 1500 nm. The beam splitter is fabricated by ion-beam sputtering [71, 72] at NanoLayers GmbH to achieve the required precision on layer growth.

2.5.3 Characterization Results

Figure 2-17 (a) shows the designed and measured transmittance of a fabricated beam splitter. The transmittance was measured by a spectrophotometer under 45° angle of incidence. The design and measurement show excellent agreement. The slight difference between design and measurement might be attributed from the limited

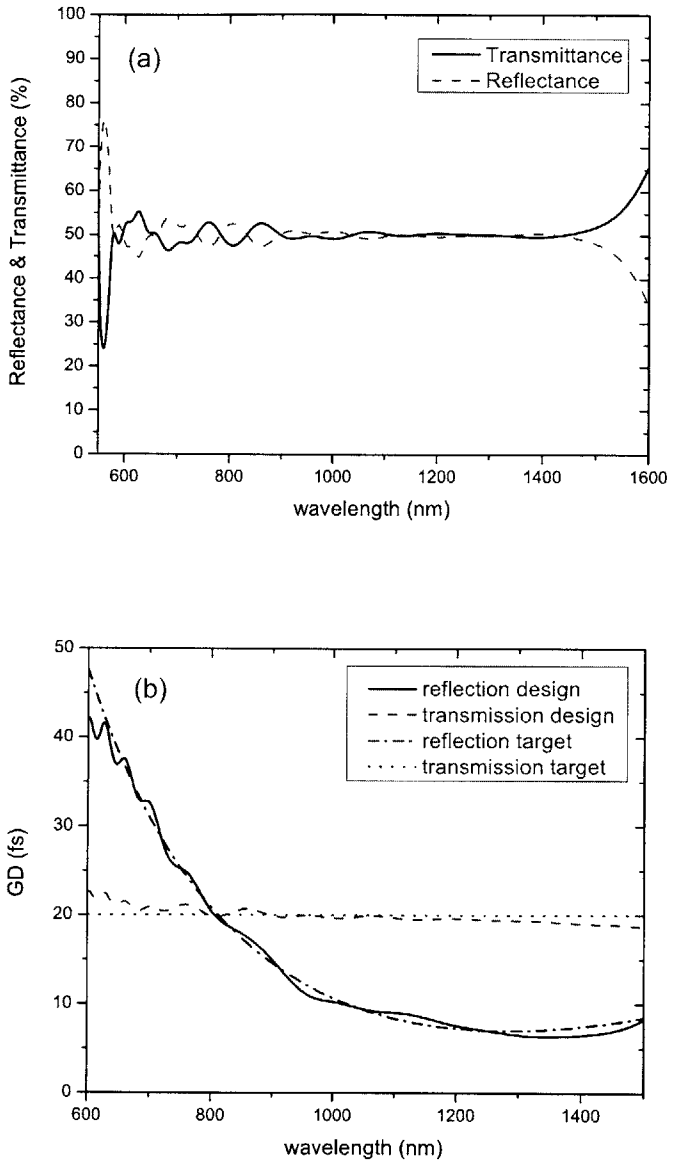

Figure 2-16: Beam splitter design results [73]. (a) Design result of transmission and reflection of coating. (b) Design result of group delay in reflection and transmission of coating.

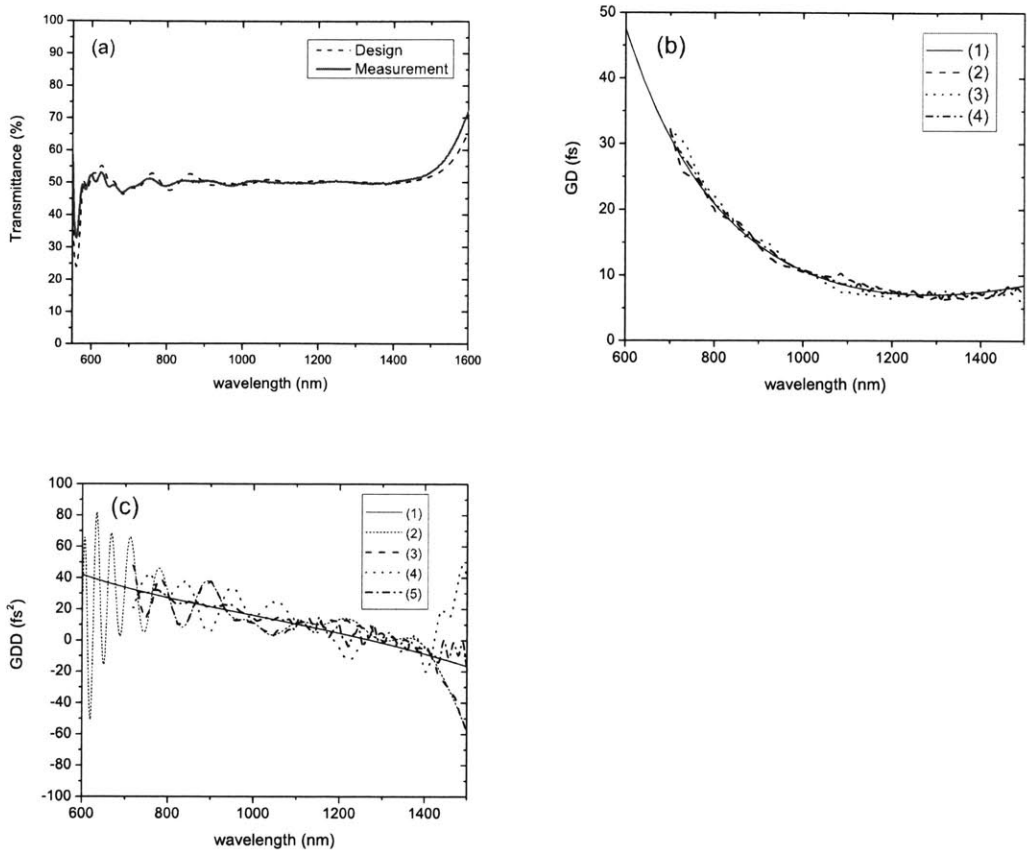

Figure 2-17: Beam splitter characterization results [73]. (a) Transmittance measurement result under p-polarized, 45 degrees incident angle. (b) Group delay (GD) measurement results: (1) design target (GD of 750 μm fused silica up to a constant); (2) measured GD of reflection from air side to coating; (3) measured GD of reflection from substrate side to coating; (4) measured GD of transmission through coating and substrate. (c) Group delay dispersion (GDD) measurement results: (1) design target (GDD of 750 μm fused silica); (2) design result of GDD in reflection from air side to coating; (3) measured GDD of reflection from air side to coating; (4) measured GDD of reflection from substrate side to coating; (5) measured GDD of transmission through coating and substrate.

incident angle accuracy of ±1.5 degrees. The GDs and corresponding GDDs were measured by a white light interferometer [74]. Figure 2-17 (b) shows the collection of all measured GDs for three possible cases: (i) reflection from air side to coating; (ii) reflection from substrate side to coating; (iii) transmission through coating and substrate. Since the measurements always involve two reflections or transmissions, the measurement results are divided by two when compared with the design. In addition, for an easy comparison with the design, the measured GD curves are shifted by a constant amount. The measurements were limited on the short wavelength side at 700 nm by the blocking filter for the 633 nm light from the He-Ne laser used for interferometer calibration. For all cases shown, the measured GDs and the corresponding GDDs show excellent agreement with the design. Figure 2-17 (c) shows the collection of measured GDDs with its design goal (GDD of 750 μm fused silica) and the design result of reflection from air side to coating. The measured result for reflection from air to coating is very well matched with the design. In all cases, the actual GDDs are in good agreement with the design goal within ±20 fs^2 deviation. Although the GDDs have some oscillations, the simulation shows that the reflected or transmitted pulse does not experience significant distortion from it.

2.6 Subfemtosecond Timing (Repetition Rate) Synchronization

2.6.1 Introduction

Timing synchronization of the pulse envelopes from each laser with sub-cycle timing fluctuation is one of the most important tasks in pulse synthesis. In the frequency domain, this corresponds to the repetition rate synchronization between two lasers. For high-quality pulse synthesis, it is desirable to have a residual timing jitter less than 1/10 of the optical cycle, e.g., 330 attoseconds (as, 10^{-18} sec) at 1 μm center wavelength, over full Nyquist bandwidth with a long-term drift-free operation.

Tight timing synchronization is necessary not only for the pulse synthesis but also

for synchronizing different optical systems in large-scale timing distribution systems. For example, the photo-injector laser, the seed laser and the probe lasers should be synchronized within drift-free sub-10 fs accuracy for the seeded x-ray free electron laser (XFEL) shown in Fig. 1-4.

Conventional repetition rate synchronization between two mode-locked lasers based on microwave mixers [75, 76] suffers from high residual jitter and thermal drifts in the electronic amplifiers and mixers. To overcome these limitations, together with former Postdoctoral Associate Thomas Schibli, a balanced optical cross-correlator [44] is proposed and demonstrated. This technique uses nonlinear optical processes for an extremely sensitive detection of timing differences between optical pulses.

2.6.2 Balanced Optical Cross-Correlator

Figure 2-18 shows the schematic of the balanced cross-correlator. The combined pulses from two mode-locked lasers with different spectra, denoted as wavelengths λ_1 and λ_2, are splitted by a broadband 50:50 beam splitter. The two beam paths have a different group delay (GD), for example, by inserting a glass plate in one of the arms. This group delay offsets the relative position between two pulses. Each combined pulse is focused into a nonlinear crystal to generate a sum-frequency component at $\frac{1}{\lambda_{SFG}} = \frac{1}{\lambda_1} + \frac{1}{\lambda_2}$. After bandpass filtering, the sum-frequency generation (SFG) components are detected by a balanced detector which measures the intensity imbalance. For small timing differences (within the range of the group delay of the GD element), the output from the balanced detector is proportional to the timing error between the two pulses. At the zero-crossing of the balanced detector output, the amplitude noise from each laser is balanced and does not affect the detected error signal. The signal from the balanced detector is used to lock the repetition rates of the two lasers by controlling the cavity length of one laser with cavity mirrors mounted on piezo-electric transducers (PZTs). This finally closes the loop. This method enables long-term drift-free timing synchronization between two independent lasers.

For the implementation of this balanced cross-correlator, lithium triborate (LBO) crystals with 1-mm thickness are used for SFG at 499 nm. The crystal is type-I SFG

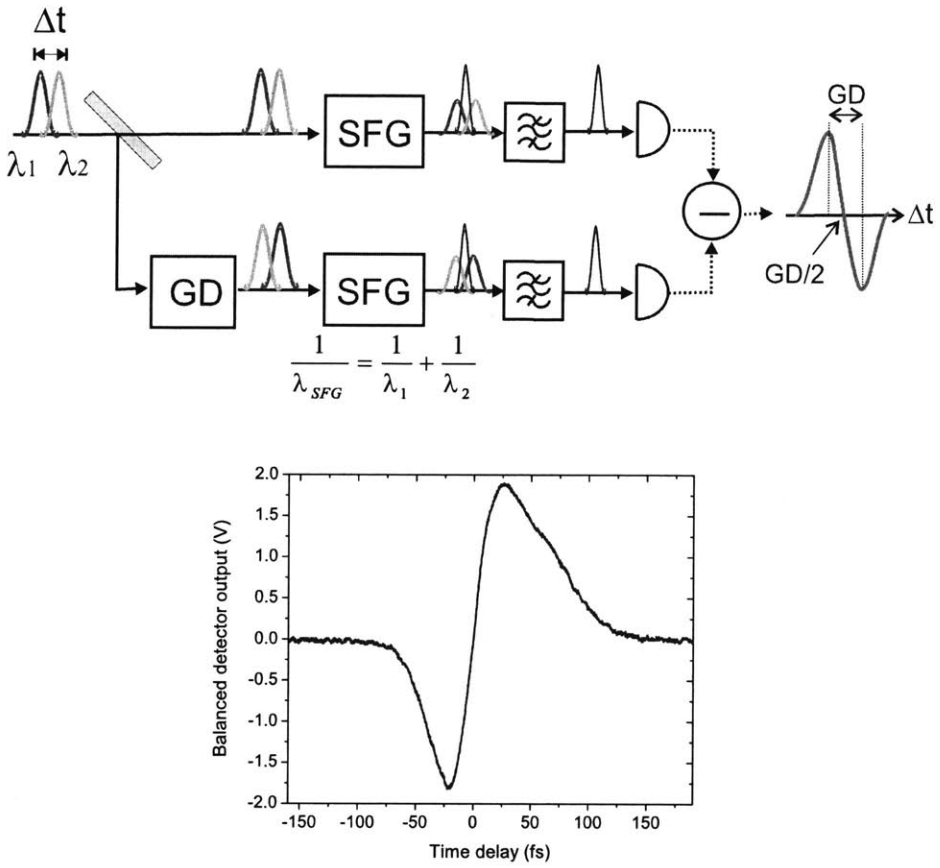

Figure 2-18: Schematic of a balanced cross-correlator. GD: group-delay element between two color pulses. SFG: sum-frequency generation. The graph shows a measured balanced cross-correlator output as a function of time delay between two pulses.

phase-matched between 830 nm from the Ti:sapphire laser and 1250 nm from the Cr:forsterite laser that results in SHG at 499 nm (1/830nm + 1/1250nm = 1/499nm). To generate a group delay offset of 48 fs between 830 nm and 1250 nm, a 3-mm thick fused silica plate is used. Because the dependence of chromatic dispersion on temperature is very small (<1 as/K) [44], the timing offset is well fixed at 48 fs without drift. The S-shaped graph in Fig. 2-18 shows the balanced detector output signal when the two lasers are not locked. The typical timing detection sensitivity is >150 mV/fs, that is >100,000 times more sensitive than that of typical microwave mixers. In addition, because the intensity noise is cancelled by the balanced detection, it is robust against amplitude noise and drifts. Finally, it can operate in a long-term stable way because of very small temperature dependence. Note that pure microwave locking techniques based on high-speed photodetectors and mixers suffer from large thermal drift (typical high-speed photodetector and mixer show >300 fs/K [25] and >70 fs/K [77] temperature sensitivities at 10 GHz), and cannot achieve a long-term drift-free operation over hours.

The error signal from the balanced detector is applied to the loop filter. The loop filter has fast and slow signal paths. The fast signal output is a PI controller that controls the fast PZT through a fast driver (home-built driver with THS6012 OP amp). The fast PZT loop with ~100 kHz bandwidth stabilizes the high frequency fluctuations. The slow signal output is applied to a slow PZT though a high voltage driver (1 kV driver based on the design at JILA) to compensate slow timing drift over long time scale. The bandwidth of the slow feedback loop is about 1 kHz. To get a lock, the loop gain of the fast PZT loop is set high enough to acquire locking condition. Once the locking is obtained, an integrator is turned on while the proportional gain is reduced until the oscillations by the fast PZT resonances are completely removed. At this condition, the slow PZT control loop is turned on and the slow loop gain is increased until the residual timing jitter is minimized. To enable high gain at the low frequency <1 kHz where the noise contribution is large while at the same time avoiding oscillations by the slow PZT, an additional lag compensation [78] RC-circuit is inserted in the slow loop. With the optimization of parameters (gains, positions

of poles and zeros) in both fast and slow loops, a very stable subfemtosecond timing lock is obtained over 12 hours as will be shown in the next section.

2.6.3 Measurement Results

To evaluate the out-of-loop residual timing jitter between two lasers, an out-of-loop cross-correlator with a BBO crystal and a 2.3-MHz bandwidth photodetector is built. The residual timing jitter depends on the intensity noise of Cr:forsterite laser and locking conditions such as the gains of fast and slow PZTs and corner frequencies, and needs to be optimized each time a new lock is obtained. As a result, the resulting timing jitter varies time to time. The typical timing jitter performance is between 300 as and 500 as. Figure 2-19 shows the representative out-of-loop timing jitter density when the two lasers are locked. The integrated timing jitter from 10 Hz to 1 MHz is 388 as. Most of the residual jitter originates from the peaks within ranges [300 Hz, 2 kHz] (250 as) and [100 kHz, 200 kHz] (100 as). This noise is mainly caused by the timing fluctuation converted from the intensity noise of 1064 nm pump laser. With a more broadband noise cater using a Pockels cell with damped piezo resonances, a much better timing lock performance is expected below 100 as.

Figure 2-20 shows the out-of-loop cross correrlation trace in the time domain. The black line shows the cross-correlation trace when the two lasers are not locked. The red line shows the cross-correlation trace when two lasers are locked adjacent to each other so that timing fluctuations are transferred into intensity fluctuations in the cross-correlation signal [76]. The pulse trains from the two lasers are locked with 380 $\pm$ 130 as rms timing jitter over 12 hours in the bandwidth from 20 μHz to 2.3 MHz. The indicated error is from the intensity noise contribution. Note that the duration of 12 hours does not constitute a limit to the locking scheme but was merely the duration of the experiment. In principle, as long as the lasers stay mode-locked, the timing lock can be maintained if the mechanical perturbations to the system are below a certain threshold value (the maximum displacement of the used PZT). To the best of my knowledge, this is the first time to demonstrate drift-free subfemtosecond timing synchronization performance over >12 hours time scale.

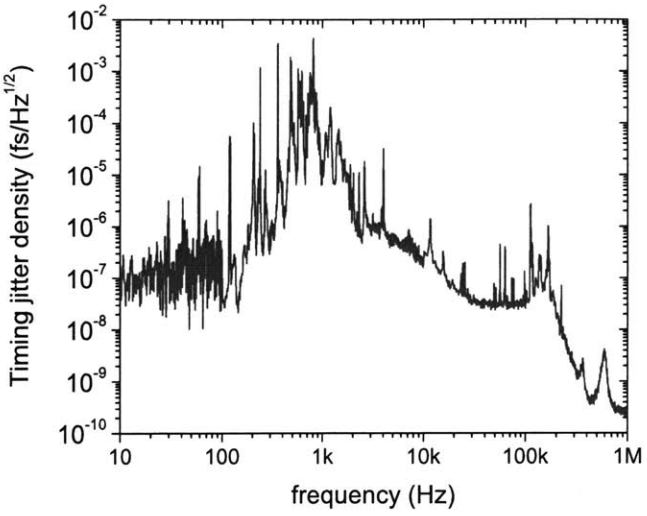

Figure 2-19: Residual out-of-loop timing jitter density measurement result between Ti:sapphire and Cr:forsterite lasers. The integrated timing jiter from 10 Hz to 1 MHz is 388 as. Most of the jitter is originated from the sharp peaks in [300 Hz, 2 kHz] and [100 kHz, 200 kHz] ranges.

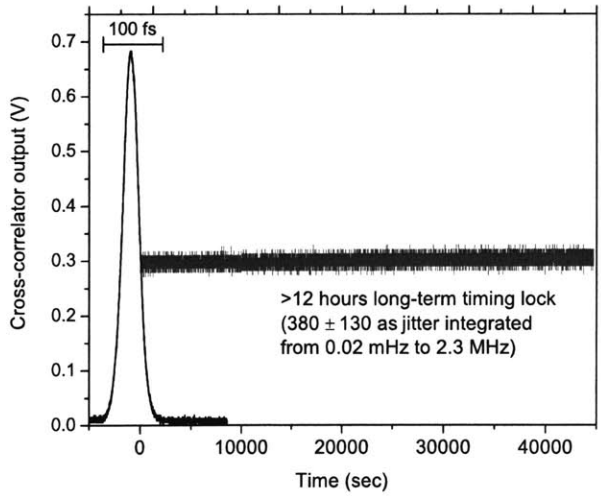

Figure 2-20: Long-term timing synchronization result between Ti:sapphire and Cr:forsterite lasers [79]. Drift-free subfemtosecond synchronization over 12 hours was observed.

Note that this subfemtosecond timing synchronization is also important for the large-scale timing distribution systems. In such systems, remotely located optical subsystems (mode-locked lasers) need to be tightly synchronized. This can be done by distributing the timing pulse train to remote locations via timing stabilized fiber links (described in Chapter 4) and synchronize this timing pulse trains with the output of the optical subsystems by use of balanced optical cross-correlators. This effectively results in remote synchronization of multiple optical subsystems and lasers in a long-term drift-free way.

2.7 Subfemtosecond Phase (Carrier-Envelope Offset Frequency) Synchronization

2.7.1 Detection of Carrier-Envelope Offset Frequency by Direct Photodetection of Overlapping Spectra

As soon as the tight timing synchronization is obtained, strong heterodyne beat signals are obtained in the overlap region of the optical spectrum (indicated as the red box in Fig. 2-9). To detect the difference in carrier-envelope offset frequency (Δf_{ceo}) between the two lasers, a 15 nm wide part of the spectrum in the overlap spectral range at 1120 nm is filtered out and detected with an InGaAs photodetector. Figure 2-21 shows the RF spectrum measured with a 1-GHz bandwidth InGaAs Avalanche photodetector (APD310 from MenloSystems). Heterodyne beatnotes ($mf_{\mathrm{R}} \pm \Delta f_{\mathrm{ceo}}$, m=integer) show 30 dB SNR measured with a 30 kHz resolution bandwidth. Because the spectral overlap is enough, a simple direct photodetection can be used rather than the more complex and alignment sensitive techniques such as $1f$-$2f$ or $2f$-$3f$ interferometers used in other experiments [47].

The last goal is to lock this heterodyne beatnote (Δf_{ceo}) to DC. To detect the Δf_{ceo} at the low frequency near DC, it is important to detect the beatnote with an amplitude-noise free detection scheme. The simple direct photodetection is sensitive to the RIN from each laser. To cancel the unwanted amplitude noise and detect the

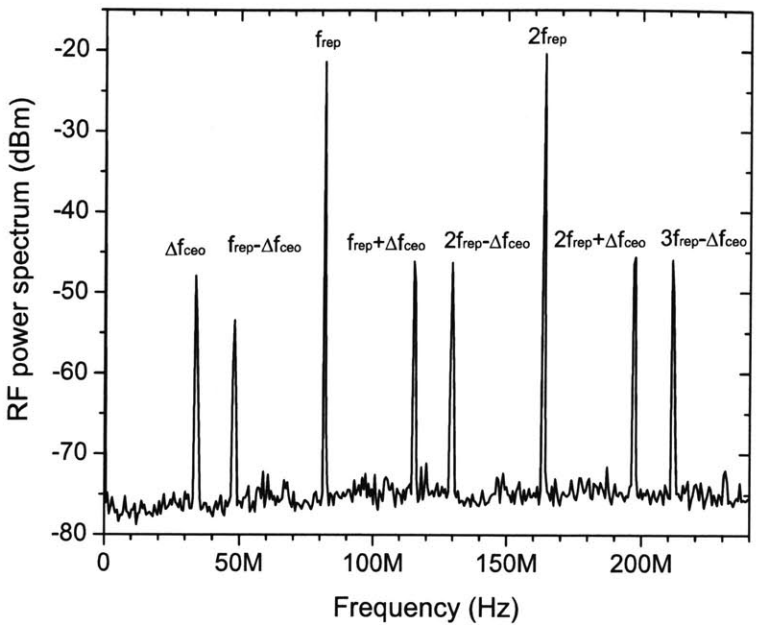

Figure 2-21: RF spectrum (RBW 30 kHz) of the beat signals from the InGaAs Avalanche photodetector output.

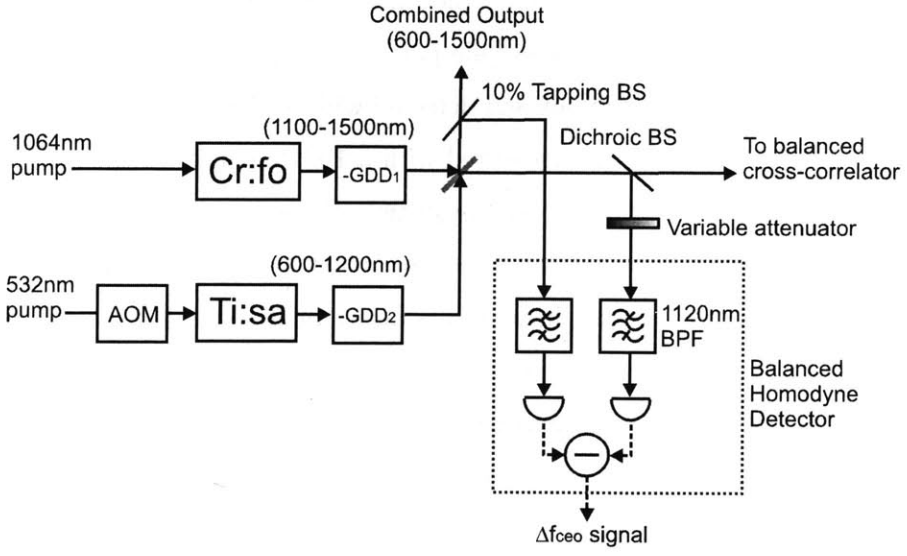

Figure 2-22: Schematic of the balanced homodyne detector for Δf_{ceo} detection. BS, beamsplitter; BPF, bandpass filter.

heterodyne beatnote with high sensitivity, balanced homodyne detection is demonstrated. Figure 2-22 shows the schematic of this homodyne detection.

In essence, by use of a lossless 50:50 beamsplitter, we can cancel the amplitude noise while keeping the f_{ceo} beatnote. It is possible by the 90° phase shift between transmitted and reflected electric fields at the beamsplitter.

A more detailed derivation is presented in the following. We can write the electric field of the optical pulses from each laser as

$$E_C(t) = \hat{E}_C(t)e^{j2\pi f_C t} + n_C(t), \tag{2.13}$$

$$E_T(t) = \hat{E}_T(t)e^{j2\pi f_T t} + n_T(t), \tag{2.14}$$

where $E_C(t)$ is the total electric field, $\hat{E}_C(t)$ is the pulse train envelope, f_C is the center frequency, and $n_C(t)$ is the amplitude noise of the optical pulse from the Cr:forsterite laser. In the same manner, the parameters in Eq. (2.14) are defined for the Ti:sapphire laser.

When these pulses are combined by a perfect lossless 50:50 beamsplitter, i.e., the reflectivity is $r = -\frac{1}{\sqrt{2}}$ and the transmittivity is $t = j\frac{1}{\sqrt{2}}$ [80], the combined field at each arm is expressed as

$$E_1(t) = \frac{1}{\sqrt{2}}\left[-\left(\hat{E}_C(t)e^{j2\pi f_C t} + n_C(t)\right) + j\left(\hat{E}_T(t)e^{j2\pi f_T t} + n_T(t)\right)\right] \tag{2.15}$$

$$E_2(t) = \frac{1}{\sqrt{2}}\left[-\left(\hat{E}_T(t)e^{j2\pi f_T t} + n_T(t)\right) + j\left(\hat{E}_C(t)e^{j2\pi f_C t} + n_C(t)\right)\right] \tag{2.16}$$

When each combined beam passes through a narrowband optical filter that transmits only a small range of wavelength in the overlapped spectrum (in this experiment, 15nm wide part centered at 1120 nm),

$$E_1'(t) = \frac{1}{\sqrt{2}}\left[-\left(\hat{E}_C'(t)e^{j2\pi f_C' t} + n_C'(t)\right) + j\left(\hat{E}_T'(t)e^{j2\pi f_T' t} + n_T'(t)\right)\right] \tag{2.17}$$

$$E_2'(t) = \frac{1}{\sqrt{2}}\left[-\left(\hat{E}_T'(t)e^{j2\pi f_T' t} + n_T'(t)\right) + j\left(\hat{E}_C'(t)e^{j2\pi f_C' t} + n_C'(t)\right)\right] \tag{2.18}$$

where $\hat{E}_C'(t)$ and $\hat{E}_T'(t)$ are the filtered pulse train envelope functions, $n_C'(t)$ and $n_T'(t)$ are the filtered amplitude noise, and $f_C' = mf_{rep} + f_{ceo}^{Cr:fo}$ and $f_T' = mf_{rep} + f_{ceo}^{Ti:sa}$ are the mode comb frequencies at the center of filtered spectral region.

The photocurrent at each photo detector that is low-pass filtered at $f_{rep}/2$ is expressed as

$$\begin{aligned}\langle I_1(t)\rangle_{f<f_{rep}/2} &= \int\left|\frac{1}{\sqrt{2}}\left[-\left(\hat{E}_C'(t)e^{j2\pi f_C' t} + n_C'(t)\right) + j\left(\hat{E}_T'(t)e^{j2\pi f_T' t} + n_T'(t)\right)\right]\right|^2 dt \\ &= \frac{1}{2}\left[|\hat{E}_C'|^2 + |\hat{E}_T'|^2 + 2|\hat{E}_C'||\hat{E}_T'|\sin(2\pi\Delta f_{ceo}t) + \langle n'^2\rangle\right] \end{aligned} \tag{2.19}$$

$$\begin{aligned}\langle I_2(t)\rangle_{f<f_{rep}/2} &= \int\left|\frac{1}{\sqrt{2}}\left[-\left(\hat{E}_T'(t)e^{j2\pi f_T' t} + n_T'(t)\right) + j\left(\hat{E}_C'(t)e^{j2\pi f_C' t} + n_C'(t)\right)\right]\right|^2 dt \\ &= \frac{1}{2}\left[|\hat{E}_C'|^2 + |\hat{E}_T'|^2 - 2|\hat{E}_C'||\hat{E}_T'|\sin(2\pi\Delta f_{ceo}t) + \langle n'^2\rangle\right] \end{aligned} \tag{2.20}$$

where $|\hat{E}_C'|$ and $|\hat{E}_T'|$ are the DC amplitude of filtered Cr:fo and Ti:sa pulses, Δf_{ceo} is the difference in the carrier-envelope offset frequency $\Delta f_{ceo} = f_{ceo}^{\text{Ti:sa}} - f_{ceo}^{\text{Cr:fo}}$, and $n'^2 = |n_C'|^2 + |n_T'|^2 + j(n_C' n_T'^* - n_C'^* n_T')$. The photodiode responsivity and scaling factors such as characteristic impedances are normalized for simplicity.

The output of the detector is the difference of the two photocurrents, $\langle I_1\rangle - \langle I_2\rangle$.

$$\langle I_{out}(t)\rangle_{f<f_{rep}/2} = \langle I_1(t)\rangle - \langle I_2(t)\rangle = 2|\hat{E}_C'||\hat{E}_T'|\sin(2\pi\Delta f_{ceo}t) \tag{2.21}$$

The DC components as well as the amplitude noise from both lasers are cancelled by the balanced detection. Only the beat frequency component that we aim to detect remains. Further, this beat frequency corresponds to the difference in the carrier-envelope offset frequency, $\Delta f_{ceo} = f_{ceo}^{\text{Ti:sa}} - f_{ceo}^{\text{Cr:fo}}$.

The balanced homodyne detector is implemented as Fig. 2-22. The ultrabroadband 50:50 beamsplitter (shown in Sec. 2.5) is used for the 'lossless' 50:50 beamsplitter. From the combined output arm, 10% of light is tapped off by a tapping

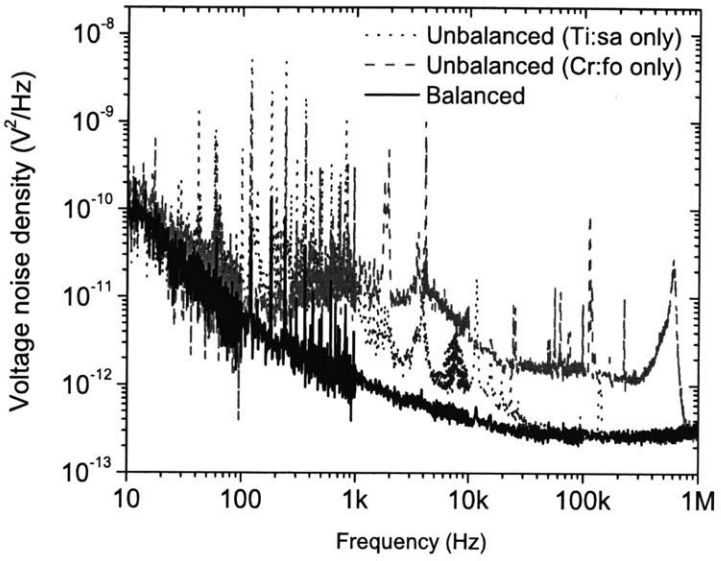

Figure 2-23: Intensity noise cancellation by a balanced homodyne detector.

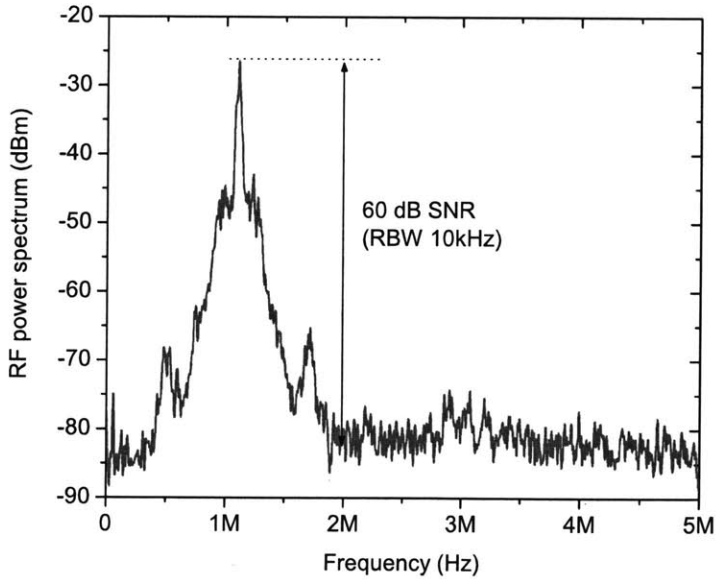

Figure 2-24: Heterodyne beatnote detected by balanced homodyne detector with a 60 dB signal-to-noise ratio.

beamsplitter (a single layer of 100.5 nm thick Ta_2O_5 on a 0.5mm thick fused silica substrate). From the other arm to the balanced cross-correlator, 1120 nm component is tapped off by a dichroic beamsplitter that transmits 830 nm and 1250 nm (for balanced cross-correlator) and reflects 1120 nm (for balanced homodyne detector). For an intensity balancing, a variable attenuator is used in one of the arms. Figure 2-23 shows the intensity noise cancellation by intensity balancing. The RIN from Cr:forsterite and Ti:sapphire lasers are cancelled down to the detector noise floor. This balancing is kept in a drift-free way. By use of this detector, an exceptionally high SNR of 60 dB is achieved to detect the Δf_{ceo} beatnote. For generation of this beat signal, $\sim$1 μW of 1120 nm power from each laser is used. Figure 2-24 shows the measured Δf_{ceo} at 1 MHz with a resolution bandwidth of 10 kHz.

2.7.2 Orthogonal Control Between Timing and Phase Synchronization

Because the balanced homodyne detector detects the Δf_{ceo} signal itself, one can directly lock this signal to DC by applying it to the acousto-optic modulator (AOM) in the pump beam. The intra-cavity energy change by the AOM induces the carrier-envelope offset frequency change by an amplitude-to-phase conversion in the laser cavity (Eq. A.12).

However, there are two major problems in this attempt. First, when it is locked, the peak-to-peak residual phase jitter should be kept within π optical phase, that is, 1.87 fs at 1120 nm. Otherwise, the phase lock will be broken by the limited locking range of the homodyne detector. Second, the intra-cavity energy change induces not only the carrier-envelope offset frequency change but also the repetition rate change (Eq. A.14). Although the impact is quite small for the fundamental repetition rate (f_{rep}), at the optical frequency (mf_{rep} with $m \simeq 268\text{THz}/82\text{MHz} = 3.3 \times 10^6$), the impact is multiplied by a factor of millions. This is because what the homodyne detector measures is the difference in the comb line positions between two lasers at 268 THz. As a result, the residual timing jitter influenced by the pump power

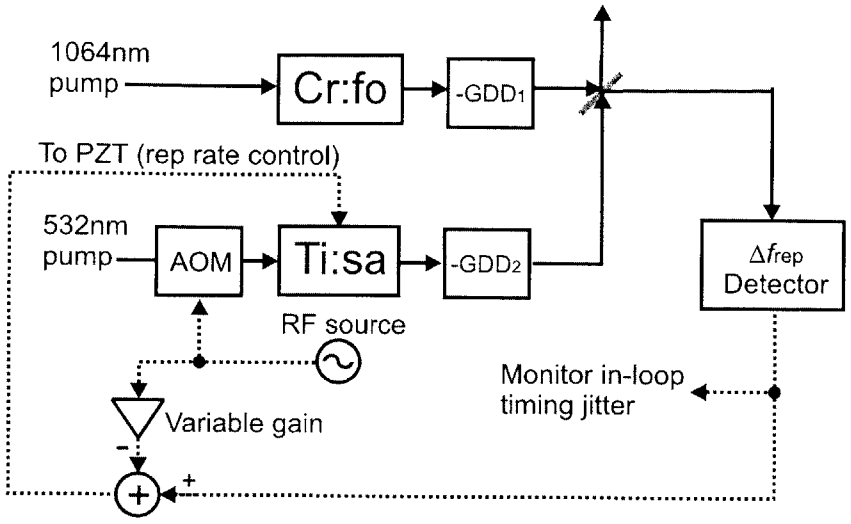

Figure 2-25: Test of orthogonal control between timing and phase locking loops.

modulation in turn affects the carrier-envelope phase locking loop. Even in the case when the residual phase jitter is well below π optical phase, if the 'cross-talk' from the timing locking loop is more than the pull-in range of the phase lock (1.87 fs in this case), the lock cannot be acquired.

In this section, a scheme for orthogonal control between timing and phase lock is tested. It is implemented by subtracting the AOM driving signal from the PZT driving signal so that the impact from the intra-cavity energy change is minimized in the timing locking loop. It is similar idea with the orthogonal controller between diode injection current and saturable absorber bias voltage shown in Ref. [81]. Figure 2-25 shows the schematic of the orthogonal control test. The AOM placed in the pump beam of the Ti:sapphire laser is modulated by 20 kHz signal from an RF source. Note that frequency modulation below 1 kHz does not affect the timing lock because of enough loop gain provided by the in-loop integrator. Frequency components above hundreds kHz also do not impact the system much because the laser response has a limited bandwidth set by the relaxation oscillation.

The results are summarized in Fig. 2-26. When the orthogonal control is off, 2 $\%_{pp}$ change of pump power induces 8 fs_{pp} timing jitter by the amplitude-to-timing conversion in the laser cavity. Then the gain is increased until the 20 kHz peak is

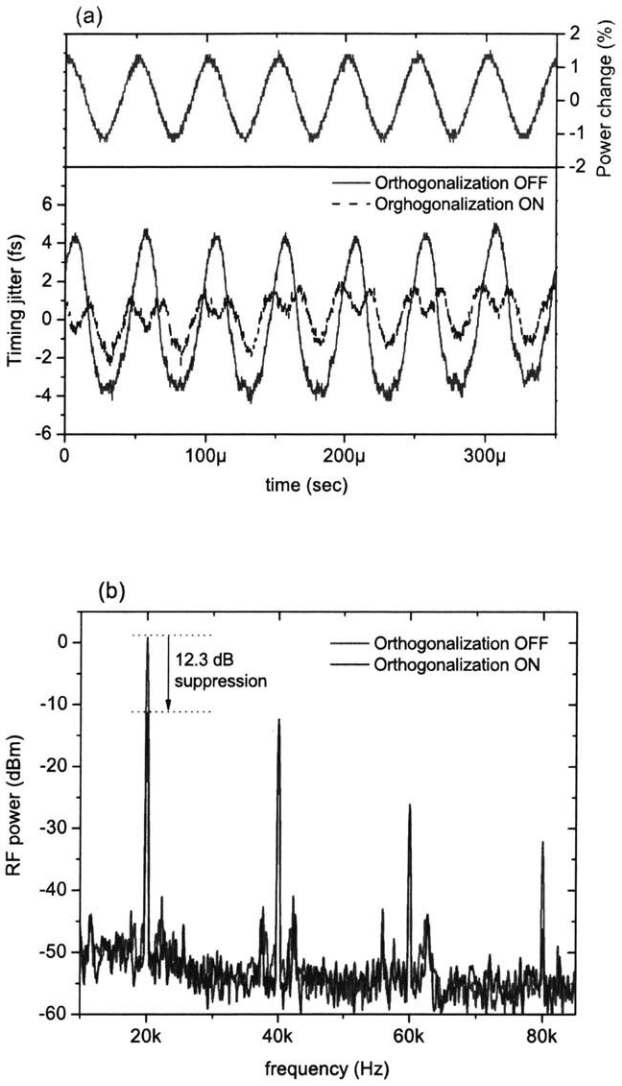

Figure 2-26: Crosstalk suppression by orthogonal control. The AOM is modulated by a 20 kHz RF signal. (a) Without orthogonal control, 2 $\%_{pp}$ power modulation induces 8 fs_{pp} timing jitter. With orthogonal control, it is suppressed to 3 fs_{pp} jitter. (b) In the frequency domain, the 20 kHz peak is suppressed by 12.3 dB with the orthogonal control.

minimized. In this way, 12.3 dB could be suppressed. This is shown in Fig. 2-26 (b). In the time domain, it is compared with the case when the orthogonal control is off in Fig. 2-26 (a). The peak-to-peak jitter is decreased to 3 fs_{pp}. The imperfect suppression is caused by (a) the phase shift between the AOM driving signal and the timing error signal that drives the PZT and (b) the nonideal PZT responses. An additional phase shifter might be able to correct the problem. It requires more investigation on the frequency dependence of phase shift.

To acquire the carrier-envelope offset frequency lock, the pump power typically needs to be modulated by about ± 1 $\%_{pp}$. It means that without orthogonal control, more than 8 fs_{pp} timing jitter fluctuation can be induced in the timing lock. This in turn fluctuates the heterodyne beat signal and hinders the carrier-envelope phase locking process. With the current orthogonal control, reduction of cross-talk down to 3 fs_{pp} jitter is feasible. With more optimized orthogonal control, less than 1 fs_{pp} transient jitter level is envisioned.

2.7.3 Experiments and Measurement Results

Figure 2-27 shows the schematic of the entire experimental setup for the timing and phase synchronization. Major components and techniques in this setup are presented in the previous sections: broadband prismless Ti:sapphire and Cr:forsterite lasers in Sec. 2.3; noise eater in Sec. 2.4; broadband 50:50 beam splitter with matched GDD for pulse combining in Sec. 2.5; balanced optical cross-correlator for timing synchronization in Sec. 2.6; balanced homodyne detector and orthogonal controller for phase synchronization in Sec. 2.7. For the robust operation, the entire setup is built on a single breadboard. The setup is protected from air currents by an enclosure made of 0.5" thick polycarbonate plates. Further, the breadboard is placed on multiple layers of lead foil and polyester-based polyurethane foam to isolate the system from the acoustic vibrations from the optical table.

The detected Δf_{ceo} signal is locked to 3 MHz from an RF source by a digital phase detector. The reasons for locking the beatnote in this way are two-fold. First, the digital phase detector provides a much extended locking range of $[-32\pi,+32\pi]$. This

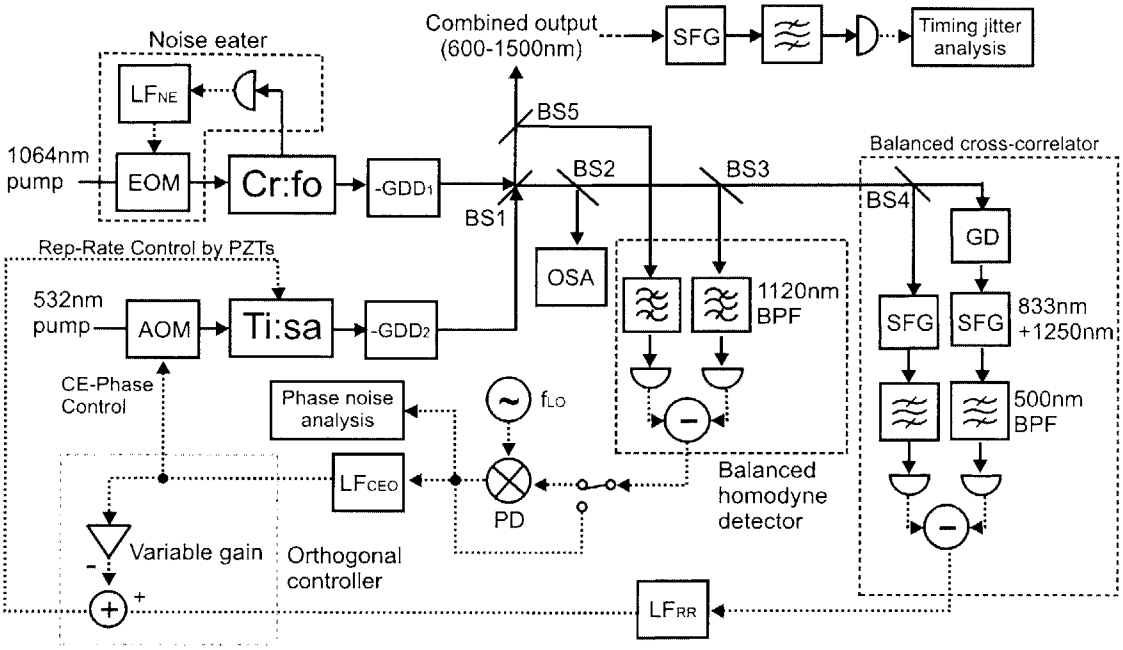

Figure 2-27: Schematic outline of the entire timing and phase synchronization setup. AOM, acousto-optic modulator; BPF, bandpass filter; BS1 and BS4, broadband 50:50 beam splitter with matched GDD (described in Sec. 2.5); BS2 and BS5, 10% tapping beam splitter; BS3, dichroic beamsplitter (transmits 833 nm and 1250 nm; reflects 1120 nm); Cr:fo, Cr:forsterite laser oscillator; EOM, electro-optic modulator (implemented as a combination of quarter-wave plate, Pockels cell and polarizer); f_{LO}, RF synthesizer; GD, group delay element (3-mm thick fused silica); $-GDD_1$, extra-cavity dispersion precompensation for Cr:forsterite laser output; $-GDD_2$, extra-cavity dispersion precompensation for Ti:sapphire laser output; LF_{CEO}, loop filter for the f_{ceo} locking loop; LF_{NE}, loop filter for noise eater; LF_{RR}, loop filter for repetition rate locking loop; OSA, optical spectrum analyzer; PD, digital phase detector; SFG, sum-frequency generation crystal (LBO); Ti:sa, Ti:sapphire laser oscillator.

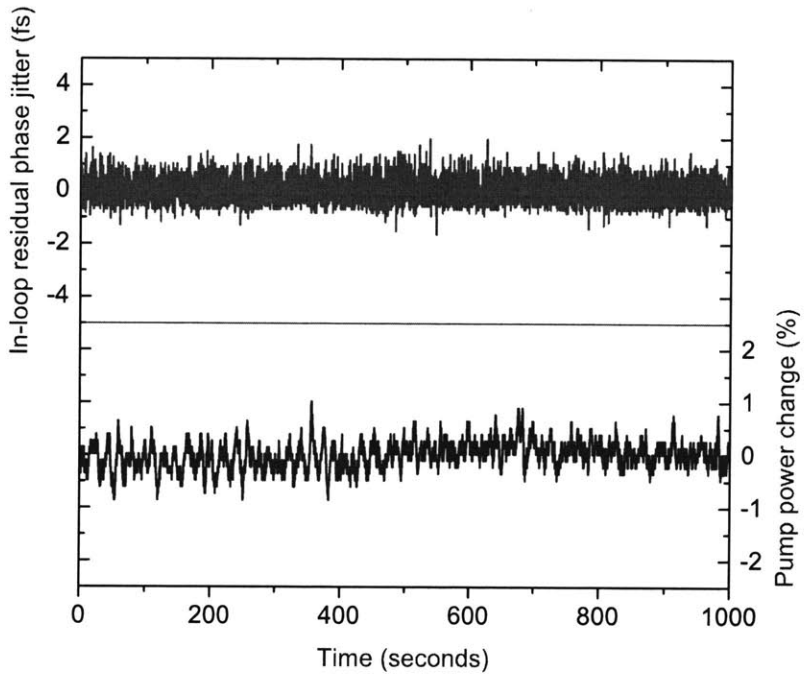

Figure 2-28: In-loop residual carrier-envelope offset phase jitter and the corresponding pump power change over 1000 seconds when Δf_{ceo} is locked to 3 MHz. The residual rms phase jitter is 476 as (0.26π rad at 1120 nm wavelength).

feature makes lock acquisition much easier especially in the transient state when the modulated pump power influences both timing and phase loops. Second, when the beatnote is locked, it provides useful information of how much residual phase noise exists in the heterodyne beatnote itself. With the digital phase detector, a long-term stable (>1 hour) carrier-envelope offset phase lock is obtained.

Figure 2-28 shows the in-loop residual carrier-envelope offset phase jitter and the corresponding pump power modulation over 1000 seconds. The Δf_{ceo} is locked to 3 MHz. The residual rms phase jitter is 0.26π rad at 1120 nm wavelength. This corresponds to 476 as phase jitter. This confirms that long-term stable subfemtosecond timing and phase synchronization is feasible between two independently mode-locked lasers. To the best of my knowledge, this is the first time to demonstrate continuously phase-coherent optical spectrum over 1.5 octaves with subfemtosecond-precision timing and phase jitters between two independently mode-locked lasers.

2.8 Summary and Future Work

In summary, a phase-coherent ultrabroadband optical spectrum ranging from the visible to the infrared is demonstrated by subfemtosecond timing and phase synchronization of mode-locked Ti:sapphire and Cr:forsterite lasers.

The next step is clear – locking the Δf_{ceo} to DC. For that, a hybrid phase-lock technique using an offset locking [45, 83] and balanced homodyne detection is currently pursued. The idea is first locking the Δf_{ceo} to DC by an offset locking that can provide large phase detection range with digital phase detectors. Because the offset locking performance is limited by the uncontrolled path difference between the two laser outputs, the slow drift will be detected and compensated by the balanced homodyne detection presented in Sec. 2.7. In this way, one can attain long-term drift-free phase synchronization over an extended phase locking range. In addition, improvements of the noise eater by RTP or BBO crystal-based Pockels cell as well as phase adjustment of orthogonal control will further reduce the residual noise. With all these improvements, it is expected to reduce the residual timing and phase jitter

below the 100 as regime.

When the locking of Δf_{ceo} to DC is done, it will be necessary to characterize the synthesized optical pulses. For this pulse characterization, conventional interferometric autocorrelation is not suitable because the second harmonic components will have a strong spectral overlap with the fundamental. Pulse characterization techniques that directly measure spectral phase using broadband upconversion processes will be more suitable, for example, a recently developed two-dimensional spectral shearing interferometry (2DSI) [82]. Once it is confirmed that the pulses are indeed approaching single-cycle duration, one can use the synthesized pulses for various phase-sensitive nonlinear optics experiments.

While keeping the demonstrated timing and phase synchronization techniques, other interesting pulse synthesis experiments can be designed by replacing the current laser sources. Note that most of the current limitations are originated from low average output power and high residual noise of the used lasers. In fact, very recently, there has been remarkable progress in the high repetition rate and low noise Ti:sapphire lasers and Er-fiber lasers. In the future, it will be more advantageous to replace Cr:forsterite laser with a spectrally-broadened Er-fiber laser for lower noise, broader spectrum, and more stable operation. In this way, we can envision to generate spectrum from 550 nm to 2 μm range that might be able to generate a pulse even shorter than one cycle of light oscillation.

Coherent superposition of multiple lasers is not only useful for synthesizing shorter pulses. It can also generate higher energy pulses by combining multiple lasers in the same spectral range. For this power scaling applications, a single-crystal balanced cross correlator demonstrated in Chapter 4 can be used for subfemtosecond timing synchronization.

Chapter 3

Long-Term Stable Microwave Signal Synthesis from Mode-Locked Lasers

3.1 Motivation

Mode-locked lasers show a great potential to generate ultralow-jitter microwave and RF signals encoded in its pulse repetition rate [10, 22, 84, 85]. However, it is a highly nontrivial task to transfer the low noise properties of the pulse train in the optical domain to the electronic domain, and extract a drift-free, ultralow-jitter microwave signal with a power level sufficient for the intended application from an optical pulse train. For distribution and synchronization of microwave signals from optical pulse trains in large-scale, high-precision timing distribution systems [20, 86, 87], it is crucial to convert the optical pulse train into a drift-free, low-jitter microwave signal with a satisfactory power level in a long-term stable way. Readout of microwave signals from atomic optical clocks [88, 89] is another important motivation for long-term drift-free extraction of microwave signals from optical pulse trains. We can also envision to implement ultralow-noise RF and microwave signal synthesizers based on mode-locked lasers both at the commercial instruments level and at the electronic-photonic

integrated circuits level.

The extraction of a microwave signal from an optical pulse train using direct photodetection, the most commonly used technique for microwave signal extraction from pulse trains, suffers from excess phase noise [24, 90, 91]. The major origin of this excess noise is amplitude-to-phase conversion in the photodetectors and microwave mixers [90, 92]. The intensity noise and power drifts of optical pulse trains can be converted into a significant amount of excess timing jitter and drifts, and degrade the long-term stability of the extracted microwave signals. In Refs. [26] and [88], the amplitude-to-phase conversion factor of high-speed photodiodes was measured, and it typically ranged from 1 to 10 ps/mW, depending on the bias voltage and diode type used. For a 12-GHz commercial InGaAs photodetector at 6 V reverse bias, the amplitude-to-phase conversion factor was measured as 1.6 ps/mW [26]. For an Er-doped fiber laser with 0.03 $\%_{\mathrm{rms}}$ relative intensity noise (RIN), this may already result in 5-fs excess jitter when 10 mW of power is applied to the photodetector. In addition, direct photodetection has a limited extractable microwave power and signal-to-noise ratio (SNR) due to the limited input optical power to the photodetector. Phase drifts in the diode due to temperature change (>300 fs/K is reported in Ref. [25]) as well as post-amplification to reach the required signal level can prevent long-term stable regeneration of microwave signals.

Nevertheless, careful suppression of these excess noise sources has been used to demonstrate microwave signal extraction from optical pulse trains at 10 GHz with 3.3 fs timing jitter measured from 0.1 Hz to 1 MHz [88] and later even 0.8 fs measured from 1 Hz to 1 MHz at a power level of -15 dBm [89]. Although the short-term jitter could be suppressed down to 1 fs level, the slow phase drift of extracted microwave signals is still the major limitation, for example, ~56 fs (~3.5 mrad at 10 GHz) drift in 100 seconds caused by ~0.3 % amplitude fluctuation as shown in Ref. [88]. For precise timing synchronization applications, this drift sets a serious limitation.

To circumvent the amplitude-to-phase conversion and to ensure long-term stable microwave signal extraction directly at the microwave power level needed for subsequent experiments, it is highly desirable to develop an optoelectronic phase-locked

loop (PLL) using an optical pulse train and a high-quality voltage-controlled oscillator (VCO) to prevent those undesired amplitude-to-phase conversion and drifts from the photodetection process. In doing so, the key issue is the development of drift-free, low-jitter phase detectors that extract the timing error between optical pulse trains and microwave signals in the optical domain. By closing the PLL using the detected timing information, the relative phase between optical pulse trains and microwave signals can be fixed in the optical domain before the photodetection is involved. In this way, one can avoid the timing/phase drift of photodetection and post-amplification stages that limits the quality of extracted microwave signals. In this Chapter, two new optoelectronic PLL techniques for low-noise and drift-free microwave signal synthesis are presented. For both techniques, an electro-optic sampling by a Sagnac-loop interferometer is used to detect the phase error between optical pulse trains and microwave signals. The first technique converts the phase error into an intensity imbalance and uses this information to close the loop (presented in Section 3.2). The second one converts the phase error into an intensity modulation depth and detect it by downconversion with a synchronous detection (presented in Section 3.3).

3.2 Microwave Signal Synthesis from Mode-Locked Lasers Using Balanced Intensity Detectors

3.2.1 Operation and Noise Analysis

The general idea for transfer of timing information into the optical domain is visualized in Figure 3-1. While still in the optical domain, the timing information is transferred into an intensity imbalance between two beams by sending the pulse train through a pair of amplitude modulators. The modulators are driven by the output signal from a VCO with 180° phase difference. The intensity difference, which is proportional to the timing error between the positions of microwave signal zero-crossings and the optical pulse trains, is detected by a balanced detector. This signal controls the input to the VCO and changes the driving frequency of the modulators until the

pulse train coincides with the zero-crossings of the driving microwave signal, leading to the balanced output powers. This closes the PLL operation. With this scheme, the problem of photodetection on the electronic side is shifted to the optical side. The method derives a signal that carries the timing information not susceptible to the amplitude-to-phase conversion in the photodetection.

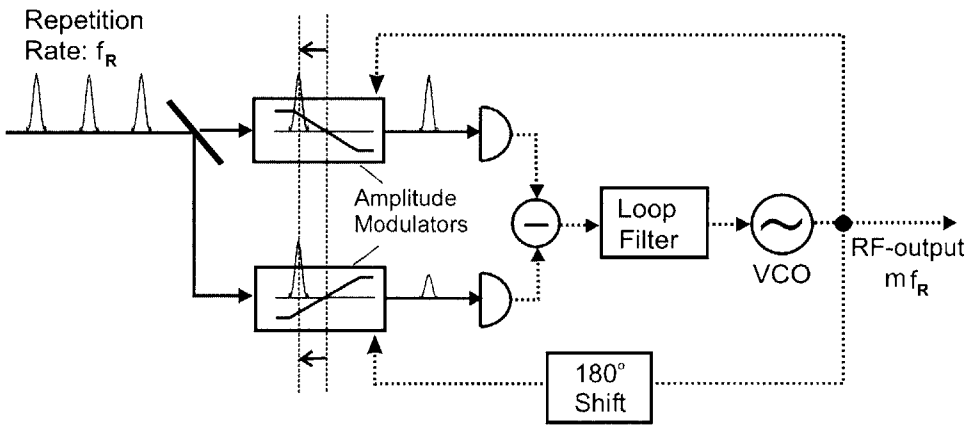

Figure 3-1: Schematic setup for microwave signal extraction from an optical pulse train by transferring timing information into the optical domain.

The 180° out-of-phase amplitude modulators can be realized by a Mach-Zehnder interferometer with a phase modulator in one arm. However, this scheme will suffer from the phase drifts in the interferometer arms due to temperature fluctuations, air currents, and mirror vibrations. To remove these problems, the interferometer can be implemented in a Sagnac-loop configuration. The two outputs from the Sagnac-loop are expressed as $P_1 = P_{in}\sin^2(\Delta\phi/2)$ and $P_2 = P_{in}\cos^2(\Delta\phi/2)$, where P_{in} is the average input power and $\Delta\phi$ is the phase difference between counter-propagating pulses in the loop. The outputs are intensity-balanced when the phase difference $\Delta\phi$ is set to $\pi/2$.

In the following, the phase detection sensitivity and the shot noise limited performance of this scheme will be derived. The optical pulse train applied to the Sagnac

loop can be written as

$$P_{in}(t) = P_{avg,in} T_R \sum_{n=-\infty}^{\infty} \delta(t - nT_R), \tag{3.1}$$

where $P_{avg,in}$ is the average optical power of the input pulse train to the Sagnac-loop and $T_R = 1/f_R$ is the period of the pulse train.

The phase modulation driven by the microwave signal from VCO is

$$\Delta\phi(t) = \Phi_0 \sin(2\pi f_0 t + \theta_e) + \Phi_{DC}, \tag{3.2}$$

where Φ_0 is the phase modulation amplitude by the VCO output, f_0 is the frequency of the VCO output, θ_e is the phase error between input pulse train and the VCO output, and Φ_{DC} is the DC phase offset between counter-propagating pulses. Ideally this value should be $\pi/2$ to enable locking at the zero-crossings.

After circulating in the Sagnac-loop, the optical power detected at each photodiode of balanced detector is expressed as

$$P_1(t) = P_{in}(t) \sin^2\left(\frac{\Delta\phi(t)}{2}\right) = P_{avg} T_R \sum_{n=0}^{\infty} \sin^2\left[\frac{1}{2}\{\Phi_0 \sin(2\pi f_0 t + \theta_e) + \Phi_{DC}\}\right] \delta(t - nT_R), \tag{3.3}$$

$$P_2(t) = P_{in}(t) \cos^2\left(\frac{\Delta\phi(t)}{2}\right) = P_{avg} T_R \sum_{n=0}^{\infty} \cos^2\left[\frac{1}{2}\{\Phi_0 \sin(2\pi f_0 t + \theta_e) + \Phi_{DC}\}\right] \delta(t - nT_R). \tag{3.4}$$

Now suppose the frequency is locked, that is, $f_0 = N f_R$. The averaged photocurrent generated from each photodiode is

$$\langle I_1 \rangle = R P_{avg} \sin^2\left[\frac{1}{2}\{\Phi_0 \sin\theta_e + \Phi_{DC}\}\right], \tag{3.5}$$

$$\langle I_2 \rangle = R P_{avg} \cos^2\left[\frac{1}{2}\{\Phi_0 \sin\theta_e + \Phi_{DC}\}\right], \tag{3.6}$$

where R is the responsivity of photodiode in A/W unit.

The output of balanced detector is

$$\langle I_d \rangle = \langle I_2 \rangle - \langle I_1 \rangle = RP_{avg} \cos[\Phi_0 \sin\theta_e + \Phi_{DC}]. \tag{3.7}$$

Supposing the ideal DC phase offset, $\Phi_{DC} = \pi/2$, the output of the balanced detector in the linear regime ($\theta_e << 1$) is

$$\langle I_d \rangle = RP_{avg} \sin[\Phi_0 \sin\theta_e] = RP_{avg}\Phi_0\theta_e. \tag{3.8}$$

Therefore, the phase detection sensitivity in A/rad is $K_d = \langle I_d \rangle/\theta_e = RP_{avg}\Phi_0$.

There are several amplitude noise sources inside the PLL. For example, the shot noise at photodiodes, the thermal noise from resistors, and the acoustic noise introduced to the interferometer. The in-loop amplitude noise is converted to the phase noise at the VCO output over the PLL bandwidth. The fundamental limit comes from the shot noise, and here the shot noise limited phase noise level is derived.

The shot noise current density in A^2/Hz is

$$\Phi_{I_{\text{Shot}}} = 2qI_0 = 2q\left(\frac{RP_{avg}}{2}\right) = qRP_{avg}. \tag{3.9}$$

With balanced detector, the shot noise from each photodiode is added.

$$\Phi_{I_{\text{Shot}}}^{\text{balanced}} = 2\Phi_{I_{\text{Shot}}} = 2qRP_{avg}. \tag{3.10}$$

From Eqs. 3.8 and 3.10, the resulting single-sideband (SSB) output phase noise density within the PLL bandwidth (in rad^2/Hz) is

$$S_{\varphi,I_{Shot}} = \frac{1}{2} \cdot \frac{\Phi_{I_{\text{Shot}}}^{\text{balanced}}}{K_d^2} = \frac{2qRP_{avg}}{2R^2P_{avg}^2\Phi_0^2} = \frac{q}{RP_{avg}\Phi_0^2}. \tag{3.11}$$

This relationship indicates that the residual phase noise is scalable by increasing the input optical power (P_{avg}) as well as the driving microwave power from the VCO (Φ_0). This noise scalability is much more difficult to be implemented by direct photodetection scheme.

3.2.2 Experimental Setup

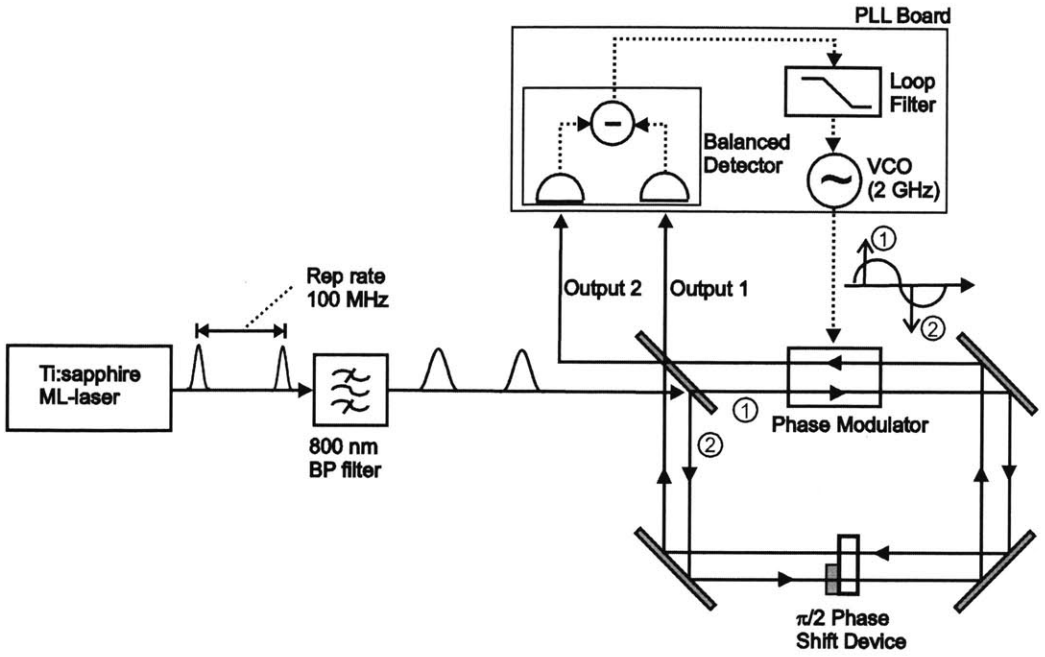

Figure 3-2: The scheme for extraction of a 2 GHz signal from a 100 MHz repetition rate Ti:sapphire laser [94].

Figure 3-2 shows the synchronization scheme. A 100 MHz repetition rate Ti:sapphire mode-locked laser is used as the pulse source. After passing a bandpass filter at 800 nm to limit the pulsewidth to about 100 fs, the input optical pulse train is sent into the Sagnac-loop. A resonant phase modulator at 2 GHz is positioned in the Sagnac-loop in such a way that the optical delay between counter propagating pulses at the phase modulator is set to half of the microwave signal period, i.e., 0.5 ns for the 2 GHz VCO. This assures that the two pulses experience opposite phase modulation. The output beams are detected by a balanced detector that generates a difference signal between the two photocurrents from the two Si pin-photodiodes. The output current from the balanced detector is transferred to a passive loop filter (type II, order 2 topology [93]) for proper filtering. The passive loop filter structure is advantageous over an active counterpart since it allows a simple circuit implementation and also ensures excellent noise performance. The loop filter output signal drives the VCO and changes the driving frequency of the phase modulator until it reaches a phase-

locked state by balancing the two output powers from the interferometer. This closes the PLL operation. For a stable and drift-free biasing of the interferometer (setting $\Phi_{DC} = \pi/2$ in Eq. 3.2), an effective quarter-wave plate is inserted in one of the beams using a thin-film coating covering only half of the substrate. A very stable and drift free phase-locked operation is achieved with this scheme.

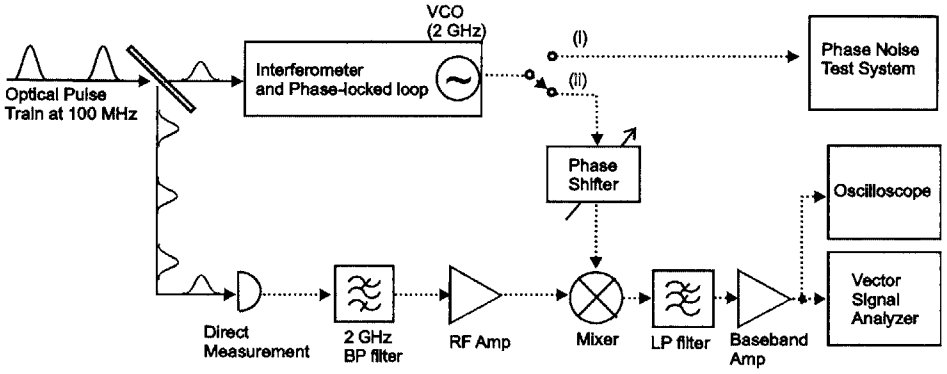

Figure 3-3: The VCO output is characterized (i) by a commercial phase noise test system and (ii) by mixing in quadrature with the 2 GHz component of the directly detected signal. The resulting signal is measured with a vector signal analyzer. The normalization constant for calibration to the microwave phase is measured independently with an oscilloscope.

The phase noise of the microwave output signal from the VCO is characterized in two ways: (i) by the frequency discriminator technique using a commercial phase noise measurement setup PN9000 from Aeroflex; (ii) by mixing the output signal of the VCO in quadrature with the 2 GHz component of the directly detected pulse train in order to measure the relative phase noise between the optical pulse train and the extracted microwave signal. Figure 3-3 shows the measurement set-up. Using method (i), the input is delayed and mixed with itself in quadrature in order to extract the phase noise of the input. Method (ii) is a standard technique to measure the residual phase noise between two locked microwave signals where an oscilloscope is used to monitor that the two microwave signals are in quadrature, and a vector signal analyzer is used to measure the noise spectrum.

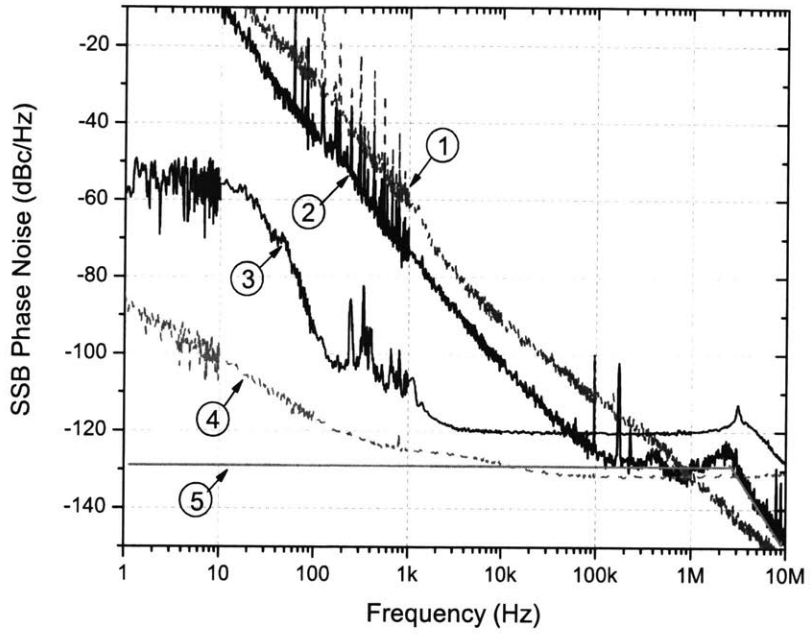

Figure 3-4: Measured single-sideband phase noise of (1) the free-running VCO and (2) the locked VCO using a commercial phase noise measurement system. Curve (3) shows the measured single-sideband phase noise between extracted microwave signal and the 20th harmonic of directly detected pulse train using a mixer and vector signal analyzer. Curve (4) shows the noise floor of the vector signal analyzer. Curve (5) shows the estimated phase noise level of extracted microwave signal from result of curve (2).

3.2.3 Measurement Results and Discussions

The measured single-sideband (SSB) phase noise spectra from 1 Hz to 10 MHz are shown in Figure 3-4. Curve (1) shows the phase noise spectrum of the free-running VCO measured with the Aeroflex phase noise measurement system. Curve (2) shows the phase noise measured by the same method when the system is locked. The locking is clearly visible in the spectrum covering the range of 100 kHz to 10 MHz. At lower frequencies, the phase noise of the Ti:sapphire pulse train dominates. The phase noise level of the free-running Ti:sapphire laser is +26 dB up-shifted due to the frequency ratio of 20 between repetition rate and VCO frequency.

To verify the assumption that the phase noise of the laser dominates at low frequencies in the frequency discriminator measurement results, the relative phase noise between the pulse train and the microwave signal was measured by using the second phase noise characterization method. The result is shown in curve (3) of Fig. 3-4. Due to the noise floor of the vector signal analyzer (curve (4) in Fig. 3-4) and excess noise in the photo-detector that generates the reference signal, the high frequency noise floor is increased in comparison to method (i). But this measurement clearly shows that the noise increase at low frequency in curve (2) is the phase noise of the free-running Ti:sapphire laser.

The origin of the enhanced phase fluctuations below 1 kHz may be due to either mechanical vibrations in the Sagnac-loop or excess phase noise in the photo-detection process that converts enhanced laser amplitude fluctuations into phase fluctuations. In any case, based on the current measurements, the relative timing jitter between the microwave signal and the pulse train integrated from 1 kHz to 10 MHz can be estimated by the area underneath curve (5), which lines up with the high frequency noise of the Aeroflex measurement (curve (2) in Fig. 3-4) and results in about 60 fs timing jitter.

Now we will check whether the measured phase noise level agrees with the theoretical shot noise limited performance (Eq. 3.11). The phase modulation amplitude Φ_0 is determined by $\Phi_0 = \pi V_{VCO}/V_\pi = 0.07$ rad, where the VCO output amplitude is $V_{VCO} = 0.71$ V and the half-wave voltage of phase modulator is $V_\pi = 31.4$ V. With other parameters used in the experiment, photodiode responsivity $R = 0.5$ A/W and $P_{avg} = 1$ mW, the shot noise limited SSB phase noise level is

$$S_{\varphi,I_{Shot}} = \frac{q}{RP_{avg}\Phi_0^2} = 6.5 \times 10^{-14} \text{ rad}^2/\text{Hz} = -132 \text{ dBc/Hz} \qquad (3.12)$$

This result fairly agrees with the measurement, Curve (5) of Fig. 3-4, from 1 kHz to the loop bandwidth ($\sim$ 1 MHz). The integrated jitter based on this calculation from 1 Hz to 10 MHz results in 56 fs. It confirms that we are mostly limited by shot noise of photodetection.

For long-term stability (below 1 kHz), a fiber implementation of the Sagnac-loop is preferable. This will eliminate a large part of drift problems from any thermal drifts of the output beam-splitter that lead to an imbalance of the interference and a drift in phase. In addition, the use of a VCO with better phase noise performance will greatly reduce the high frequency noise contribution. However, the major limitation is coming from the limited optical power applicable to the photodiodes. Because the balancing is achieved when both photodiodes receive half of the input optical power ($P_{avg}/2$), one cannot arbitrarily increase the input optical power. To address these issues, a balanced optical-microwave phase detector is proposed and demonstrated in the next section.

3.3 Microwave Signal Synthesis from Mode-Locked Lasers Using Balanced Optical-Microwave Phase Detectors

Although the synchronization of microwave signals with optical pulse trains based on balanced intensity detection provides a very simple interface between optics and electronics domains, it is difficult to scale the noise performance due to the limited optical power applicable to the photodiode and the drift in beam combining and splitting. To overcome these problems, a device named balanced optical-microwave phase detector is proposed and demonstrated in this section. This phase detector is still based on the timing information transfer into the optical domain. However, it is implemented by use of a differentially-biased Sagnac fiber-loop and synchronous detection, which is similar to Sagnac-loop based gyroscopes [95] and clock recovery systems [96].

3.3.1 Operation and Noise Analysis

In this section, the operation and noise analysis of balanced optical-microwave phase detectors are presented. Figure 3-5 (a) shows the schematic diagram of the optoelec-

tronic PLL using a balanced optical-microwave phase detector. Figure 3-5 (b) shows the relative phase relationship between the optical pulse train, the voltage-controlled oscillator (VCO) output signal, and the reference signal. Major parameters used in the derivation in this section are labelled in Fig. 3-5 (a) and (b).

The optical pulse train applied to the Sagnac-loop can be written as

$$P_{in}(t) = P_{avg,in} T_R \sum_{n=-\infty}^{\infty} \delta(t - nT_R), \tag{3.13}$$

where $P_{avg,in}$ is the average optical power of the input pulse train to the Sagnac-loop and $T_R = 1/f_R$ is the period of the pulse train.

The phase modulator in the Sagnac-loop is driven by the sum of the signal from (1) the VCO with a frequency equal to a multiple of repetition rate, $f_0 = N f_R$ (when locked), and (2) the reference signal with a frequency of half the repetition rate, $f_r = f_R/2$ (where $f_R = 1/T_R$ is the repetition rate of the pulse train):

$$\phi(t) = \Phi_0 \sin(2\pi f_0 t + \theta_e) + \Phi_m \sin(\pi f_R t + \Delta\phi), \tag{3.14}$$

where Φ_0 is the amplitude of phase modulation from the VCO, θ_e is the phase error between the pulse train and the VCO signal, Φ_m is the amplitude of phase modulation from the reference signal, and $\Delta\phi$ is the fixed relative phase between the pulse train and the reference signal.

After circulating in the Sagnac-loop interferometer, the optical power detected at the photodiode ($P(t) = (1-L)P_{in}(t)\sin^2(\varphi/2)$, where L is the loss in the Sagnac-loop and φ is the phase difference between counterpropagating pulses in the Sagnac-loop) is expanded as

$$P(t) = P_{avg} T_R \sum_{n=-\infty}^{\infty} \sin^2\left[\frac{1}{2}\Phi_0 \sin(2\pi f_0 t + \theta_e) + \Phi_m \sin(\pi f_R t + \Delta\phi)\right] \delta(t - nT_R), \tag{3.15}$$

where $P_{avg} = (1 - L)P_{avg,in}$ is the average power of the output pulse train from the Sagnac-loop.

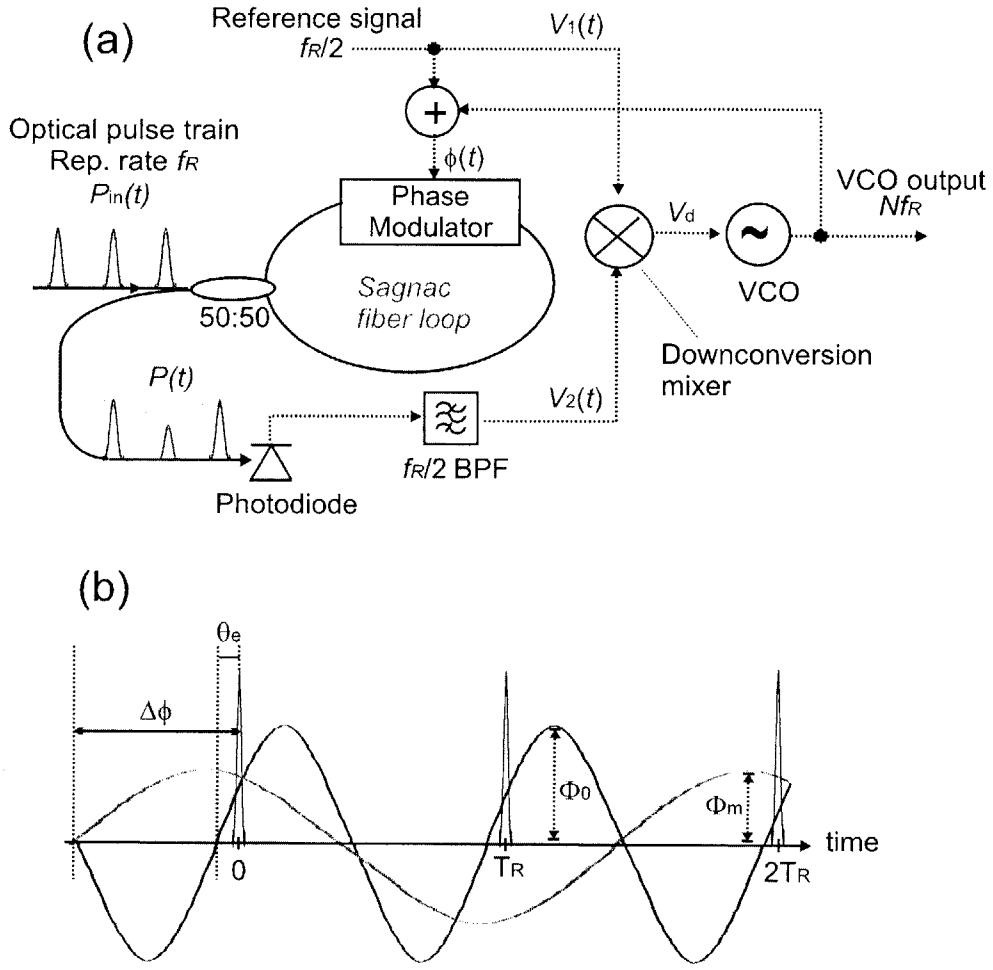

Figure 3-5: (a) Schematic diagram of the optoelectronic phase-locked loop (PLL) using a balanced optical-microwave phase detector. BPF, bandpass filter; VCO, voltage-controlled oscillator. (b) Relative positions of the optical pulse train (blue pulse train), the VCO output signal (red sinusoidal signal), and the reference signal (grey sinusoidal signal). For illustrative simplicity, N is set to $N = 1$.

The high frequency VCO signal (10.225 GHz in this work) has a unidirectional phase modulation by the travelling-wave nature of the phase modulator. Because the same unidirectional property is not applied to the reference signal (22.13 MHz in this work), the phase modulator is positioned in such a way that counterpropagating pulses experience opposite phases by the reference signal. This is the reason why the modulation depth is multiplied by a factor of two only for the reference signal in Eq. 3.15.

Now suppose the frequency is locked, that is, $f_0 = Nf_R$. Since the pulse train will sit on the zero-biasing points, i.e., $t_n = nT_R$ at the locked state, the following approximations are valid: $\sin(2\pi f_0 t+\theta_e) = \sin(2\pi Nn+\theta_e) \simeq \theta_e$ and $\sin(\pi f_R t+\Delta\phi) = \sin(n\pi+\Delta\phi)$. In addition, $\sin^2(\varphi/2) \simeq \varphi^2/4$ holds for small phase modulations. With these linear approximations, the optical power at the photodiode (Eq. 3.15) is then expressed as

$$P(t) = P_{avg}T_R \sum_{n=-\infty}^{\infty} \left[\left\{ \frac{\Phi_0^2\theta_e^2}{4} + \frac{\Phi_m^2}{2}\left(1-\cos(2\Delta\phi)\right) \right\} + \Phi_0\Phi_m\theta_e \sin\left(\pi f_R t + \Delta\phi\right) \right] \delta(t-nT_R). \tag{3.16}$$

By the Fourier transform of Eq. 3.16, one can extract the amplitude at the reference frequency, $f_R/2$. The result is the following:

$$P\left(\pm j\frac{f_R}{2}\right) = 2\pi P_{avg}\Phi_0\Phi_m \sin(\Delta\phi)\theta_e\delta\left(f \mp \frac{f_R}{2}\right). \tag{3.17}$$

We clearly see the relative phase $\Delta\phi$ should be set to $\pi/2$ to maximize the phase detection sensitivity. In this condition, the pulse train sits exactly on the maxima/minima of the modulation signal as shown in Fig. 3-5 (a). When the pulse train is received by a photodiode with a responsivity of R (A/W), bandpass-filtered at $f_R/2$, and amplified by a transimpedance gain of G (V/A), the input voltage to the downconversion mixer is

$$V_2(t) = 2RGP_{avg}\Phi_0\Phi_m\theta_e \cos\left(\pi f_R t\right). \tag{3.18}$$

Note that the phase error θ_e is encoded in the amplitude of the signal. To convert the phase error signal to the baseband, $V_2(t)$ is mixed with the reference signal $V_1(t)$:

$$V_1(t) = V_1 \sin(\pi f_R t + \Delta\phi) = V_1 \cos(\pi f_R t). \tag{3.19}$$

When these two signals are mixed in phase, the baseband voltage is

$$V_d = \alpha V_1(t) V_2(t)|_{f<f_R/2} = [\alpha R G P_{avg} \Phi_0 \Phi_m V_1]\, \theta_e, \tag{3.20}$$

where α (V^{-1}) is the conversion efficiency of the downconversion mixer. This is the phase error signal output from the balanced optical-microwave phase detector. Therefore, the phase detection sensitivity K_d (V/rad) is

$$K_d = \frac{V_d}{\theta_e} = \alpha R G P_{avg} \Phi_0 \Phi_m V_1. \tag{3.21}$$

The fundamental noise limit of this phase detector comes from the shot noise of the photodetection process. This is a valid assumption because the relative-intensity noise (RIN) of passively mode-locked solid-state lasers has a bandwidth limited by the long upper-state lifetime [97], typically less than 1 MHz. At the reference signal ($f_R/2$= 22.13 MHz in this work) where the synchronous detection is operated, the laser source was confirmed to be shot noise limited.

Here, the phase noise floor from shot noise will be derived. When the system is locked, the average optical power received at the Sagnac-loop output photodiode is

$$\begin{aligned} \langle P_{locked} \rangle &= \left\langle P_{avg} T_R \sum_{n=-\infty}^{\infty} \Phi_m^2 \delta(t - nT_R) \right\rangle \\ &= \Phi_m^2 P_{avg}. \end{aligned} \tag{3.22}$$

The shot noise current power spectral density in A^2/Hz unit is

$$\left\langle \bar{i}_{shot}^2 \right\rangle = 2qI_0 = 2qR\Phi_m^2 P_{avg}, \tag{3.23}$$

where q (C) is the electron charge.

When we suppose the reference signal is noise-free, the voltage noise density from the mixer output at the baseband in V^2/Hz unit is

$$\begin{aligned}\left\langle \overline{V}^2_{d,shot} \right\rangle &= \frac{1}{2}\alpha^2 V_1^2 G^2 \left\langle \bar{i}^2_{shot} \right\rangle \\ &= \alpha^2 V_1^2 q R G^2 \Phi_m^2 P_{avg}. \end{aligned} \tag{3.24}$$

From Eqs. 3.21 and 3.24, the single-sideband (SSB) phase noise density floor due to shot noise in rad^2/Hz at the carrier frequency Nf_R (the frequency of the VCO output signal) is expressed as

$$S_{\varphi,shot} = \frac{1}{2} \cdot \frac{\left\langle \overline{V}^2_{d,shot} \right\rangle}{K_d^2} = \frac{\alpha^2 V_1^2 q R G^2 \Phi_m^2 P_{avg}}{2\left(\alpha R G P_{avg} \Phi_0 \Phi_m V_1\right)^2} = \frac{q}{2 R P_{avg} \Phi_0^2}. \tag{3.25}$$

This sets the absolute limit in achievable residual jitter. It has basically the same form as the balanced intensity detection scheme, Eq. 3.11, with additional factor of 1/2. From this relationship, it is clear that higher optical power (P_{avg}) as well as phase modulation depth (microwave power) from the VCO output (Φ_0) enables the minimum residual jitter.

3.3.2 Experimental Setup

Figure 3-6 shows the schematic of the balanced optical-microwave phase detector. Part of the input pulse train is tapped off by photodiode 1. This photodiode signal is used to generate a reference signal for a synchronous detection at half the repetition rate ($f_R/2$) of the optical pulse source. The reference signal is then applied to both the phase modulator and the down-conversion mixer. The rest of the input pulse train is sent to the Sagnac-loop with an in-loop phase modulator. When there is no phase modulation, the loop output should be zero if the coupling ratio is exactly 50:50. The pulse train is phase-modulated by the sum of (i) the signal from the microwave input port at frequency Nf_R (N is an integer) and (ii) the reference signal at frequency $f_R/2$. The high frequency (Nf_R) microwave signal gives a unidirectional

phase modulation because of the travelling-wave nature of the phase modulator. For the reference signal whose frequency does not support the unidirectional modulation, the phase modulator is positioned in such a way that counter-propagating pulses at the phase modulator experience opposite phases due to the reference signal. The phase shifter 1 is used to align the pulse train positions to the maxima/minima of the reference signal. By this phase modulation, the output pulse train from the Sagnac-loop is amplitude-modulated at the frequency of $f_R/2$ as conceptually shown in Figs. 3-5 (a) and 3-6. As shown in Eq. 3.18, the amplitude-modulation depth is proportional to the phase error. The pulse train detected at the fiber-loop output with photodiode 2 is band-pass filtered at $f_R/2$, mixed in phase with the reference signal (phase shifter 2 is used to keep two signals in phase), and down-converted to the baseband. This phase error output is filtered and controls the low-noise VCO to close the PLL. When the PLL is in the locked state, the Sagnac-loop output pulse train is unmodulated.

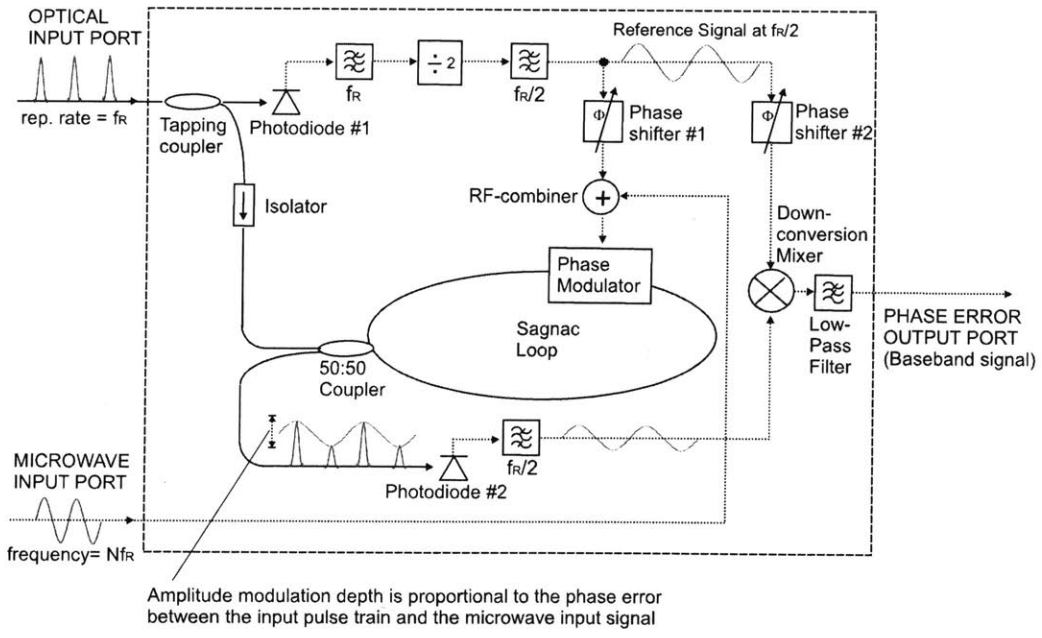

Figure 3-6: Schematic of the balanced optical-microwave phase detector [98]. The solid and dotted lines indicate optical and electrical signal paths respectively.

The major advantages of this phase detector are three-fold: (i) long-term drift-free operation, (ii) scalability in its phase detection sensitivity, and (iii) high-power microwave signal extraction. First, a long-term drift-free operation is possible by its "balanced" operation when it is locked. In the locked state, the broadband amplitude noise from both optical and microwave signals is suppressed by the synchronous detection. Since the detection does not use the phases of individual frequency components during photodetection, the amplitude-to-phase conversion does not affect the system performance. Another advantage, the scalability, comes from the fact that the phase detection sensitivity is proportional to the average optical power in the Sagnac loop and the modulation depth of the phase modulation as shown in Eq. 3.25. Finally, the use of high-power, low-noise VCOs leads to a better signal-to-noise ratio of the regenerated microwave signal, not limited by the extractable microwave signal power from photodetectors.

Figure 3-7 shows the experimental demonstration setup for the microwave signal extraction from an optical pulse train by use of the balanced optical-microwave phase detector. All optical components in the phase detector are implemented with commercial 1550-nm optical fibers and components. A stretched-pulse Er-doped fiber laser [99] (repetition rate $f_R = 44.26$ MHz) is used as the optical pulse source. Part of the input pulse train is tapped off by the pin-PD 1 to generate a synchronous detection reference signal at half the repetition rate ($f_R/2$) of the optical pulse source. In the experimental implementation, a signal with the frequency $10.5f_R$ is also generated to modulate the circulating pulse train in the fiber-loop. Frequency component $10.5f_R$ is used instead of $f_R/2$ to reduce the necessary fiber-loop length. The rest of the input pulse train ($P_{avg} = 5$ mW) is sent into the polarization-maintaining (PM) fiber Sagnac-loop including a phase modulator. The phase modulator is positioned in such a way that the optical delay between counter-propagating pulses at the phase modulator is set to $\Delta t_{delay} = 1/(2 \times 10.5f_R)$. The VCO (PSI DRO-10.225) has a center frequency of 10.225 GHz (Φ_0 =0.3 rad) which corresponds to the 231st harmonic of the fundamental repetition rate. The pulse train detected at the fiber-loop output (pin-PD 2) has an amplitude modulation with frequency $f_R/2$ whose amplitude is

proportional to the phase error between the pulse train and the VCO signal. This amplitude modulation is converted to the baseband by synchronous detection with a mixer. The phase error signal is filtered and controls the low-noise VCO. A long-term stable lock between the laser and the VCO is obtained.

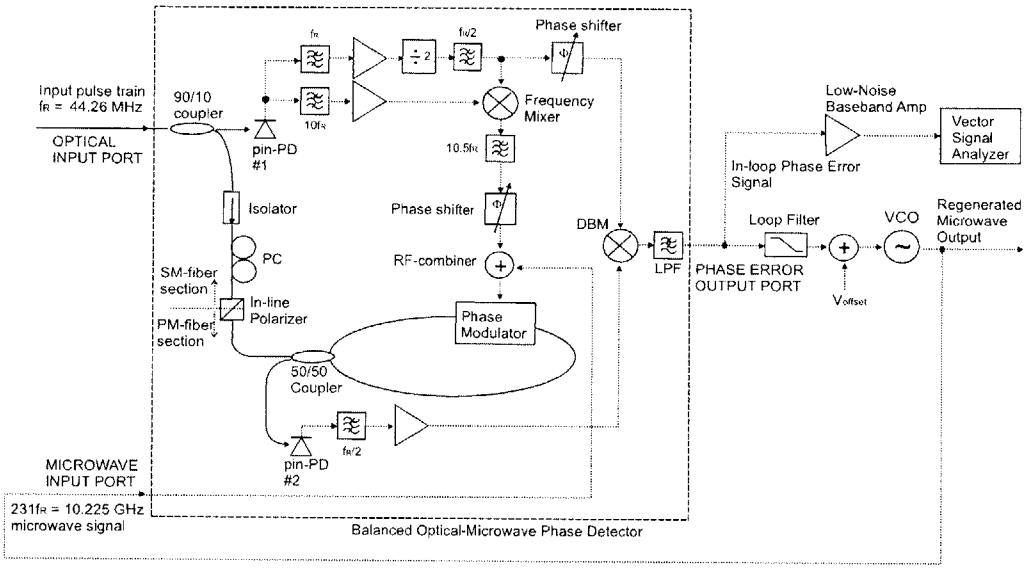

Figure 3-7: Demonstration experimental setup for microwave signal regeneration from an optical pulse train by use of the balanced optical-microwave phase detector [98]. DBM, double-balanced mixer; LPF, low-pass filter; PC, polarization controller; PD, photodiode; PM, polarization-maintaining; SM, non-PM single-mode; VCO, voltage-controlled oscillator. Solid and dotted lines indicate optical (in fiber) and electrical signal paths, respectively.

3.3.3 Out-of-loop Timing Jitter Measurement Results

Figure 3-8 shows the schematic of the experimental setup for out-of-loop relative timing jitter measurements between the two 10.225 GHz microwave signals locked to a free-running 44.26 MHz, 1550 nm stretched-pulse Er-doped fiber mode-locked laser. Two nearly identical optoelectronic PLLs based on balanced optical-microwave phase detectors were built with 10.225 GHz (the 231st harmonic of the fundamental repetition rate, N =231) VCOs (PSI DRO-10.225). The average input optical power

to each Sagnac-loop ($P_{avg,in}$) is 5 mW, and +4 dBm of VCO output power is used to close the PLL. From each VCO, +10 dBm output power at 10.225 GHz can be extracted for external measurements.

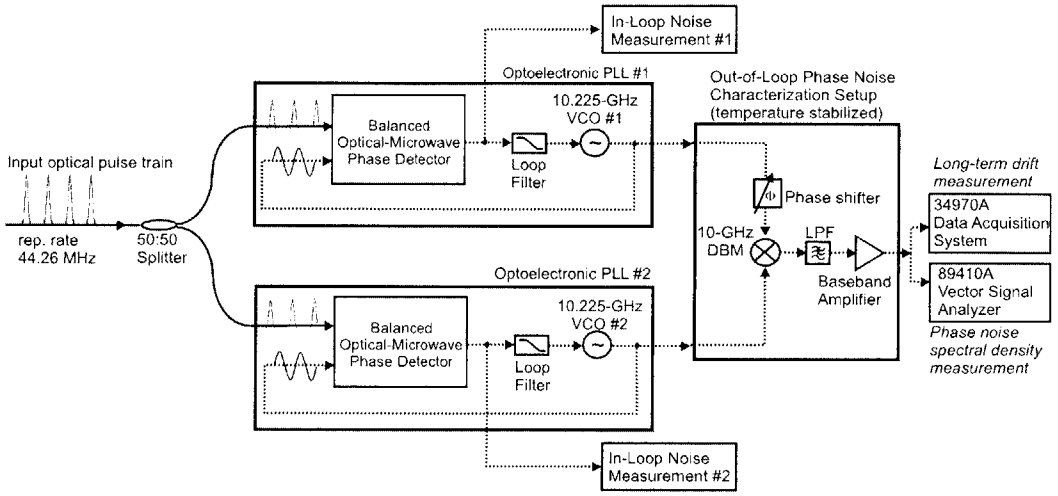

Figure 3-8: Experimental setup for long-term out-of-loop relative timing jitter measurement between two microwave signals locked to a mode-locked laser. DBM: double-balanced mixer, LPF: low-pass filter, PLL: phase-locked loop, VCO: voltage-controlled oscillator.

To evaluate the out-of-loop relative timing jitter between the two extracted microwave signals, the outputs from the locked VCOs are mixed in quadrature in the out-of-loop phase noise characterization setup. The baseband phase error signal is amplified by a low-noise amplifier (G=10 non-inverting amp with AD797) and monitored by a vector signal analyzer (Agilent 89410A) for phase noise spectral density measurements and a data acquisition system (Agilent 34970A) for long-term drift measurements. Note that only the out-of-loop phase noise characterization setup is actively temperature-stabilized to enable a long-term measurement, while both PLLs are not temperature-stabilized or otherwise shielded against environmental perturbations.

Figure 3-9 summarizes the single-sideband (SSB) phase noise spectra for the in-loop and out-of-loop performances between two PLLs when both PLLs are optimized for long-term stable operation. In the locked state, the in-loop timing jitters inte-

grated from 10 Hz to 10 MHz for PLL 1 (curve (b)) and PLL 2 (curve (c)) are 19.2 fs and 18.8 fs, respectively. Most of the noise contribution is from the high frequency (>100 kHz) peak. The noise floor above 5 MHz is caused by the bandpass filter at the reference signal frequency. To evaluate the resolution of the out-of-loop characterization setup, the residual phase noise (curve (d)) was measured when the same 10.225 GHz microwave signal is split and applied to both input ports of the mixer in quadrature. The background timing jitter of the characterization setup itself is 0.8 fs integrated from 10 Hz to 10 MHz. The out-of-loop relative timing jitter between the two extracted 10.225 GHz microwave signals (curve (c)) integrated from 10 Hz to 10 MHz is 12.8 fs. Both in-loop and out-of-loop timing jitters are mostly determined by the high-frequency noise between 100 kHz and 1 MHz. The reason why the in-loop jitter is larger than the out-of-loop jitter is mainly from the high frequency peak characteristic caused by the finite loop bandwidth of about 100 kHz. The enhanced high frequency peak in the in-loop characteristic is reduced in the out-of-loop measurement by limiting the loop filter bandwidths of the PLLs. Although the in-loop results show strong noise suppressions in the low frequency range due to the loop filter integrator, the out-of-loop noise does not show the same strong suppression. In addition, the out-of-loop noise level almost did not move even when changing the parameters such as optical power and microwave signal power levels, which should scale the noise level when the system is shot noise limited as discussed in Section 3.3. With the parameters used in the experiment (photodiode responsivity: R = 0.9 A/W, average output optical power from the Sagnac-loops: P_{avg} = 2 mW, and phase modulation depth of VCO output: Φ_0 =0.3 rad), the shot-noise limited theoretical SSB phase noise level for each loop should be $S_{\varphi,shot} = -152$ dBc/Hz as derived in Eq. 3.25 (line (f)). The measured out-of-loop noise level is about 30 dB worse than the theoretical shot noise limited level. The potential reasons are (1) the uncorrelated noise between $f_R/2$ for the downconversion and $10.5f_R$ for the Sagnac-loop drive, (2) electronic excess noise from the amplification of the output pulse train, and (3) the limited isolation between ports (LO-RF, LO-IF) of the downconversion mixer. The sources of this non-scalable noise are currently under investigation.

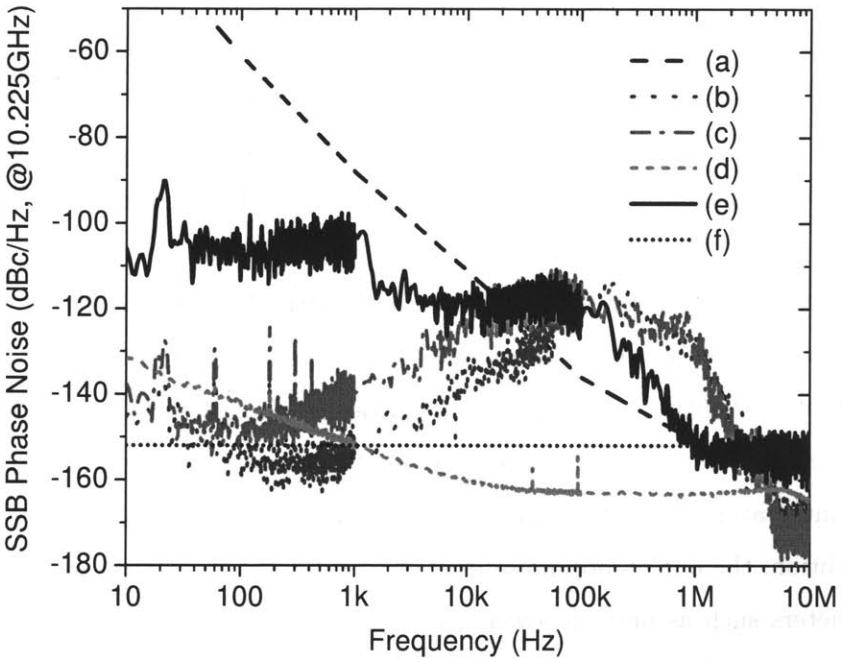

Figure 3-9: Single-sideband (SSB) phase noise spectra at 10.225 GHz from 10 Hz to 10 MHz [100]: (a) free-running VCO (taken from datasheet); (b) in-loop phase noise of PLL 1; (c) in-loop phase noise of PLL 2; (d) residual phase noise of the out-of-loop characterization setup; (e) out-of-loop relative phase noise between PLL 1 and PLL 2; (f) phase noise level in the ideal condition, when both PLLs are shot-noise limited and there is no excess electronic noise sources. The out-of-loop measurement shows 12.8 fs relative jitter between two extracted microwave signals. The in-loop jitters are 19.2 fs and 18.8 fs for PLL 1 and 2, respectively.

3.3.4 Out-of-loop Timing Drift Measurement Results

Although the short-term background jitter (0.8 fs) provides enough resolution for the characterization, the long-term timing drift of the characterization setup itself shows significant amount of drift. Even though the temperature of the characterization setup is actively stabilized within 0.4 $^{\circ}C_{pp}$ (0.07 $^{\circ}C_{rms}$) over 10 hours, at certain time frames, up to 41 fs (in 1 hour) and 48 fs (in 4 hours) timing drifts are observed, as shown in Fig. 3-10 (a). The measured timing drift and the temperature are not clearly correlated, and the exact reasons for this rather abrupt drift are currently not fully understood. Path length variations in the RF cables and connectors that have not been stabilized might be a major cause for this abrupt and large phase fluctuations (note that a 50 fs drift corresponds to a path length change of only 15 μm). This drift in the characterization setup sets the limitation of the long-term drift measurement.

Figure 3-10 (b) shows the result for long-term timing drift measurement between the two 10.225 GHz microwave signals when both VCOs are locked. The output voltage from the characterization setup was recorded every 5 seconds over a time span of one hour. The relative timing between the two microwave signals showed the maximum deviation within 48 fs over one hour. This corresponds to 3 mrad phase stability at the 10.225 GHz carrier frequency. As shown in Fig. 3-10 (a), the characterization setup itself may contribute up to >40 fs drift. Therefore, the long-term timing drift measurement result in Fig. 3-10 (b) is currently limited by the characterization setup itself. Despite of the limitation in the measurement, this measured long-term stability is, to the best of my knowledge, the first time to achieve a 3 mrad-level phase stability of a 10.225 GHz microwave signal extracted from a mode-locked laser over an hour time scale. To overcome the limitation of the long-term drift measurement, it is desirable to use an optical technique for the timing detection to avoid drift of microwave components.

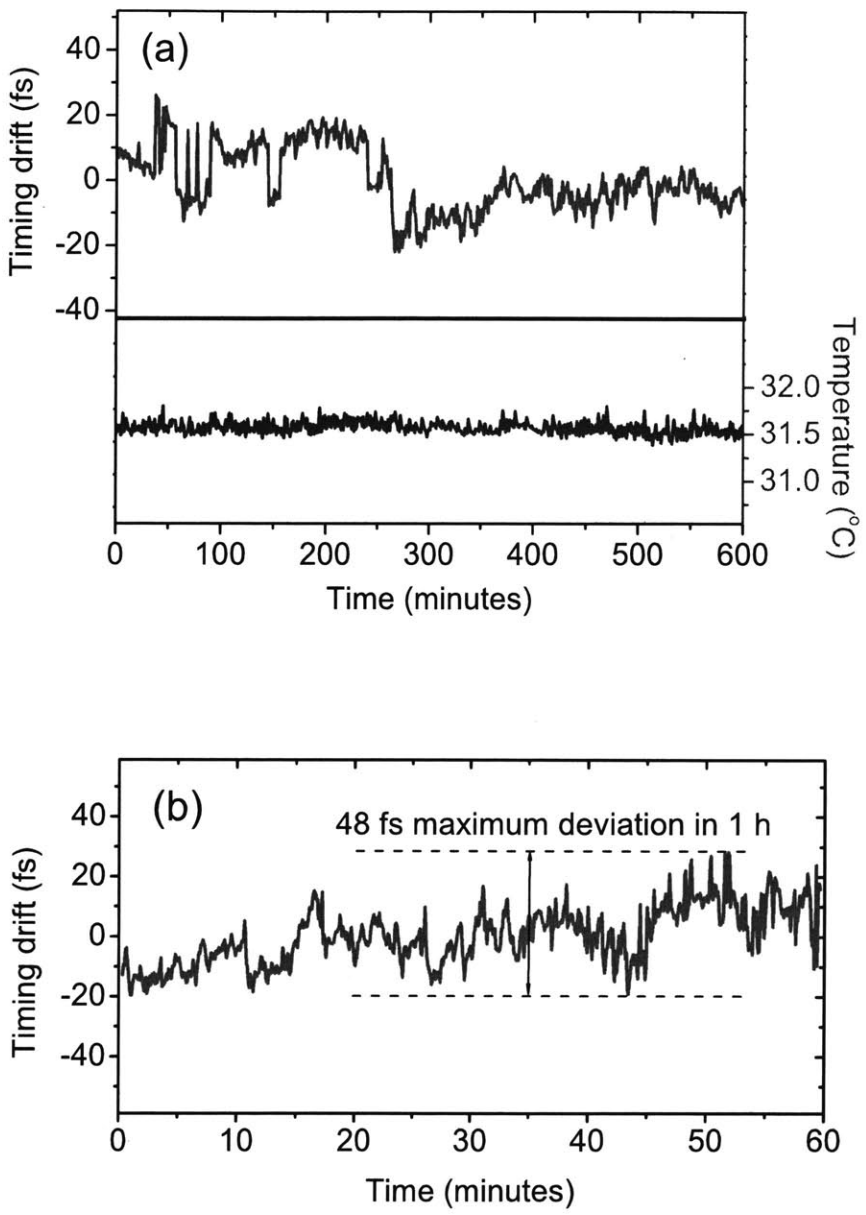

Figure 3-10: Long-term timing measurements [100]. (a) Long-term background timing drift measurement of the characterization setup. Although the temperature is actively stabilized within 0.41 °C (maximum-minimum) over 10 hours, at certain time frames, up to 41 fs (in 1 hour) and 48 fs (in 4 hours) timing drifts are observed. (b) Long-term out-of-loop drift measurement between two locked VCOs shows that the timing drift is within 48 fs over one hour. The data was taken at every 5 seconds.

3.4 Summary and Future Work

In summary, new optoelectronic PLLs based on detection of timing information between optical pulse trains and microwave signals in the optical domain are demonstrated for long-term stable microwave signal synthesis from mode-locked lasers.

The first version based on intensity balancing between two outputs from a free-space Sagnac loop interferometer resulted in 60 fs timing jitter between a 100 MHz pulse train and a 2 GHz microwave signal. The performance was mainly limited by the high V_π (31.4 V) of the free-space phase modulator and the high frequency noise of the VCO. Although the noise scalability has a limitation due to the limited applicable optical power to the photodiode, with a proper modulator with lower V_π (which leads to a higher Φ_0) and a better VCO, this scheme can achieve much better noise performance. In particular, its extremely simple electronic configuration – two photodiodes followed by a passive RC loop filter – provides much simpler interface between optical and electrical domains compared to the other techniques.

The second version based on a balanced optical-microwave phase detector could achieve long-term stable (<3 mrad over 1 hour) microwave signal extraction from a mode-locked laser at the frequency of 10.225 GHz and the power level of +10 dBm. This excellent long-term phase stability is achieved by electro-optic sampling of the microwave signal with the optical pulse train in a differentially-biased Sagnac-loop interferometer. The relative short-term out-of-loop timing jitter integrated from 10 Hz to 10 MHz is 12.8 fs. The long-term timing measurement shows the maximum deviation within 48 fs over one hour, which is mainly limited by the drift of the characterization setup itself (up to 41 fs in 1 hour; up to 48 fs in 4 hours). This is the first time to achieve a 3 mrad-level phase stability of a 10.225 GHz microwave signal extracted from a mode-locked laser over an hour time scale. The demonstrated performance is currently limited by the electronic noise sources rather than the shot noise, and the potential of noise scalability is not yet fully exploited. By identifying and removing the non-ideal technical noise sources, it is expected to reach shot noise limited performance with long-term drift-free operation.

In terms of implementation of these devices, I envision that the high-precision microwave signal synthesizers based on mode-locked lasers and optoelectronic PLLs can be implemented both at the instrument level (fitting, for example, in a 19" rack) and at the integrated circuit level in the near future. With the currently available optical and microwave devices, the balanced optical-microwave phase detectors can be implemented in an instrument for research laboratories and facilities requiring high-precision microwave signals referenced to optical master oscillators. In addition, with the recent advance of microphotonic fabrication techniques and electronic-photonic integration using high index contrast materials on silicon chips, the optoelectronic PLLs can be also implemented on an integrated chip in the near future. For example, $Si/SiN/SiO_2$-based system will be used for fabrication of the Sagnac loop, Si-modulator, Si- or Si/Ge-photodetectors and low- and high-speed CMOS or Si/Ge-heterostructure bipolar transistor circuits. The integration of the demonstrated optoelectronic PLLs on a silicon chip is currently in progress in a collaboration with the Sandia National Laboratory.

Finally, the potential near-future applications include microwave signal read-out from atomic optical clocks [88], large-scale timing distribution and synchronization systems [94], locking a mode-locked laser to a microwave standard, synchronization of multiple mode-locked lasers to the common microwave signal, and high-precision (and relatively low-cost compared to the state-of-the-art Sapphire-loaded cavity oscillators) microwave signals synthesizer in general.

Chapter 4

Timing Stabilized Fiber Links for Large-Scale Timing Distribution

4.1 Motivation

Precise optical timing distribution to remote locations is important for large-scale facilities requiring high-precision synchronization, for example, seeded x-ray free electron lasers [20] and phased-array antennas [86]. It is also crucial for the high-precision time and frequency standard distribution over long distances [81, 101, 102, 103, 104]. The conventional timing distribution based on coaxial RF-cables cannot achieve the required precision, e.g., long-term drift-free sub-10 fs timing jitter level. Therefore, optical techniques for timing distribution is highly desirable for such high-precision large-scale facilities.

In the envisioned timing distribution system, the timing signal in form of an optical pulse train generated from a mode-locked laser is distributed to the remote RF- or optical-subsystems that we aim to synchronize with minimal excess noise. The use of optical pulse trains from mode-locked lasers for the timing distribution has many advantages [105] compared to the cw-transfer techniques [106], such as: (i) any harmonic components of fundamental repetition rate can be recovered at the end stations; (ii) the group delay of the fiber link is directly stabilized; (iii) Brillouin scattering and residual reflections are strongly suppressed; (iv) optical cross-correlation

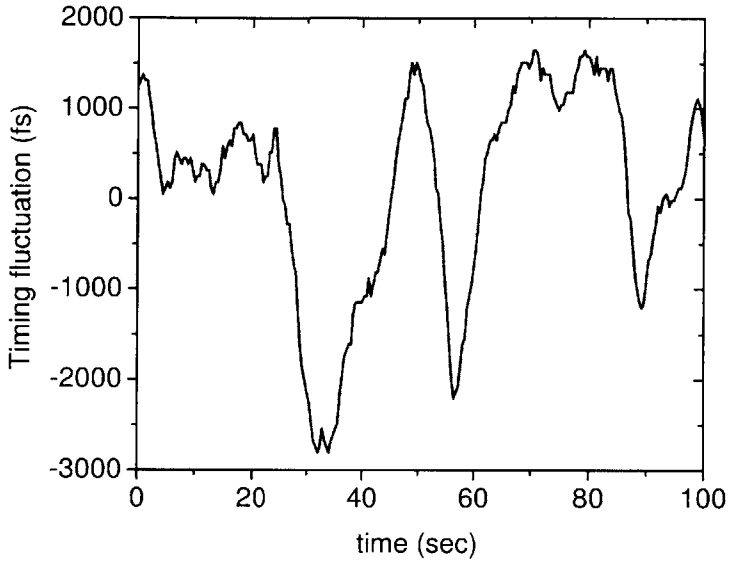

Figure 4-1: Timing drift caused by fiber length fluctuations in an uncompensated 300 meter long fiber link. In 100 seconds time scale, timing drift up to 4.5 ps is observed.

can be easily employed for various optical stabilization and synchronization tasks; and (v) the pulse train can be directly used to seed optical amplifiers. Although there are two disadvantages in using optical pulses, (i) the impact of fiber nonlinearities such as self-phase modulation (SPM) and Raman effects [107] and (ii) the necessity of dispersion compensation for cross-correlation, these effects are not too severe if the repetition rate of the mode-locked laser can be chosen high enough, i.e., a few hundreds MHz.

In the implementation of such systems, acoustic noise and thermal drifts introduced to the fiber involved in the distribution must be cancelled by a proper feedback loop. Figure 4-1 shows the measured timing drift in an uncompensated 300 meter long fiber link over 100 seconds in a laboratory environment. Timing change up to 4.5 ps is observed in just 100 seconds time scale. Note that 1 μm of fiber length change corresponds to 5 fs of timing error. The measurement result shows that 3×10^{-6} length fluctuation of the fiber link can easily happen in a minute, and for a long dis-

tance fiber transfer over several hundreds meters, this creates more than a picosecond timing error. For long-term drift-free optical timing distribution with femtosecond precision, this timing error sets a serious limitation. In this Chapter, long-term drift-free timing link stabilization based on a novel single-crystal balanced cross-correlator is demonstrated.

4.2 Timing Stabilization

As visualized in Fig. 4-2, the timing stabilization of a fiber link can be implemented by a fiber length control loop by referencing the back-reflected pulse from the fiber end with the later pulse directly from the mode-locked laser. In this scheme, if the fiber length is L, the stabilization bandwidth is set by the pulse travel time 2L/c, where c is the speed of light in the fiber. For effective stabilization, we assume that no length fluctuations are faster than 2L/c. This is a valid assumption for a timing link up to a few kilometers length scale because most of the noise contribution to the link is from acoustic vibration (within a few kHz frequency range) and much slower temperature drift. For a 1-km fiber length, the bandwidth limitation is set about c/2L = 100 kHz.

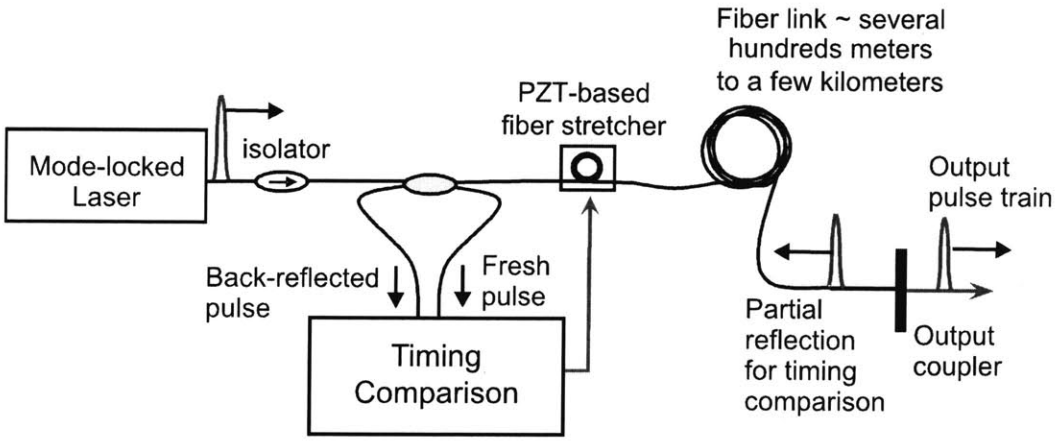

Figure 4-2: The concept of timing link stabilization by comparing a back-reflected pulse with a later fresh pulse directly from the laser.

The most critical and challenging issue is how to compare the reflected pulse with

the pulse directly from the mode-locked laser and extract an accurate timing error signal. So far, electronic techniques based on high-speed photodetectors and microwave mixers have been used to stabilize fiber links on a rather short-term time scale [26, 27]. The limited timing resolution as well as large thermal drifts of microwave components makes it difficult to stabilize links better than 100 fs in a long-term stable way. For example, typical 10 GHz microwave mixers have $\sim$1 μV/fs timing resolution and $\sim$70 fs/K thermal coefficient [77].

To overcome these limitations set by the performance of microwave components and techniques, it is highly desirable to use optical cross-correlation techniques [76] for high-resolution and drift-free detection of timing errors between two optical pulses. In particular, a balanced cross-correlation configuration [44] is preferred to suppress the laser amplitude noise. Previously, a balanced cross-correlator for long-term (>12 hours) sub-fs synchronization of two independently mode-locked lasers operating at different center wavelength [44, 79] was demonstrated (more detailed information on this technique is also presented in Section 2.6). However, this method is limited to the case of optical pulses with different center wavelengths because the delay between the two input pulses is generated by group delay dispersion (GDD). It is not applicable to the case when the two optical pulses have the same center wavelength, such as the timing link stabilization. In the next section, a single type-II phase-matched periodically poled $KTiOPO_4$ (PPKTP) crystal is introduced to construct a compact and self-aligned balanced cross correlator for precise timing detection.

4.3 Single-Crystal Balanced Cross-Correlator

The single-crystal balanced cross-correlator consists of (a) generation of a group delay difference between two orthogonally polarized - otherwise identical - pulses, and (b) broadband second-harmonic generation (SHG) by a type-II phase-matched nonlinear crystal. Using the group delay resulting from the birefringence between the two orthogonal polarizations in the crystal enables the implementation of balanced cross-correlation at the same wavelength. The detected signal is background free, i.e., if

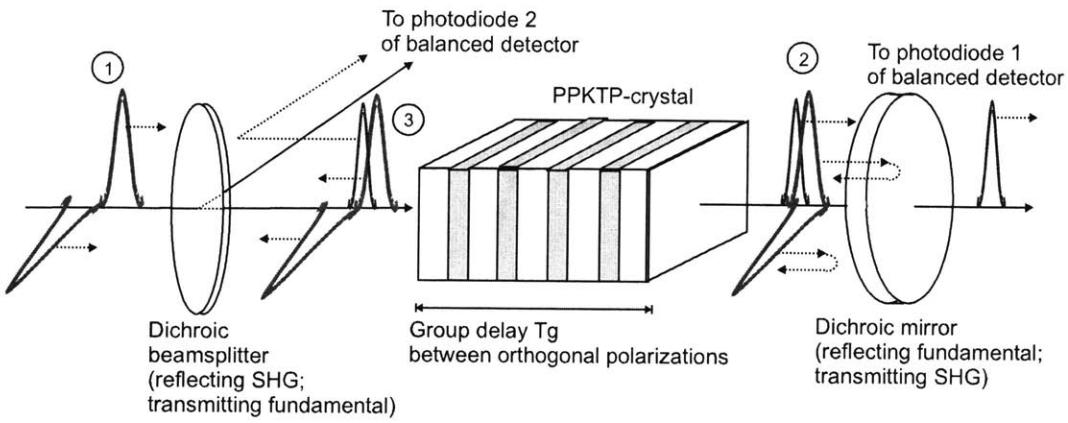

Figure 4-3: Operation of a single-crystal balanced cross correlator. SHG, second-harmonic generation.

the pulses do not overlap in time, the detector signal is vanishing. Moreover, the group delay and the SHG functions can be combined in a single nonlinear crystal. For construction of a cross-correlator at 1550 nm, the use of a PPKTP crystal is especially advantageous because of the extended phase-matching bandwidth of 100 nm centered near 1550 nm [108].

For collinear type-II phase-matched SHG under optimum focusing conditions, we obtain the following optimum conversion efficiency:

$$\eta_{\text{opt}} = \frac{8\pi^2 Z_0}{\lambda^3}\frac{d_{\text{eff}}^2}{n^3} \cdot 5.68 \cdot l \cdot \frac{P_{\text{peak,in}}}{\sqrt{2}} \tag{4.1}$$

where $Z_0 = \sqrt{\mu_0/\epsilon_0}$ is the free-space characteristic impedance, λ is the wavelength of the input, d_{eff} is the effective nonlinear coefficient, n is the refractive index of the nonlinear crystal, l is the walkoff length, and $P_{\text{peak,in}}$ is the peak power of the input pulse. For input pulses with 200-fs pulsewidth and 77-pJ pulse energy at 1550 nm, the optimum conversion efficiency of PPKTP is calculated as $\eta_{\text{opt,PPKTP}} \simeq 8 \times 10^{-3}$. The measured efficiency with a 4-mm long PPKTP crystal with a poling period of 46.2 μm is $\eta \simeq 60\mu W/15mW = 4 \times 10^{-3}$, which shows a fairly good agreement with the optimum theoretical efficiency.

Figure 4-3 shows the operation of the single-crystal balanced cross-correlator. The input pulses are transmitted through a first dichroic beamsplitter which transmits

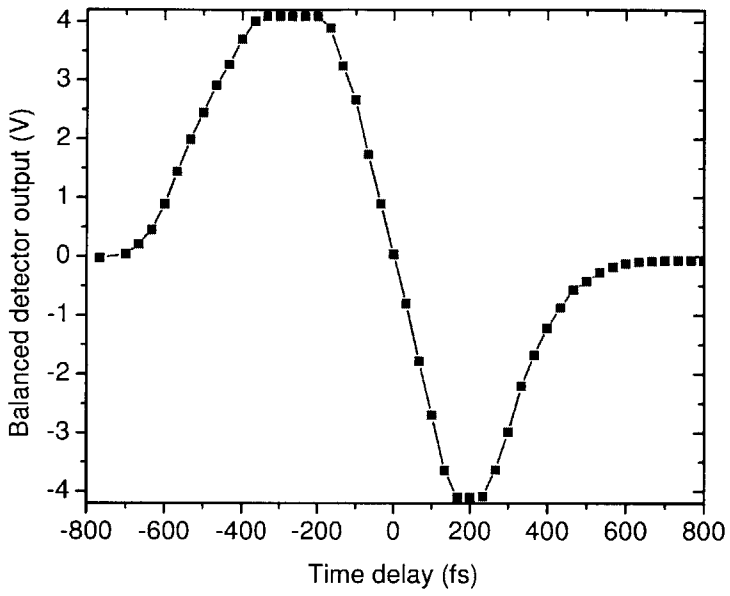

Figure 4-4: Balanced autocorrelation using 77 pJ, 200 fs pulses at 1550 nm. The trace is clipped by the maximum output voltage of the detector (4 V).

the input pulses but reflects the SHG of the input pulses. The pulses are focused into a type-II phase-matched PPKTP crystal. The generated SHG component is transmitted through the second dichroic mirror and detected by photodiode 1 in the balanced detector. The remaining fundamental input pulses are reflected from the dichroic mirror and again focused into the PPKTP crystal. The SHG component generated by the back-reflected pulses is separated by the dichroic beamsplitter and detected by photodiode 2 in the balanced detector. At the balanced detector output, a signal proportional to the relative position between the two input pulses is extracted. Figure 4-4 shows the measured autocorrelation trace of a 77 pJ, 200-fs pulse at 1550 nm using a balanced cross-correlator with a 4-mm long PPKTP crystal (poling period = 46.2 μm). This PPKTP crystal was designed by Dr. Franco N. C. Wong of MIT and fabricated by Raicol Crystals Ltd.

4.4 Demonstration of Timing Link Stabilization

Figure 4-5 shows the schematic for a 310-meter timing stabilized link using the single-crystal balanced cross-correlator.

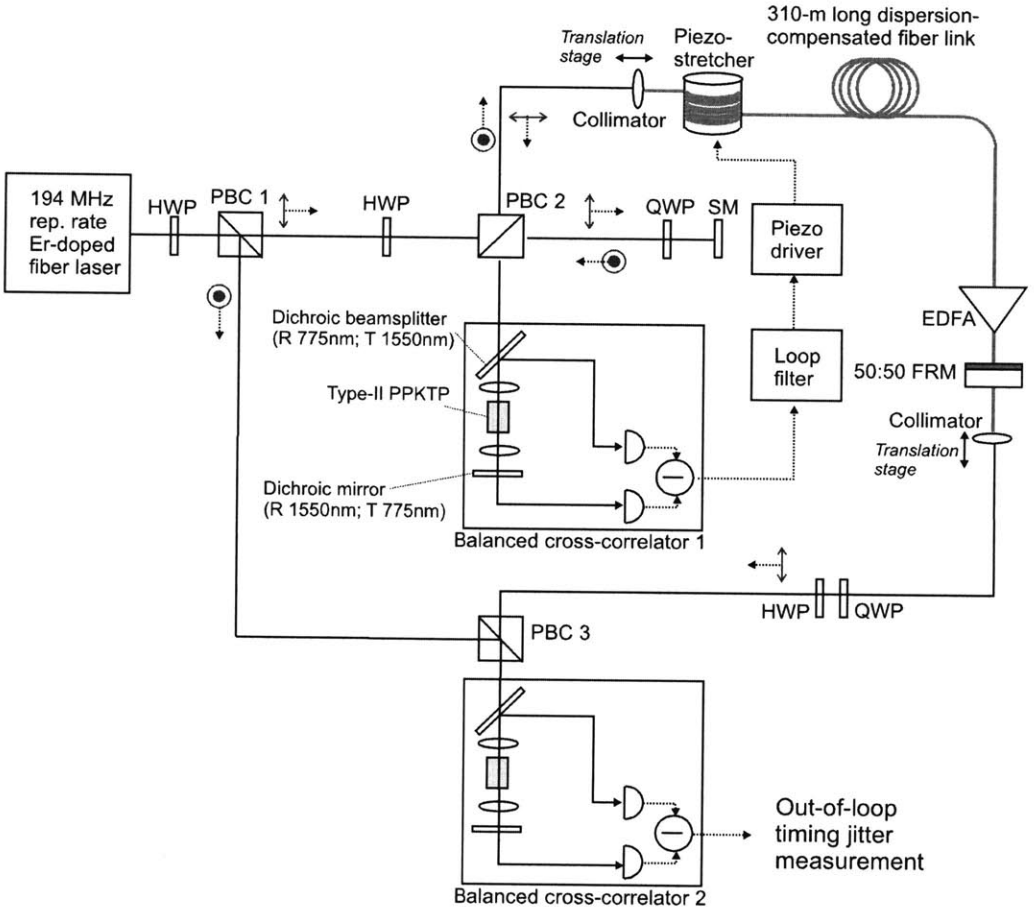

Figure 4-5: Schematic for timing link stabilization using a single-crystal balanced cross correlator [109]. EDFA, Er-doped fiber amplifier; FRM, Faraday rotating mirror; HWP, half-wave plate; PBC, polarizing beamsplitter cube; QWP, quarter-wave plate; R, reflection; SM, silver mirror; T, transmission.

A 194-MHz soliton Er-doped fiber laser [12] is used as the optical pulse source. The output power is 40 mW and the pulsewidth is 200 fs. Part of the input pulse train is tapped off by a polarizing beamsplitter cube (PBC 1 in Fig. 4-5) to the out-of-loop characterization setup. The other part of the light is transmitted through a 310-

meter long dispersion-compensated fiber link containing a piezo-stretcher. The fiber link is comprised of ~40 meter of dispersion-compensating fiber (DCF) ($D_2 \simeq -114.3$ ps/km/nm) and ~270 meter of SMF-28 fiber ($D_2 \simeq +17$ ps/km/nm). Half of the link-transmitted pulses are back-reflected by a 50:50 Faraday rotating mirror (FRM) at the end of the fiber link. With the FRM, the polarization state of the returning pulse is orthogonal to that of the input pulse, which enables 100 % transmission through PBC 2 (in Fig. 4-5). Due to the coupling loss of the collimator, the splicing loss between DCF and SMF-28 fiber and the insertion loss inside the FRM, the loss is more than 10 dB for the reflected pulses compared with the input pulses. To compensate those losses in the transmission, an Er-doped fiber amplifier (EDFA) is added at the end of the fiber link. The reflected pulse (measured pulsewidth ~ 420 fs) is combined with the fresh pulse directly from the laser at the polarizing beamsplitter cube (PBC 2 in Fig. 4-5). The combined pulses are applied to the balanced cross-correlator (balanced cross-correlator 1 in Fig. 4-5). The error signal generated from the balanced cross-correlator is regulated by a loop filter and applied to the piezo-stretcher in the link via a high-voltage piezo driver. This closes the timing stabilization loop. When it is locked, the timing fluctuation introduced to the fiber link is compensated by the counteraction of the piezo stretcher. To evaluate the out-of-loop performances, a second balanced cross-correlator (balanced cross-correlator 2 in Fig.4-5) is used to compare the transmitted pulses through the 310-meter link with fresh pulses directly from the mode-locked laser.

4.5 Measurement Results

Figure 4-6 and 4-7 summarize the measurement result of the stabilized fiber link. Figure 4-6 shows the out-of-loop timing jitter spectral density in units of fs/$\sqrt{\text{Hz}}$. The out-of-loop rms-timing jitter integrated from 10 Hz to 100 kHz (detector bandwidth) is 9.2 fs, where the detector background noise corresponds to 8.2 fs.

The top trace of Fig. 4-7 shows the long-term out-of-loop timing jitter trace over 100 seconds measured with an oscilloscope. The rms-value of this measurement

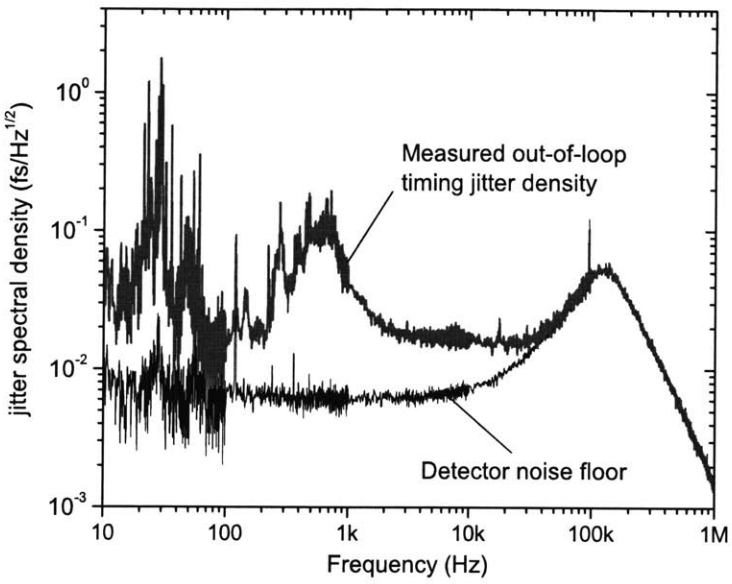

Figure 4-6: Measured out-of-loop timing jitter spectral density [109]. The integrated rms jitter from 10 Hz to 100 kHz is 9.2 fs. The detector noise floor corresponds to 8.2 fs jitter, which sets the limits in measurement accuracy.

confirms the stabilization to a precision of 9.7-fs. The jitter analysis was mainly limited by the limited signal-to-noise ratio of the detection. With a higher optical power level and/or lower losses in the fiber link as well as a lower noise balanced photodetectors, it is clearly possible to improve the locking performance as well as the measurement resolution.

The bottom trace of Fig. 4-7 shows the displacement of the piezo stretcher in the fiber link during the same time frame. The fiber link used in this experiment is not temperature, vibration, nor airflow stabilized, and the locking is broken purely by the limited displacement range of the used piezo stretcher ($\sim$700 μm, corresponding to 2×10^{-6} length fluctuation of the whole fiber link). With additional manual adjustment of the translation stage, the lock could be kept for more than one hour. To the best of my knowledge, this result is the first long-term 10-fs level stabilization of a fiber link. It also indicates that adding a motorized translation stage and polarization control at

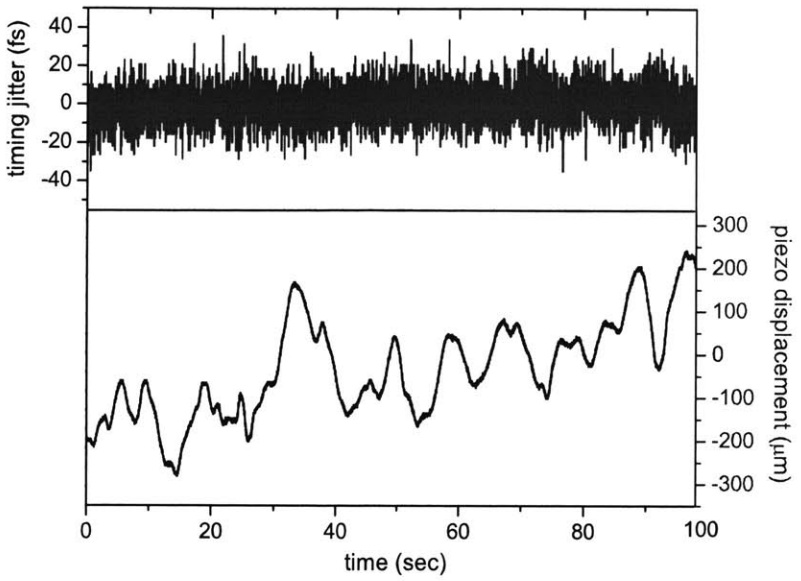

Figure 4-7: Long-term out-of-loop timing jitter trace (top trace) and piezostretcher displacement (bottom trace) over 100 seconds [109]. The rms jitter over 100 seconds is 9.7 fs.

the end of the fiber will enable to maintain this level of accuracy in synchronization as long as desired.

4.6 Test in an Accelerator Environment

After the first demonstration in a laboratory environment, the cross-correlator based timing link stabilization was implemented in a real accelerator environment at the Deutsches Elektronen-Synchrotron (DESY), Hamburg, Germany. A 400 meter long fiber link is installed in the operating FLASH (Free electron LASer in Hamburg) free electron laser. To test the influence of a noisy environment, the fiber is installed around the circumference of the accelerator hall. To correct the large timing drift of more than 10 ps, which is beyond the range that a fast piezostretcher can compensate for, an additional motorized optical delay line (ODL) is installed.

Figure 4-8 shows the timing stability of the fiber link over 12 hours. The timing

jitter in 100 seconds is 4.4 fs, and the slow timing drift over 12 hours is less than 25 fs. The overall displacement of the ODL was 40 ps over 12 hours. This long-term femtosecond level accuracy is not attainable with conventional coaxial RF distribution systems widely used in accelerator facilities. The potential sources of the drift are imperfect balancing of the out-of-loop cross correlator and the polarization mode dispersion (PMD) in the fiber link. An additional polarization control loop might be helpful to avoid the PMD limitations.

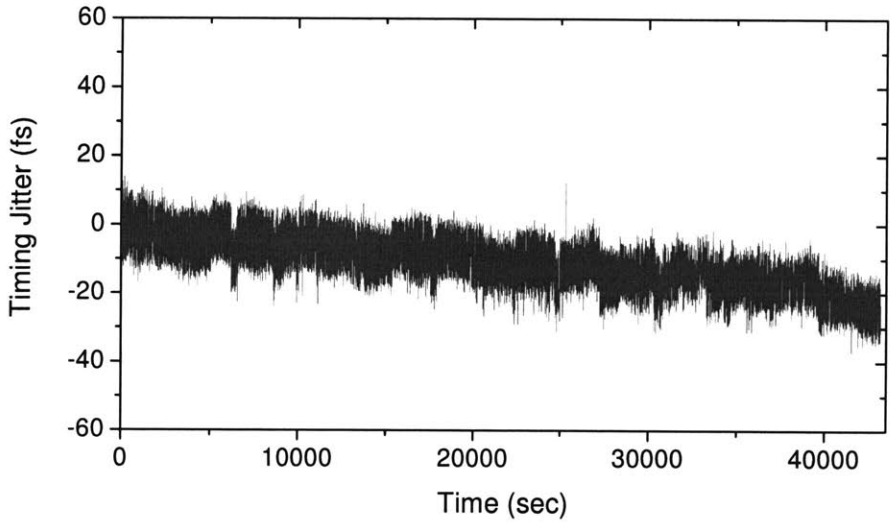

Figure 4-8: Out-of-loop timing jitter measurement of a 400 meter long fiber link over 12 hours in an accelerator environment (FLASH machine in DESY). The short term (<100 s) timing jitter is 4.4 fs. The long-term drift over 12 hours is less than 25 fs. Data courtesy of Florian Loehl [110].

4.7 Summary and Future Work

In summary, a self-aligned, single-crystal balanced cross-correlator comparing the timing between optical pulses at the same center wavelength is demonstrated. As a first application of this single-crystal balanced cross-correlator, long-term 10-fs precision

stabilization of a 310-meter fiber link is demonstrated in a laboratory environment. Further, the same technique is applied in a real accelerator environment, and it showed less than 25 fs timing drift over 12 hours time scale.

The potential applications of the single-crystal balanced cross-correlator include drift-free sub-fs synchronization of two lasers operating at the same center wavelength, fiber link stabilization for large-scale timing distribution, and high-frequency timing jitter measurements of mode-locked lasers [111]. It is also possible to implement a compact balanced cross-correlator as a fully packaged waveguide device using periodically poled waveguide structures in the near future.

As for the timing stabilized fiber link, further investigation is necessary to remove the slow drift over hours. The implementation of a separate polarization state control loop is in progress, and the impact of fiber PMD, as well as the wavelength dependent polarization rotation in the EDFA, will be further investigated. In addition, the ultimate test of link stabilization performance will be done by building two independently stabilized fiber links and comparing the delivered outputs from the two links.

This timing stabilized fiber link will play an important role in large-scale facilities requiring high-precision remote synchronization performance. As shown in Section 4.6, the preliminary test was already done at DESY (Hamburg, Germany). In addition, this timing link technique has recently been transferred to the Instrumentation Group of ELETTRA (Trieste, Italy) to construct their timing distribution system in the FERMI-FEL facility in November 2007. Another important application is the enhancement of long-term stability in transfer of time and frequency standard over long distances.

Chapter 5

Optical Subsampling Downconverter for Analog-to-Digital Conversion of Narrowband High-Frequency Microwave Signals

5.1 Motivation

Already in the early 1970s, several research groups proposed and demonstrated the applications of optical components and techniques in analog-to-digital conversion of electronic signals [112, 113, 114]. Although many researchers investigated various types of "photonic" analog-to-digital converters (ADCs) over 30 years, any photonic ADCs have not been used in commercial ADCs to date [115]. The major reason for this little impact is more rapid advance of electronic ADC techniques in the same period. However, recently the ADC has become one of the major bottlenecks in mixed signal circuits and systems because of even more rapid progress in digital electronics. Therefore, to overcome the current limits in resolution and speed in ADC, photonic

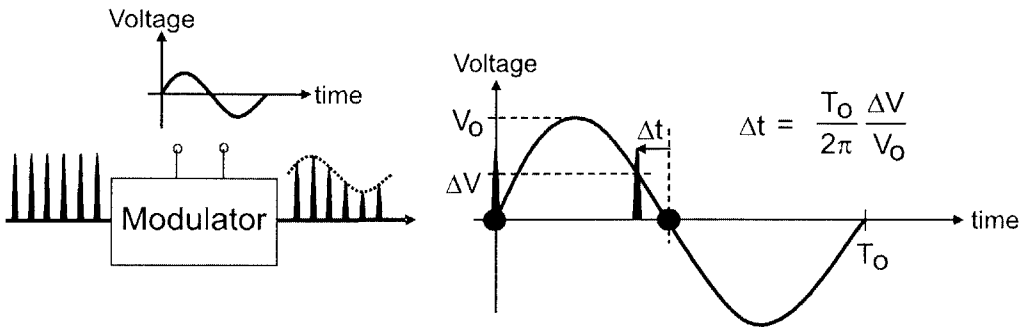

Figure 5-1: Simplified schematic of the photonic ADC.

ADC techniques regain interests with the recent advance in telecommunication-grade optical components and microphotonic integration.

The use of optical pulse trains for the sampling of microwave and RF signals might be a natural idea in the sense that the pulse train resembles the ideal impulse train in the definition of sampling. However, a more important advantage of using an optical pulse train for sampling is its much lower timing jitter compared to the electronic clock signals.

Figure 5-1 shows a simplified example of illustrating the importance of timing jitter. An electronic signal is sampled by an optical pulse train using an intensity modulator. The timing jitter (Δt) of the pulse is transferred to the voltage error (ΔV) and leads to the lower resolution when the pulse samples the electronic signal. In the case of sinusoidal electronic signal, the maximum voltage error occurs at the zero crossings where the slope is the maximum. A simple calculation gives the relationship between the timing jitter and the voltage error as

$$\Delta t = \frac{T_0}{2\pi}\frac{\Delta V}{V_0}, \tag{5.1}$$

where T_0 and V_0 are the period and amplitude of the sinusoidal electronic signal, respectively.

For sampling of a 40 GHz signal with 8-bit resolution, which is not achieved with conventional ADC techniques to date, the required timing jitter is less than $\left(\frac{25\text{ps}}{2\pi}\right)\left(\frac{2}{(2^8-1)\sqrt{12}}\right) \simeq 9$ fs. This is clearly the range beyond conventional electronic

sources can achieve (0.5-2 ps rms jitter [116]). However, sub-10 fs jitter is feasible with optical pulse trains from mode-locked lasers as shown in Ref. [14]. Therefore, the photonic ADC has an advantage over its electronic counterpart especially for sampling high frequency (>10 GHz) microwave signals.

The focus of this Chapter is how to sample and digitize a narrowband high-frequency (>10 GHz) microwave signal with optical pulse trains. This is important for narrowband radar and communication systems operating at high carrier frequency. In addition, in the context of large-scale timing distribution and synchronization systems introduced in Section 1.2, it can be used as a diagnosis tool for the high-frequency microwave signals. This work is done in a close collaboration with Matthew Park and Prof. Michael Perrott of the MIT High Speed Circuits and Systems Group.

5.2 Operation

The basic idea is downconverting the narrowband high-frequency (near Nf_{rep}) microwave signal to the baseband by subsampling with optical pulse train with a fundamental repetition rate of f_{rep}. Figure 5-2 shows the schematic of the optical subsampling downconverter.

The first step is frequency-mixing the narrowband high-frequency microwave signal with the optical pulse train in the optical domain. This is done by applying the optical pulse train with a repetition rate f_{rep} to the intensity modulator driven by the microwave signal with a frequency $\sim Nf_{rep}$ that we aim to sample. Then the spectrum of microwave signal is copied at every harmonic of the repetition rate including at $f = 0$ (baseband) in the frequency domain, as shown in Fig. 5-2. By lowpass filtering the baseband copy, one can downconvert the high-frequency microwave signal to the baseband in the optical domain.

The second step is transferring the information in the optical domain to the electronic domain. This can be done by applying the modulated optical pulse train to a photodiode connected to an on-chip current source and capacitor.

The final step is digitizing the downconverted electronic signal. For this, a continuous-

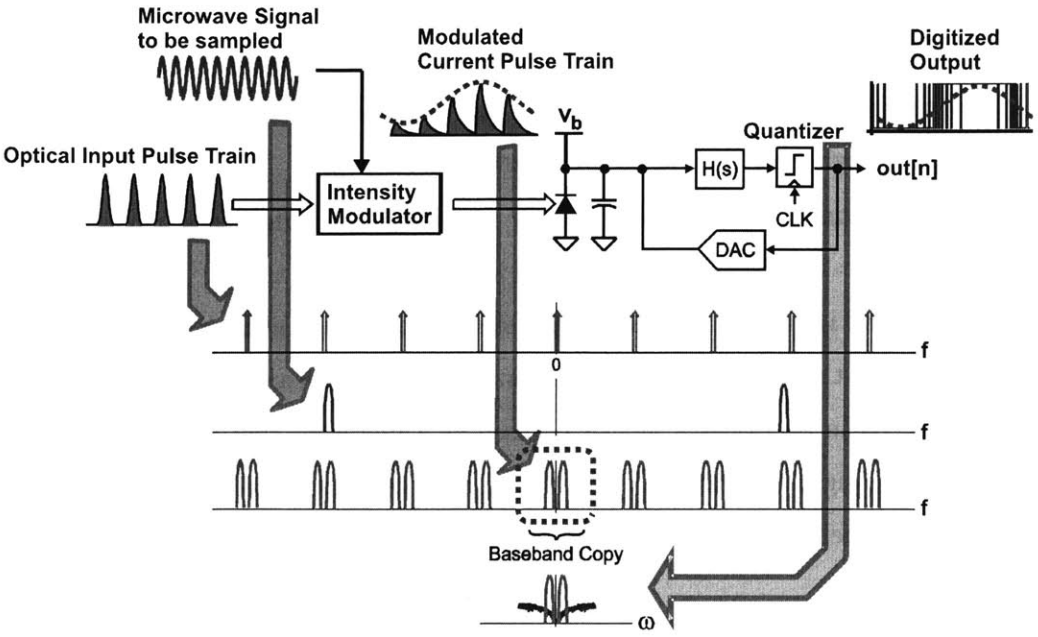

Figure 5-2: Schematic of the optical subsampling downconverter [117].

time (CT) delta-sigma ADC is used. A delta-sigma converter is a widely-used oversampling technique. In essence, the baseband analog signal is digitized by a 1-bit resolution ADC operating at a very high sampling rate in conjunction with noise shaping and digital filtering [118]. The 1-bit DAC is used to keep the input of the quantizer at zero in average by a feedback loop between the input and the digitized output. By this delta-sigma modulator, a noise spectrum is shaped like a highpass filter that enhances the signal-to-noise ratio (SNR) in the frequency band of interest as shown in Fig. 5-2. By sending the oversampled 1-bit serial stream to a digital filter and digitally resampling it by a decimator, one can decode the final output, the digitized n-bit resolution baseband signal.

5.3 Experiments and Measurement Results

The used optical pulse source is a 193.5 MHz repetition rate soliton mode-locked Er-fiber laser [14]. It generates a train of ~200 fs optical pulses centered at 1550 nm. The measured timing jitter is 29 fs integrated from 1 kHz to 10 MHz.

The pulse train is applied to a dual-output 10 GHz $LiNbO_3$ Mach-Zehnder intensity modulator. The two outputs from the modulator are differentially modulated:

$$P_{out1} = P_{in} \sin^2 \left(\frac{\pi}{2} \frac{V_{in}(t)}{V_\pi} \right),$$
$$P_{out2} = P_{in} \cos^2 \left(\frac{\pi}{2} \frac{V_{in}(t)}{V_\pi} \right), \tag{5.2}$$

where P_{in} is the input optical power, $V_{in}(t)$ is the voltage signal applied to the modulator (that we aim to sample), and V_π is the half-wave voltage of the modulator. With a DC bias $V_{in,DC} = V_\pi/2$, two outputs are operated in a fully differential way. The used modulator is manufactured by Lucent Technologies in the 1990s and rented from MIT Lincoln Laboratory. The exact characteristics of the modulator are unfortunately not well-known nor documented. Some in-lab measurements revealed that the modulator shows a large insertion loss both for optical signals and electrical signals at 10 GHz. In addition, the two outputs have unmatched modulation characteristics that results in different modulation depths for the two outputs. These problems seriously limited the performance of the ADC as will be shown later in this section.

The used microwave carrier frequency is 9.4825 GHz. It is set to the 49th harmonic of the fundamental repetition rate (193.5 MHz) plus 1 MHz ($f_{RF} = 49 f_{rep} + 1$ MHz). A 1 Mbps GMSK signal with a 9.4825 GHz carrier frequency is generated by Agilent E8267D PSG vector signal generator.

The used photodioes are off-chip fiber-pigtailed InGaAs pin-photodiodes with 75 μm active area (from PD-LD Inc).

The delta-sigma modulator as well as digital electronic part is implemented as an integrated circuit chip designed by Matthew Park. The custom IC is fabricated in the 0.18 μm CMOS process of National Semiconductor. The IC area is 0.64 mm^2 and the power consumption is 47 mW. More detailed information on the circuit design is presented in Ref. [117]. The ADC is clocked at 193.5 MHz, that is matched with the fundamental repetition rate of the mode-locked laser. This clock rate provides an over-sampling ratio (OSR) of 48.4 ($= 193.5/(2 \times 2)$) over an effective bandwidth of 2 MHz.

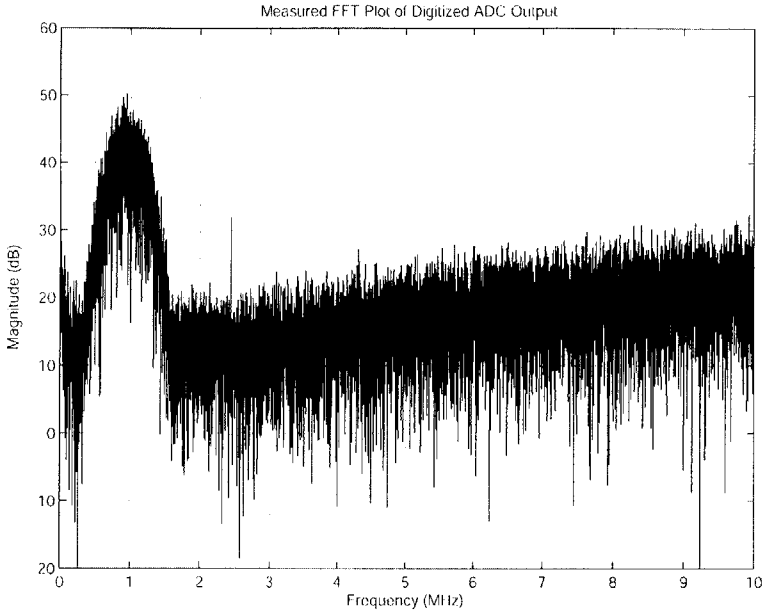

Figure 5-3: Measured FFT of the digitized baseband output [119].

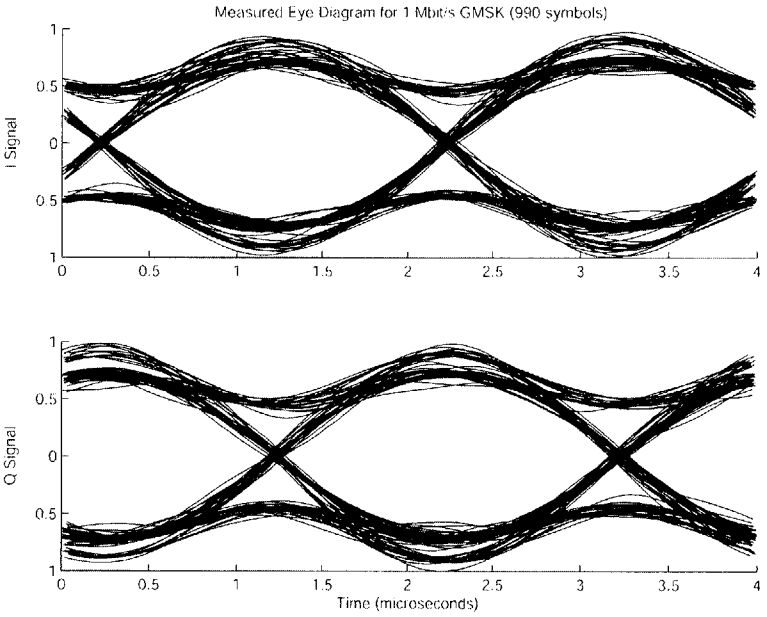

Figure 5-4: Measured eye diagrams of the received I and Q data patterns [119].

Figure 5-3 shows the measured FFT of the digitized baseband output. The measured SNR is 32 dB over an effective bandwidth of 2 MHz. The maximum signal to noise-plus-distortion ratio (SNDR) is 22 dB over the same bandwidth. This number is much lower than the predicted SNDR of 54 dB assuming ideal case when the shot noise limited SNR and the modulator nonlinearity limited spurious-free dynamic range (SFDR) are balanced.

This discrepancy is mainly originated from the imperfect optical components. First, the mismatching between two differential outputs from the optical modulator resulted in imperfect suppression of the 2nd order distortion. The measured SFDR was limited by the 2nd order and not the 3rd order harmonic component. Second, the large insertion loss of optical and microwave signals at the optical modulator reduced the dynamic range. It turned out to be that only 5 % of usable ADC dynamic range was used in the experiment [119]. Finally, the used photodiodes were not matched pairs and had limited linear range (<1 mW).

Despite of the limited performance, the ADC could digitize the modulated signal with wide-open eyes in the eye diagrams as shown in Fig. 5-4. Note that this eye diagram is generated directly from the digitized ADC output by performing decimation, demodulation and filtering on the data using MATLAB [119].

5.4 Summary and Future Work

In summary, an optical subsampling downconverter is demonstrated for analog-to-digital conversion of narrowband high-frequency (>10 GHz) microwave signals. The measured maximum SNR and SNDR of a 1-Mbps GMSK signal at 9.4825 GHz carrier frequency are 32 dB and 22 dB over 2 MHz bandwidth, respectively.

This result is much lower than the theoretical prediction, 54 dB of peak SNDR in a 2 MHz bandwidth at 10 GHz. The performance is mainly limited by the nonideal behavior of the used modulator and photodiodes. However, these limitations can be fixed to a large extent by using improved components.

There has been great progress in high-speed optical modulators in recent years.

For example, 40 GHz dual output $LiNbO_3$ modulators with V_π of 5 V are commercially available. Moreover, the use of linearized modulators [120] can greatly improve the nonlinearity limitations imposed in the conventional sinusoid-response modulators. Matched-paired photodiodes with extended linearity over 10 mW are also available. The next version experiment is in progress with improved optical components and signal sources. With state-of-the-art optical components and even lower timing jitter (in 1 fs range) from more carefully engineered mode-locked laser sources, the envisioned performance reaches 60 dB SNDR up to 100 GHz carrier frequency.

More generally, photonic ADC techniques have a promise in achieving high-speed and high-resolution ADC performances in the near future. Not only the narrowband case shown in this Chapter, a more general broadband ADC can be implemented, for example, by a time-stretched pulse demultiplexing approach [121, 122]. The photonic ADCs can be implemented by commercially available discrete optical and electronic components at an instrument level as it is done in this Chapter. A more attractive and interesting future direction is implementing the entire functionalities on electronic-photonic integrated circuits (EPICs) [122]. It will be exciting years to come for the photonic ADC research and development community whether it can demonstrate ground-breaking results that electronic counterparts cannot achieve and finally have a "real" impact on commercial and/or special-purpose ADCs after 30 years of research.

Chapter 6

Conclusion

6.1 Summary of Work

In this thesis work, high-precision synthesis of ultrafast optical pulse signals and phase-stable microwave signals from low-noise mode-locked lasers is studied. The distribution of optical/microwave signals to remote locations as well as the diagnosis of microwave signals with optical pulse trains are also investigated.

Coherent superposition of multiple mode-locked lasers can synthesize shorter, more intense, or even 'arbitrary' optical pulses that a single mode-locked laser cannot generate. For demonstration of the high-precision synchronization between independent lasers, ultrabroadband prism-less Ti:sapphire and Cr:forsterite mode-locked lasers are used. A broadband 50:50 beam splitter with matched group delay dispersion is designed and fabricated for efficient pulse combining and splitting. Subfemtosecond (<0.4 fs) timing synchronization over 12 hours is demonstrated with a balanced optical cross-correlator. In addition to the timing lock, phase synchronization to a 3-MHz local oscillator with subfemtosecond accuracy (<0.5 fs) over 1000 seconds is achieved. To reduce residual timing and phase jitters well below optical cycle, noise eater and orthogonal controller are implemented. Drift-free subfemtosecond timing and phase synchronization enables phase-coherent spectrum over 1.5 octaves that has a potential to generate single-cycle optical pulses at 1 μm.

Mode-locked lasers can also synthesize low-noise microwave signals. Although mode-locked lasers can produce ultralow-noise signals as a form of optical pulse trains, the transfer of stability from optical domain to electronic domain is a highly non-trivial task. The excess noise in the photodetection process hinders long-term stable extraction of microwave signals. To build a drift-free interface between optical and electronic domains with minimal excess noise, an optoelectronic phase-locked loop based on electro-optic sampling with a differentially-biased Sagnac-loop is proposed and demonstrated. Long-term (>1 hour) 3-mrad level phase stability of a 10.225 GHz microwave signal extracted from a mode-locked laser is demonstrated.

The timing information in optical and microwave signals needs to be distributed to remote locations for effective synchronization over long distances. When using an optical fiber for the pulse delivery, acoustic noise and thermal drifts induce large timing fluctuations. It should be cancelled by a length-correction feedback loop. A single type-II phase-matched PPKTP crystal is used to construct a compact and self-aligned balanced optical cross-correlator for precise timing detection that conventional microwave mixers cannot do. A 310 m long fiber link is stabilized with long-term sub-10 fs accuracy. The timing link is also installed in a real accelerator environment and showed less than 25 fs drift over 12 hours in the first test.

The use of optical pulse trains for sampling of high-frequency (>10 GHz) microwave signals can be beneficial because of the ultralow timing jitter of mode-locked lasers. An optical subsampling downconverter for analog-to-digital conversion of narrowband high-frequency microwave signals is demonstrated in a collaboration with the MIT High Speed Circuits and Systems Group. The measured signal to noise-and-distortion ratio (SNDR) of 1-Mbps GMSK signals at 9.5 GHz carrier frequency is 22 dB over 2 MHz bandwidth. It has a potential to increase this SNDR up to 54 dB with better optical modulators.

The devices and techniques presented in this thesis provide a platform for large-scale femtosecond (and potentially *sub*femtosecond)-precision timing distribution and synchronization systems.

6.2 Future Direction

High-precision measurements and controls have enabled to access new regimes that were not accessible before. In this thesis work, I strived for making ultrashort and ultralow-noise optical pulses access such new regimes in precision by developing new optical-electrical hybrid approaches in signal synthesis, distribution and diagnosis.

Because tomorrow's world will need even higher speed, higher accuracy and higher control capabilities, from basic science to consumer electronic products, the use of optical pulse trains will find more applications. One important direction is how we can implement the high-precision optoelectronic functionalities such as phase-locked loops, analog-to-digital converters, and intra- and inter-chip interconnections on a silicon chip with conventional CMOS circuitries. We can generate optical and/or electronic clock signals with higher speed and much lower jitters, implement high-speed, high-resolution analog-to-digital converters for software radios, or make multiple chips working together with higher efficiency by high-density interconnections, just to name a few applications.

The high-precision accuracy does not need to be confined to an IC chip. It can be disseminated over long distances too. In this context, another research direction lies on the improvements of timing distribution systems. By optimizing cw and ultrashort pulse delivery schemes, precise clock signals can be delivered anywhere it is necessary. In this way, for example, remonte clock distribution and synchronization exclusively done by the global positioning system (GPS) can be replaced for certain applications. In the near future, we might be able to create large-scale networks with femtosecond precision.

Appendix A

Control of Femtosecond Laser Frequency Combs

The frequency comb dynamics can be analyzed in an analytic way using soliton perturbation theory [66, 125]. In this Appendix Chapter, the major steps and results are reviewed.

The pulse dynamics in a mode-locked laser can be described by the "master" equation [123, 124] in the time domain in a form of nonlinear Schrödinger equation,

$$\begin{aligned} T_R \frac{\partial A(T,t)}{\partial T} &= \left[(g-l) + D_f \frac{\partial^2}{\partial t^2} + \gamma |A|^2 + jD_2 \frac{\partial^2}{\partial t^2} - j\delta |A|^2 \right] A(T,t) + L_{\text{pert}} \\ &= D_{\text{irrev}} A(T,t) + jD_2 \frac{\partial^2 A(T,t)}{\partial t^2} - j\delta |A|^2 A(T,t) + L_{\text{pert}} \end{aligned} \tag{A.1}$$

where $A(T,t)$ is the pulse amplitude, T_R is the round-trip time, T is the long-term time variable of round-trip time scale, t is the short-term time variable, l is the amplitude loss for round-trip, g is the amplitude gain, D_f is the gain filtering coefficient, γ is the saturable absorber modulation coefficient, D_2 is the second order dispersion coefficient, δ is the self-phase modulation (SPM) coefficient, L_{pert} is the perturbations (in amplitude, phase, frequency and timing), and D_{irrev} is an operator describing the irreversible dynamics in a mode-locked laser, i.e., $D_{\text{irrev}} = g - l + D_f \frac{\partial^2}{\partial t^2} + \gamma |A|^2$.

Let's first consider the case without perturbation. The pulse train amplitude can

be written as

$$A(T,t) = \sum_{m=-\infty}^{+\infty} a(T = mT_R, t) e^{j[2\pi f_c\{t - mT_R + \left(\frac{1}{v_g} - \frac{1}{v_p}\right)2mL\}]}, \tag{A.2}$$

where $a(T,t)$ is the pulse envelope, f_c is the optical carrier frequency, v_g and v_p are the group and phase velocity in the laser cavity, and L is the laser cavity length.

The steady-state solution $a(T,t)$ has a form of a soliton:

$$a(T,t) = A_0 \text{sech}\left(\frac{t}{\tau}\right) e^{-j\phi_0 \frac{T}{T_R}} \tag{A.3}$$

with the soliton phase shift

$$\phi_0 = \frac{1}{2}\delta A_0^2 = \frac{|D_2|}{\tau^2}, \tag{A.4}$$

where A_0 is the amplitude and τ is the pulse width.

From Eqs. (A.2) and (A.3), the pulse-to-pulse carrier-envelope phase shift $\Delta\phi_{CE}$ is given by

$$\begin{aligned} \Delta\phi_{CE} &= \arg(A((m+1)T_R, t) - \arg(A(mT_R, t)) \\ &= 2\pi f_c \left(\frac{1}{v_g} - \frac{1}{v_p}\right) 2L - \phi_0 \\ &= 2\pi f_c T_R \left(1 - \frac{v_g}{v_p}\right) - \phi_0. \end{aligned} \tag{A.5}$$

Then the carrier-envelope offset frequency f_{ceo} is expressed as

$$\begin{aligned} f_{ceo} &= \frac{\Delta\phi_{CE}}{2\pi T_R} \\ &= f_c \left(1 - \frac{v_g}{v_p}\right) - \frac{\delta A_0^2}{4\pi} f_{rep}, \end{aligned} \tag{A.6}$$

where $f_{rep} = 1/T_R$ is the pulse repetition rate.

Now, let's consider the case when perturbations exist. The solution of the master equation is then a soliton-like pulse with perturbations in amplitude, phase, frequency

and timing, plus continuum.

$$a(T,t) = \left[(A_0 + \Delta A_0)\mathrm{sech}\left(\frac{t-\Delta t}{\tau}\right) + a_c(T,t)\right] e^{-j\phi_0 T/T_R} e^{j\Delta p t} e^{-j\Delta\theta} \tag{A.7}$$

with pulse energy $w_0 = 2A_0^2\tau$.

If the dominating perturbation is the self-steepening of the few-cycle pulse [66], i.e., the variation of the index during an optical cycle, it can be included by adding the following term to the master equation

$$L_{\mathrm{pert}} = -\frac{\delta}{2\pi f_c}\frac{\partial}{\partial t}(|A|^2 A). \tag{A.8}$$

The timing shift by self-steepening is

$$T_R \frac{\partial \Delta t(T)}{\partial T}\bigg|_{\mathrm{self-steep}} = \Delta\left(\frac{1}{v_g}\right) = \frac{\delta A_0^2}{2\pi f_c} \tag{A.9}$$

Then f_{ceo} result in Eq. (A.6) should be changed by this effect,

$$\begin{aligned} f_{ceo} &= f_c\left(1 - \frac{v_g}{v_p}\right) - \frac{\delta A_0^2}{4\pi} f_{rep} + f_c \frac{\partial \Delta t(T)}{\partial T}\bigg|_{\mathrm{self-steep}} \\ &= f_c\left(1 - \frac{v_g}{v_p}\right) + \frac{\delta A_0^2}{4\pi} f_{rep}. \end{aligned} \tag{A.10}$$

Note that the sign of $(\delta A_0^2 f_{rep}/4\pi)$ term is changed by including the self-steepening. This effect is also confirmed experimentally with a Ti:sapphire Kerr-lens mode-locked laser in Ref. [66].

A change in group delay due to the Kerr nonlinearity also changes the optical cavity length and the repetition rate as

$$\Delta f_{rep}\Big|_{\mathrm{self-steep}} = -f_{rep}^2 \Delta t(T)\Big|_{\mathrm{self-steep}} = -\frac{\delta A_0^2}{2\pi f_c} f_{rep}^2 = -\frac{2}{m_0}\frac{\delta A_0^2}{4\pi} f_{rep}, \tag{A.11}$$

where $m_0 = f_c/f_{rep}$ is the mode number of the carrier frequency.

For control of femtosecond laser frequency comb, an intra-cavity energy change Δw with an AOM in the pump beam and a cavity length change ΔL with PZTs in

the laser cavity are used. Now the dependence of f_{ceo} and f_{rep} on Δw and ΔL will be derived.

From Eq. (A.10), the f_{ceo} depends on the intra-cavity energy change Δw and the cavity length change ΔL according to

$$\left.\frac{\Delta f_{ceo}}{f_{rep}}\right|_{\Delta L=0} = \frac{\delta A_0^2}{4\pi}\frac{\Delta w}{w_0} \tag{A.12}$$

and

$$\left.\frac{\Delta f_{ceo}}{f_{rep}}\right|_{\Delta w=0} = m_0\left(1-\frac{v_g}{v_p}\right)\frac{\Delta L}{L_0}. \tag{A.13}$$

From Eq. (A.11), the f_{rep} depends on the intra-cavity energy Δw as

$$\left.\frac{\Delta f_{rep}}{f_{rep}}\right|_{\Delta L=0} = -\frac{2}{m_0}\frac{\delta A_0^2}{4\pi}\frac{\Delta w}{w_0}. \tag{A.14}$$

The cavity length dependence of f_{rep} is naturally given by

$$\left.\frac{\Delta f_{rep}}{f_{rep}}\right|_{\Delta w=0} = -\frac{\Delta L}{L_0}. \tag{A.15}$$

From Eqs. (A.12) to (A.15), the f_{ceo} and f_{rep} dynamics are summarized as

$$\frac{\Delta f_{ceo}}{f_{rep}} = \frac{\delta A_0^2}{4\pi}\frac{\Delta w}{w_0} + m_0\left(1-\frac{v_g}{v_p}\right)\frac{\Delta L}{L_0} \tag{A.16}$$

and

$$\frac{\Delta f_{rep}}{f_{rep}} = -\frac{2}{m_0}\frac{\delta A_0^2}{4\pi}\frac{\Delta w}{w_0} - \frac{\Delta L}{L_0}. \tag{A.17}$$

Finally, the change of each comb line position (Δf_m) is expressed as

$$\begin{aligned}\Delta f_m &= m\Delta f_{rep} + \Delta f_{ceo} \\ &= \left[\left(1-\frac{2m}{m_0}\right)\frac{\delta A_0^2}{4\pi}\frac{\Delta w}{w_0} + \left\{m_0\left(1-\frac{v_g}{v_p}\right) - m\right\}\frac{\Delta L}{L_0}\right] f_{rep}.\end{aligned} \tag{A.18}$$

Bibliography

[1] R. Ell, U. Morgner, F. X. Kaertner, J. G. Fujimoto, E. P. Ippen, V. Scheuer, G. Angelow, T. Tschudi, M. J. Lederer, A. Boiko, and B. Luther-Davies, "Generation of 5-fs pulses and octave-spanning spectra directly from a Ti:sapphire laser," Opt. Lett. **26**, 373–375 (2001).

[2] M. Dantus, R. M. Bowman, and A. H. Zewail, "Femtosecond laser observations of molecular vibration and rotation," Nature **343**, 737 – 739 (1990).

[3] R. Holzwarth, Th. Udem, T. W. Haensch, J. C. Knight, W. J. Wadsworth, and P. St. J. Russell, "Optical Frequency Synthesizer for Precision Spectroscopy," Phys. Rev. Lett. **85**, 2264-2267 (2000).

[4] Th. Udem, R. Holzwarth, and T. W. Hänsch, "Optical frequency metrology," Nature **416**, 233 – 237 (2002).

[5] S. A. Diddams, Th. Udem, J. C. Bergquist, E. A. Curtis, R. E. Drullinger, L. Hollberg, W. M. Itano, W. D. Lee, C. W. Oates, K. R. Vogel, and D. J. Wineland, "An Optical Clock Based on a Single Trapped $^{199}Hg^{+}$ Ion," Science **293**, 825 (2001).

[6] Royal Swedish Academy of Sciences, "The Nobel Prize in Physics 2005 - Advanced Information" (2005), http://nobelprize.org/physics/laureates/2005/phyadv05.pdf.

[7] S. T. Cundiff, "Phase stabilization of ultrashort optical pulses," J. Phys. D. **35**, R43 – R59 (2002).

[8] M. Hentschel, R. Kienberger, Ch. Spielmann, G. A. Reider, N. Milosevic, T. Brabec, P. Corkum, U. Heinzmann, M. Drescher, and F. Krausz, "Attosecond metrology," Nature **414**, 509 – 513 (2001).

[9] A. Baltuska, T. Udem, M. Uiberacker, M. Hentschel, E. Goulielmakis, C. Gohle, R. Holzwarth, V. S. Yakovlev, A. Scrinzi, T. W. Haensch, and F. Krausz, "Attosecond control of electronic processes by intense light fields," Nature **421**, 611– 615 (2003).

[10] S. Namiki and H. A. Haus, "Noise of the stretched pulse fiber ring laser: Part I-Theory," IEEE J. Quantum Electron. **33**, 649 (1997).

[11] A. Bartels and H. Kurz, "Generation of a broadband continuum by a Ti:sapphire femtosecond oscillator with a 1-GHz repetition rate," Opt. Lett. **27**, 1839-1841 (2002).

[12] L. Matos, O. Kuzucu, T. R. Schibli, J. Kim, E. P. Ippen, D. Kleppner, and F. X. Kaertner, "Direct frequency comb generation from an octave spanning, prismless Ti:sapphire laser," Opt. Lett. **29**, 1683–1685 (2004).

[13] S. C. Zeller, T. Südmeyer, K. J. Weingarten, and U. Keller, "Passively mode-locked 77-GHz Er:Yb:glass laser," Electron. Lett. **43**, 32-33 (2007).

[14] J. Chen, J. W. Sickler, E. P. Ippen and F. X. Kärtner, "High repetition rate, low jitter, low intensity noise, fundamentally mode-locked 167 fs soliton Er-fiber laser," Opt. Lett. **32**, 1566-1568 (2007).

[15] O. D. Mücke, R. Ell, A. Winter, J. Kim, J. R. Birge, L. Matos, and F. X. Kärtner, "Self-Referenced 200 MHz Octave-Spanning Ti:Sapphire Laser with 50 Attosecond Carrier-Envelope Phase Jitter," Opt. Express **13**, 5163 (2005).

[16] A. Baltuska, M. Uiberacker, E. Goulielmakis, R. Kienberger, V. S. Yakovlev, T. Udem, T. W. Hänsch, and F. Krausz, "Phase-controlled amplification of few-cycle laser pulses," IEEE J. Sel. Top. Quantum Electron. **9**, 972-989 (2003).

[17] F. X. Kaertner, U. Morgner, R. Ell, T. Schibli, J. G. Fujimoto, E. P. Ippen, V. Scheuer, G. Angelow, and T. Tschudi, "Ultrabroadband double-chirped mirror pairs for generation of octave spectra," J. Opt. Soc. Am. B **18**, 882 – 885 (2001).

[18] G. Sansone, E. Benedetti, F. Calegari, C. Vozzi, L. Avaldi, R. Flammini, L. Poletto, P. Villoresi, C. Altucci, R. Velotta, S. Stagira, S. De Silvestri and M. Nisoli, "Isolated single-cycle attosecond pulses," Science **314**, 443-446 (2006).

[19] J. B. Schlager, B. E. Callicoatt, R. P. Mirin, N. A. Sanford, D. J. Jones and J. Ye, "Passively mode-locked glass waveguide laser with 14-fs timing jitter," Opt. Lett. **28**, 2411 (2003).

[20] J. Kim, F. Ö. Ilday, F. X. Kärtner, O. D. Mücke, M. H. Perrott, W. S. Graves, D. E. Moncton, T. Zwart, "Large-Scale Timing Distribution and RF-Synchronization for FEL Facilities," Proceedings of Free Electron Laser Conference 2004, p. 329, August 2004.

[21] C. X. Yu, S. Namiki and H. A. Haus, "Noise of the stretched pulse fiber ring laser: Part II-Experiments," IEEE J. Quantum Eletron. **33**, 660 (1997).

[22] R. Paschotta, "Noise of mode-locked lasers (Part II): timing jitter and other fluctuations," Appl. Phys. B **79** 163 – 173 (2004).

[23] T. W. Hänsch, "A proposed sub-femtosecond pulse synthesizer using separate phase-locked laser oscillators," Opt. Commun. **80**, 71 (1990).

[24] E. N. Ivanov, S. A. Diddams and L. Hollberg, "Analysis of Noise Mechanisms Limiting the Frequency Stability of Microwave Signals Generated With a Femtosecond Laser," IEEE J. Sel. Top. Quantum Electron. **9**, 1059 (2003).

[25] B. Lorbeer, F. Ludwig, H. Schlarb, A. Winter, "Noise and Drift Characterization of Direct Laser to RF Conversion Scheme for the Laser Based Synchronization System for FLASH at DESY," Proceedings of Particle Accelerator Conference 2007, p. 182, June 2007.

[26] A. Winter, P. Schmüsser, H. Schlarb, F. Ö. Ilday, J. Kim, J. Chen, F. X. Kärtner, D. Cheever, T. Zwart, D. Wang, "High-Precision Optical Synchronization Systems for X-Ray Free Electron Lasers," Proceedings of Free Electron Laser 2005, p. 676, August 2005.

[27] D. D. Hudson, S. M. Foreman, S. T. Cundiff and J. Ye, "Synchronization of mode-locked femtosecond lasers through a fiber link," Opt. Lett. **31**, 1951 (2006).

[28] T. Brabec and F. Krausz, "Intense few-cycle laser fields: Frontiers of nonlinear optics," Rev. Mod. Phys. **72**, 545 – 591 (2000).

[29] U. Morgner, R. Ell, G. Metzler, T. R. Schibli, J. G. Fujimoto, E. P. Ippen, and F. X. Kaertner, "Nonlinear optics with phase-controlled pulses in the sub-two-cycle regime," Phys. Rev. Lett. **86**, 5462 – 5465 (2001).

[30] G. G. Paulus, F. Grasbon, H. Walther, P. Villoresi, M. Nisoli, S. Stagira, E. Priori, and S. DeSilvestri, "Absolute-phase phenomena in photoionization with few-cycle laser pulses," Nature **414**, 182– 184 (2001).

[31] O. D. Mücke, T. Tritschler, M. Wegener, U. Morgner, and F. X. Kaertner, "Signatures of Carrier-Wave Rabi-Flopping in GaAs," Phys. Rev. Lett. **87**, 057401 (2001).

[32] O. D. Mücke, T. Tritschler, and M. Wegener, "Role of the Carrier-Envelope Offset Phase of Few-Cycle Pulses in Nonperturbative Resonant Nonlinear Optics," Phys. Rev. Lett. **89**, 127401 (2002).

[33] D. B. Milosevic, G. G. Paulus, and W. Becker, "Phase-dependent effects of a few-cycle laser pulse," Phys. Rev. Lett. **89**, 153001 (2002).

[34] T. Tritschler, O. D. Mücke, M. Wegener, U. Morgner, and F. X. Kaertner, "Evidence of Third-Harmonic Generation in DIsguise of Second-Harmonic Generation in Extreme Nonlinear Optics," Phys. Rev. Lett. **90**, 217404 (2003).

[35] T. M. Fortier, P. A. Roos, D. J. Jones, S. T. Cundiff, R. D. R. Bhat and J. E. Sipe, "Carrier-envelope phase-controlled quantum interference of injected photocurrents in semiconductors," Phys. Rev. Lett, **92**, 147403 (2004).

[36] P. Hommelhoff, C. Kealhofer and M. A. Kasevich, "Ultrafast electron pulses from a tungsten tip triggered by low-power femtosecond laser pulses," Phys. Rev. Lett. **97**, 247402 (2006).

[37] C. Van Vlack and S. Hughes, "Carrier-envelope offset phase control of ultrafast optical rectification in resonantly excited semiconductors," Phys. Rev. Lett. **98**, 167404 (2007).

[38] M. Y. Shverdin, D. R. Walker, D. D. Yavuz, G. Y. Yin, and S. E. Harris, "Generation of a single-cycle optical pulse," Phys. Rev. Lett. **94**, 033904 (2005).

[39] S. Adachi, P. Kumbhakar, T. Kobayashi, "Quasi-monocyclic near-infrared pulses with a stabilized carrier-envelope phase characterized by noncollinear cross-correlation frequency-resolved optical gating," Opt. Lett. **29**, 1150 (2004).

[40] A. Baltuska, T. Fuji, and T. Kobayashi, "Visible pulse compression to 4 fs by optical parametric amplification and programmable dispersion control," Opt. Lett. **27**, 306 – 308 (2002).

[41] B. Schenkel, J. Biegert, U. Keller, C. Vozzi, M. Nisoli, G. Sansone, S. Stagira, S. De Silvestri, and O. Svelto, "Generation of 3.8-fs pulses from adaptive compression of a cascaded hollow fiber supercontinuum," Opt. Lett. **28**, 1987 – 1989 (2003).

[42] K. Yamane, Z. Zhang, K. Oka, R. Morita, M. Yamashita, A. Suguro, "Optical pulse compression to 3.4 fs in the monocycle region by feedback phase compensation," Opt. Lett. **28**, 2258 – 2260 (2003).

[43] Z. Wei, Y. Kobayashi, Z. Zhang, and K. Torizuka, "Generation of two-color femtosecond pulses by self-synchronizing Ti:sapphire and Cr:forsterite lasers," Opt. Lett. **26**, 1806–1808 (2001).

[44] T. R. Schibli, J. Kim, O. Kuzucu, J. Gopinath, S. N. Tandon, G. S. Petrich, L. A. Kolodziejski, J. G. Fujimoto, E. P. Ippen, and F. X. Kaertner, "Attosecond active synchronization of passively mode-locked lasers using balanced cross-correlation," Opt. Lett. **28**, 947 – 949 (2003).

[45] A. Bartels, N. R. Newbury, I. Thomann, L. Hollberg, and S. A. Diddams, "Broadband phase-coherent optical frequency synthesis with actively linked Ti:sapphire and Cr:forsterite femtosecond lasers," Opt. Lett. **29**, 403 (2004).

[46] D. Yoshitomi, Y. Kobayashi, H. Takada, M. Kakehata and K. Torizuka, "100-attosecond timing jitter between two-color mode-locked lasers by active-passive hybrid synchronization," Opt. Lett. **30**, 1408 (2005).

[47] Y. Kobayashi, D. Yoshitomi, M. Kakehata, H. Takada, and K. Torizuka, "Long-term optical phase locking between femtosecond Ti:sapphire and Cr:forsterite lasers," Opt. Lett. **30**, 2496 (2005).

[48] R. K. Shelton, L. Ma, H. C. Kapteyn, M. M. Murnane, J. L. Hall, J. Ye, "Phase-Coherent Optical Pulse Synthesis from Separate Femtosecond Lasers," Science **293**, 1286 – 1289 (2001).

[49] F. X. Kaertner, N. Matuschek, T. Schibli, U. Keller, H. A. Haus, C. Heine, R. Morf, V. Scheuer, M. Tilsch, and T. Tschudi, "Design and fabrication of double-chirped mirrors," Opt. Lett. **22**, 831 – 833 (1997).

[50] D. E. Spence, P. N. Kean, and W. Sibbett, "60-fsec pulse generation from a self-mode-locked Ti:sapphire laser," Opt. Lett. **16**, 42 – 44 (1991).

[51] T. R. Schibli, O. Kuzucu, J. Kim, E. P. Ippen, J. G. Fujimoto, F. X. Kaertner, "Toward Single-Cycle Laser Systems," IEEE J. Sel. Top. Quant. Elec. **9**, 990–1001 (2003).

[52] Y. Chen, F. X. Kaertner, U. Morgner, S. H. Cho, H. A. Haus, E. P. Ippen, and J. G. Fujimoto, "Dispersion-managed mode locking," J. Opt. Soc. Am. B **16**, 1999 – 2004 (1999).

[53] J. W. Nicholson and W. Rudolph, "Noise sensitivity and accuracy of femtosecond pulse retrieval by phase and intensity from correlation and spectrum only (PICASO)," J. Opt. Soc. Am. B **19**, 330 (2002).

[54] V. Petricevic, S. K. Gayen, R. R. Alfano, K. Yamagashi, H. Anzai, and Y. Yamagashi, "Laser action in chromium-doped forsterite," Appl. Phys. Lett. **52**, 1040–1042 (1988).

[55] C. Chudoba, J. G. Fujimoto, E. P. Ippen, H. A. Haus, U. Morgner, F. X. Kaertner, V. Scheuer, G. Angelow, and T. Tschudi, "All-solid-state Cr:forsterite laser generating 14-fs pulses at 1.3 μm," Opt. Lett. **26**, 292–294 (2001).

[56] B. E. Bouma, G. J. Tearney, I. P. Bilinsky, B. Golubovic, and J. G. Fujimoto, "Self-phase-modulated Kerr-lens mode-locked Cr:forsterite laser source for optical coherence tomography," Opt. Lett. **21**, 1839–1841 (1996).

[57] A. A. Ivanov, B. I. Minkov, G. Jonusauskas, J. Oberle, and C. Rullière, "Influence of Cr^{4+} in concentration on cw operation of forsterite laser and its relation to thermal problems," Opt. Commun. **116**, 131–135 (1995).

[58] Z. Zhang, K. Torizuka, T. Itatani, K. Kobayashi, T. Sugaya, and T. Nakagawa, "Femtosecond Cr:Forsterite Laser with Mode Locking Initiated by a Quantum-Well Saturable Absorber," IEEE J. Quant. Elec. **33**, 1975–1980 (1997).

[59] A. Agnesi, E. Piccinini, G. C. Reali, "Influence of thermal effects in Kerr-lens mode-locked femtosecond Cr^{4+}:forsterite lasers," Opt. Comm. **135**, 77 – 82 (1997).

[60] A. Sennaroglu, "Analysis and optimization of lifetime thermal loading in continuous-wave Cr-doped solid-state lasers," J. Opt. Soc. Am. B **18**, 1578–1586 (2001).

[61] S. N. Tandon, J. T. Gopinath, H. M. Shen, G. S. Petrich, L. A. Kolodziejski, F. X. Kärtner, E. P. Ippen, "Large-area broadband saturable Bragg reflectors by use of oxidized AlAs," Opt. Lett. **29**, 2551 (2004).

[62] J. Kim, "Toward Single-Cycle Optical Pulses," S. M. Thesis, Department of Electrical Engineering and Computer Science, Massachusetts Institute of Technology, Cambridge, MA, Feb 2004.

[63] Z. Zhang, K. Torizuka, T. Itatani, K. Kobayashi, T. Sugaya, T. Nakagawa, H. Takahashi, "Broadband semiconductor saturable-absorber mirror for a self-starting mode-locked Cr:forsterite laser," Opt. Lett. **23**, 1465 – 1467 (1998).

[64] J. Son, J. V. Rudd, and J. F. Whitaker, "Noise characterization of a self-mode-locked Ti:sapphire laser," Opt. Lett. **17**, 733 – 735 (1992).

[65] C. H. Cox, III, "Analog optical links: theory and practice" (Cambridge University Press, 2004).

[66] L. Matos, O. D. Mücke, J. Chen and F. X. Kärtner, "Carrier-envelope phase dynamics and noise analysis in octave-spanning Ti:sapphire lasers," Opt. Express **14**, 2497–2511 (2006).

[67] T. M. Fortier, D. J. Jones, S. T. Cundiff, "Phase stabilization of an octave-spanning Ti:sapphire laser," Opt. Lett. **28**, 2198-2200 (2003).

[68] C. Iaconis and I. A. Walmsley, "Self-Referencing Spectral Interferometry for Measuring Ultrashort Optical Pulses," IEEE J. Quant. Elec. **35**, 501 – 509 (1999).

[69] G. Lenz, B. J. Eggleton, C. K. Madsen, C. R. Giles, and G. Nykolak, "Optimal Dispersion of Optical Filters for WDM Systems," IEEE Photon. Tech. Lett. **10**, 567-569 (1998).

[70] A. V. Tikhonravov and M. K. Trubetskov, "OptiLayer thin film software" (Optilayer Ltd., Moscow, Russia, 2003), http://www.optilayer.com/general.htm.

[71] V. Scheuer, M. Tilsch, and T. Tschudi, "Reduction of absorption losses in ion beam sputter deposition of optical coatings for the visible and near infrared," in Optical Interference Coating, F. Abeles ed., Proc. SPIE **2253**, 445-454 (1994).

[72] M. Tilsch, V. Scheuer, and T. Tschudi, "Direct optical monitoring instrument with a double detection system for the control of multilayer systems from the visible to the near infrared," in Optical Interference Coating, F. Abeles ed., Proc. SPIE **2253**, 414-422 (1994).

[73] J. Kim, J. R. Birge, V. Sharma, J. G. Fujimoto, F. X. Kärtner, V. Scheuer, G. Angelow, "Ultrabroadband beam splitter with matched group-delay dispersion," Opt. Lett. **30**, 1569 (2005).

[74] K. Naganuma, K. Mogi, and H. Yamada, "Group-delay measurement using the Fourier transform of an interferometric cross correlation generated by white light," Opt. Lett. **15**, 393-395 (1990).

[75] R. K. Shelton, S. M. Foreman, L. Ma, J. L. Hall, H. C. Kapteyn, M. M. Murnane, M. Notcutt, and J. Ye, "Subfemtosecond timing jitter between two independent, actively synchronized, mode-locked lasers," Opt. Lett. **27**, 312–314 (2002).

[76] L. Ma, R. K. Shelton, H. C. Kapteyn, M. M. Murnane, and J. Ye, "Sub-10-femtosecond active synchronization of two passively mode-locked Ti:sapphire oscillators," Phys. Rev. A **64**, 021802(R) (2001).

[77] Frank Ludwig, Deutsches Elektronen-Synchrotron, Hamburg, Germany (personal communication, 2006).

[78] G. F. Franklin, J. D. Powell and A. Emami-Naeini, "Feedback Control of Dynamic Systems" (Addison Wesley, 1994).

[79] J. Kim, J. Burnham, J. Chen, F. X. Kärtner, F. Ö. Ilday, F. Ludwig, H. Schlarb, A. Winter, M. Ferianis and D. Cheever, "An Integrated Femtosecond Timing Distribution Systems for XFELs," in Proceedings of European Particle Accelerator Conference 2006, p. 2744, June 2006.

[80] H. A. Haus, "Waves and Fields in Optoelectronics," (Prentice-Hall, Englewood Cliffs, NJ, 1984).

[81] K. W. Holman, D. J. Jones, J. Ye and E. P. Ippen, "Orthogonal control of the frequency comb dynamics of a mode-locked laser diode," Opt. Lett. **28**, 2405-2407 (2003).

[82] J. R. Birge, R. Ell, and F. X. Kärtner, "Two-dimensional spectral shearing interferometry for few-cycle pulse characterization," Opt. Lett. **31**, 2063-2065 (2006).

[83] T. M. Fortier, D. J. Jones, J. Ye and S. T. Cundiff, "Highly Phase Stable Mode-Locked Lasers," IEEE J. Sel. Top. Quantum Electron. **9**, 1002-1010 (2003).

[84] H. A. Haus and A. Mecozzi, "Noise of Mode-Locked Lasers," IEEE J. Quant. Elec. **29**, 983 – 996 (1993).

[85] X. S. Yao and L. Maleki, "Optoelectronic Microwave Oscillator", J. Opt. Soc. Am. B **13**, 1725 (1996).

[86] J.-F. Cliche and B. Shillue, "Precision Timing Control for Radioastronomy," IEEE Control Sys. Mag. **26**, 19-26 (2006).

[87] S. M. Foreman, K. W. Holman, D. D. Hudson, D. J. Jones and J. Ye, "Remote transfer of ultrastable frequency references via fiber networks," Rev. Sci. Instrum. **78**, 021101 (2007).

[88] A. Bartels, S. A. Diddams, C. W. Oates, G. Wilpers, J. C. Bergquist, W. H. Oskay and L. Hollberg, "Femtosecond-laser-based synthesis of ultra-stable microwave signals from optical frequency references," Opt. Lett. **30**, 667 (2005).

[89] J. J. McFerran, E. N. Ivanov, A. Bartels, G. Wilpers, C. W. Oates, S. A. Diddams, and L. Hollberg, "Low-noise synthesis of microwave signals from an optical source," Electron. Lett. **41**, 650 (2005).

[90] E. N. Ivanov, S. A. Diddams and L. Hollberg, "Noise Properties of Microwave Signals Synthesized with Femtosecond Lasers," IEEE Trans. Ultrason. Ferroelectr. Freq. Control **54**, 736-745 (2007).

[91] L.-S. Ma, Z. Bi, A. Bartels, K. Kim, L. Robertsson, M. Zucco, R. S. Windeler, G. Wilpers, C. Oates, L. Hollberg, and S. A. Diddams, "Frequency Uncertainty for Optically Referenced Femtosecond Laser Frequency Combs," IEEE J. Quantum Electron. **43**, 139-146 (2007).

[92] E. N. Ivanov, S. A. Diddams and L. Hollberg, "Study of the Excess Noise Associated with Demodulation of Ultra-Short Infrared Pulses," IEEE Trans. Ultrason. Ferroelectr. Freq. Control **52**, 1068 (2005).

[93] M. H. Perrott, "PLL Design Using the PLL Design Assistant Program," http://www-mtl.mit.edu/research/perrottgroup/tools.html (2002).

[94] J. Kim, F. X. Kärtner, and M. H. Perrott, "Femtosecond synchronization of radio frequency signals with optical pulse trains," Opt. Lett. **29**, 2076 (2004).

[95] K. Böhm, P. Russer, E. Weidel, and R. Urlich, "Low-noise fiber-optic rotation sensing," Opt. Lett. **6**, 64-66 (1981).

[96] L.K. Oxenlowe, C. Schubert, C. Schmidt, E. Hilliger, J. Berger, U. Feiste, R. Ludwig, H.G. Weber, "Optical clock recovery employing an optical PLL using cross-phase modulation in a Sagnac-interferometer," CLEO 2001, (Optical Society of America, Washington DC, 2001), pp. 525-526.

[97] A. E. Siegman, *Lasers* (University Science Books, 1986).

[98] J. Kim, F. X. Kärtner, and F. Ludwig, "Balanced optical-microwave phase detectors for optoelectronic phase-locked loops," Opt. Lett. **31**, 3659-3661 (2006).

[99] G. Lenz, K. Tamura, H. A. Haus and E. P. Ippen, "All-solid-state femtosecond source at 1.5 um," Opt. Lett. **20**, 1289-1291 (1995).

[100] J. Kim, F. Ludwig, M. Felber and F. X. Kärtner, "Long-term stable microwave signal extraction from mode-locked lasers," Opt. Express **15**, 8951-8959 (2007).

[101] J. Ye, J. Peng, R. J. Jones, K. W. Holman, J. L. Hall, D. J. Jones, S. A. Diddams, J. Kitching, S. Bize, J. C. Bergquist, L. W. Hollberg, L. Robertsson, and

L. Ma, "Delivery of high-stability optical and microwave frequency standards over an optical fiber network," J. Opt. Soc. Am. B **20**, 1459 – 1467 (2003).

[102] K. W. Holman, D. J. Jones, D. D. Hudson, J. Ye, "Precise frequency transfer through a fiber network by use of 1.5-um mode-locked sources," Opt. Lett. **29**, 1554 (2004).

[103] K. W. Holman, D. D. Hudson, J. Ye and D. J. Jones, "Remote transfer of a high-stability and ultralow-jitter timing signal," Opt. Lett. **30**, 1225 (2005).

[104] G. Grosche, B. Lipphardt, H. Schnatz, G. Santarelli, P. Lemonde, S. Bize, M. Lours, F. Narbonneau, A. Clairon, O. Lopez, A. Amy-Klein, and Ch. Chardonnet, "Transmission of an Optical Carrier Frequency over Telecommunication Fiber Link," Paper CMKK2, presented at the Conference on Lasers and Electro-Optics 2007.

[105] F. X. Kärtner, F. Ö. Ilday, J. Kim, A. Winter, F. Grawert, H. Byun, J. Chen, "Progress in Large-Scale Femtosecond Timing Distribution and RF-Synchronizatoin," Proceedings of 2005 Particle Accelerator Conference, p. 284, May 2005.

[106] R. Wilcox and J. Russel, "Synchronizing Lasers over Fiber by Transmitting Continuous Waves," Paper CThHH4, presented at the Conference on Lasers and Electro-Optics 2007.

[107] G. P. Agrawal, "Nonlinear Fiber Optics," 3rd Ed., Academic Press, 2001.

[108] F. König and F. N. C. Wong, "Extended phase matching of second-harmonic generation in periodically poled KTiOPO4 with zero group-velocity mismatch," Appl. Phys. Lett. **84**, 1644 (2004).

[109] J. Kim, J. Chen, Z. Zhang, F. N. C. Wong, F. X. Kärtner, F. Loehl, and H. Schlarb, "Long-term femtosecond timing link stabilization using a single-crystal balanced cross-correlator," Opt. Lett. **32**, 1044-1046 (2007).

[110] F. Loehl, H. Schlarb, J. Chen, F. X. Kärtner and J. Kim, "First Prototype of a Fiber Link Stabilization for the FLASH Synchronization System Based on Optical Cross-Correlation," Paper WEPB16, Workshop on Beam Diagnostics and Instrumentation for Particle Accelerators (DIPAC) 2007, Venice, Italy, May 2007.

[111] L. A. Jiang, S. T. Wong, M. E. Grein, E. P. Ippen and H. A. Haus, "Measuring Timing Jitter With Optical Cross Correlations," IEEE J. Quantum Electron. **38**, 1047 (2002).

[112] A. E. Siegman and D. J. Kuizenga, "Proposed method for measuring picosecond pulsewidths and pulse shapes in cw mode-locked lasers," IEEE J. Quantum Electron. **6**, 212 (1970).

[113] S. Wright, I. M. Mason, M. G. F. Wilson, "High-speed electro-optic analogue-digital conversion," Electron. Lett. **10**, 508 (1974).

[114] H. F. Taylor, "An electro-optic analog-to-digital converter," Proc. IEEE **63**, 1524 (1975).

[115] G. C. Valley, "Photonic analog-to-digital converters," Opt. Express **15**, 1955 (2007).

[116] L. Y. Nathawad, R. Urata, B. Wooley and D. A. B. Miller, "A 40-GHz-bnadwidth, 4-bit, time-interleaved A/D converter using photoconductive sampling," IEEE J. Solid-State Circuits **38**, 2021-2030 (2003).

[117] M. Park, J. Kim, F. X. Kärtner, and M. H. Perrott, "An Optical-Electrical Sub-Sampling Receiver Employing Continuous-Time Delta-Sigma Modulation," Paper A6L-E4, European Solid-State Circuits Conference (ESSCIRC) 2006, Montreux, Switzerland, Sep 2006.

[118] Analog Devices, "Sigma-Delta ADCs and DACs," Application Note AN-283.

[119] M. Park, J. Kim, F. X. Kärtner, and M. H. Perrott, "An Optical-Electrical Sub-Sampling Down-Conversion Receiver Employing CT Δ-Σ Modulation," unpublished manuscript.

[120] G. E. Betts, "Linearized modulator for suboctave-bandpass optical analog links," IEEE Trans. Microwave Theory and Tech. **42**, 2642 (1994).

[121] Y. Han and B. Jalali, "Continuout-time time-stretched analog-to-digital converter array implemented using virtual time gating," IEEE Trans. Circuits and Syst.-I **52**, 1502-1507 (2005).

[122] F. X. Kärtner et al., "Silicon electronic-photonic integrated circuits for high speed analog-to-digital conversion," International Conference on Group IV Photonics, 203-205 (2006).

[123] H. A. Haus, "Theory of mode locking with a fast saturable absorber," J. Appl. Phys. **46**, 3049 – 3058 (1975).

[124] H. A. Haus, "Theory of Mode Locking with a Slow Saturable Absorber," IEEE J. Quant. Elec. **11**, 736 – 746 (1975).

[125] F. X. Kärtner, "6.977 Ultrafast Optics" (MIT, Class note for Spring Term 2005).